Single Cell Imaging of Metabolism with Fluorescent Biosensors

Dissertation Advisor: Dr. Gary Yellen Yin Pun Hung

Single Cell Imaging of Metabolism with Fluorescent Biosensors

Abstract

Cells utilize various signal transduction networks to regulate metabolism. Nevertheless, a quantitative understanding of the relationship between growth factor signaling and metabolic state at the single cell level has been lacking. The signal transduction and metabolic states could vary widely among individual cells. However, such cell-to-cell variation might be masked by the bulk measurements obtained from conventional biochemical methods. To assess the spatiotemporal dynamics of metabolism in individual intact cells, we developed genetically encoded biosensors based on fluorescent proteins.

As a key redox cofactor in metabolism, NADH has been implicated in the Warburg effect, the abnormal metabolism of glucose that is a hallmark of cancer cells. To date, however, sensitive and specific detection of NADH in the cytosol of individual live cells has been difficult. We engineered a fluorescent biosensor of NADH by combining a circularly permuted green fluorescent protein variant with a bacterial NADH-binding protein Rex. The optimized biosensor Peredox reports cytosolic NADH:NAD^+ ratios in individual live cells and can be calibrated with exogenous lactate and pyruvate. Notably pH resistant, this biosensor can be used in several cultured and primary cell types and in a high-content imaging format.

We then examined the single cell dynamics of glycolysis and energy-sensing signaling pathways using Peredox and other fluorescent biosensors: AMPKAR, a sensor

of the AMPK activity; and FOXO3-FP, a fluorescently-tagged protein domain from Forkhead transcription factor FOXO3 to report on the PI3K/Akt pathway activity. With perturbation to growth factor signaling, we observed a transient response in the cytosolic NADH-NAD^+ redox state. In contrast, with partial inhibition of glycolysis by iodoacetate, individual cells varied substantially in their responses, and cytosolic NADH:NAD^+ ratios oscillated between high and low states with a regular, approximately half-hour period, persisting for hours. These glycolytic NADH oscillations appeared to be cell-autonomous and coincided with the activation of the PI3K/Akt pathway but not the AMPK pathway. These results suggest a dynamic coupling between growth factor signaling and metabolic parameters. Overall, this thesis presents novel optical tools to assess metabolic dynamics – and to unravel the elaborate and complex integration of glucose metabolism and signaling pathways at the single cell level.

Table of Contents

ACKNOWLEDGMENTS

For the work presented in this dissertation, I would like to thank:

My family: Mom and Dad, Grandpa and Grandma, Keami and Kyle, my uncle, aunt, and cousins, for your love and patience through these years and across the thousands of miles.

Families and friends with whom I have stayed or kept in touch: the Arrudas, the Bennicis, the Cicovackis, the Hoppes, and the Lawlers, for your support and many wonderful home-made meals.

Friends, especially Timothy Hoppe, Jim Miller, Brian Bennici, Roseann Fitzgerald, Ariela Marshall, Brittany Murray, Tony Perez, Shawn Anthony, David Gellis, Shanthini Kasturi, Alex Grassian, Kyle Perry, David Thompson, and Jason Lohmueller.

The dissertation advisory committee: Joan Brugge, David Clapham, and Thomas Schwarz, for your invaluable advice and comments over the years.

The dissertation exam committee: Thomas Schwarz, Suzanne Gaudet, Matthew Vander Heiden, and Vamsi Mootha, for your reading of this work.

Nika Danial, Alfredo Gimenez-Cassina, Bernado Sabatini, and Jon Cohen for help and advice on metabolism, microscopy, and biochemistry over the years.

The BBS office, the MDPhD program office, the Neurobiology Department, and the Peabody society at HMS.

The Brugge lab, particularly John Albeck, for showing me the beauty of high-content imaging analysis, which made this grad school experience far more pleasant and

productive; Alex Grassian and Jon Coloff, for introducing me to the field of cancer metabolism; Rachel Davidowitz for your amazing art design and drawings, Greg Leya, for your help and companionship as we both wrote our theses around the same time.

The Yellen Lab, particularly Jim Berg, for teaching me the art of sensor engineering; also Mathew Tantama and Tanya Abramson, for your tremendous help over the years; and Geoff Tanner, Sujung Ryu, Daniel Kwan, Chiamaka Nwakeze, Juan Martinez-Francois, Andrew Lutas, Ricard Masia, and Becky Mongeon, for making the lab such a great and fun place to be.

And, most of all –

Gary, for your mentorship and guidance through these years. It is a great honor to learn from and work with you.

"Men work together," I told him from the heart,

"Whether they work together or apart." - Robert Frost

For 公公嫲嫲, *Tom & Pat*

Chapter I

Introduction: optical probes for metabolic signals

ABSTRACT

Concurrent with a renaissance in cell metabolism research, optical probes based on fluorescent proteins have been developed to report the spatiotemporal dynamics of metabolism. Such genetically encoded fluorescent sensors have become versatile and powerful tools to assess metabolic signals in individual intact cells. Here we review the general principles for sensor design, and we highlight several examples to detect key metabolic parameters, such as glucose, glutathione redox state, reactive oxygen species (ROS), adenosine triphosphate (ATP), AMP-dependent protein kinase (AMPK) activity, and nicotinamide adenine dinucleotide (NADH). While the field of metabolic sensor design is still at its infancy, these and upcoming probes may help us to elucidate the complex regulation of metabolism at the single cell level.

BACKGROUND

A Renaissance in Cell Metabolism Research

Cell metabolism refers to how cells handle their nutrients. It involves a collection of biochemical reactions to process carbohydrates, amino acids, and lipids to generate energy and synthesize essential cellular building blocks. Catalyzed by metabolic enzymes, each reaction transforms a substrate, be it the initial nutrient or an intermediate metabolite, into a product for the subsequent reaction. Together, these reactions constitute elaborate metabolic pathways for particular fuels, such as glycolysis to convert glucose into pyruvate, as well as β-oxidation to break down fatty acids. From a labyrinthine ensemble of metabolic pathways, cells derive energy and macromolecules to perform diverse physiological functions that encompass circadian rhythm (Asher and Schibler, 2011; Bass and Takahashi, 2010), cell proliferation (Buchakjian and Kornbluth, 2010; Lunt and Vander Heiden, 2011), cell survival (Vaughn and Deshmukh, 2008; Yi et al., 2011), and gene regulation (Zheng et al., 2003; Wellen et al., 2009). Metabolism thus provides the crucial housekeeping function for all cells.

A renaissance of interest in cell metabolism research is currently under way, driven in part by discoveries in cancer metabolism. Many types of tumors exhibited abnormal metabolism; despite the presence of oxygen, these tumors showed hallmarks of anaerobic glucose metabolism, with elevated levels of glucose uptake and lactate production (Warburg et al., 1927; Warburg, 1956). For decades, this phenomenon, known as the Warburg effect, has been exploited for clinical diagnostic imaging of tumors using ^{18}F-deoxyglucose with positron emission tomography (FDG-PET; Vander Heiden et al., 2009). Recently, the molecular underpinnings of cancer metabolism have begun to be

unraveled: cancer cells were found to harbor aberrations in metabolic enzymes in various pathways, for instance, pyruvate kinase M2 isoform (PKM2) in glycolysis (Christofk et al., 2008; Anastasiou et al., 2011) and phosphoglycerate dehydrogenase (PHGDH) in serine metabolism (Locasale et al., 2011; Possemato et al., 2011). Furthermore, known oncogenes and tumor suppressors, such as c-Myc and p53, were found to regulate metabolic pathways, thus connecting genetic alterations in tumors to their distinctive metabolism (Gao et al., 2009; Vousden and Ryan, 2009; Yuneva et al., 2012). Therefore, metabolic pathways emerge not only as potential contributing factors but also as therapeutic targets in cancer.

Beside oncology, there is a burgeoning interest in how metabolism can be exploited for therapy, for instance, in neurological disorders. Normally, the brain relies on glucose as the major fuel (Sokoloff et al., 1977). However, during a high-fat, low-carbohydrate diet known as the ketogenic diet, circulating ketone bodies increase in level, replacing glucose to support brain metabolism (Owen et al., 1967; Haymond et al., 1983). This fuel switch dramatically alters brain activity and has been used to treat refractory epilepsy (Vining 1999; Bailey et al., 2005). The anticonvulsant effect of the ketogenic diet is a clinical example that highlights the intimate connection between metabolism and brain function (Yellen, 2008).

Metabolic Measurements in Single Live Cells

Concurrent with this renaissance in metabolism research, several optical probes have been developed to report metabolic dynamics in live cells, providing single-cell measurements that could not be obtained with the conventional biochemical methods.

Indeed, biochemical studies from decades ago have already characterized the metabolic enzymes, substrates, and cofactors in major pathways, for instance, glycolysis and purine biosynthesis (Lowry and Passonneau, 1964; Krebs, 1977). However, since most of these studies require the use of tissue or cell extracts, each measurement reflects a cell population rather than an individual cell. This masks any differences among various cell types within the tissue (for instance, cancer cells and stromal cells in tumors, or neurons and glia in brain tissues), as well as any cell-to-cell heterogeneity within the same cell type. Optical probes circumvent this drawback by providing single cell measurements. In addition, while many components of the metabolic pathways have been defined biochemically, it is unclear how these components are integrated in the metabolic system as a whole, and how metabolite levels are regulated in an intact cell in the physiological settings. By providing measurements in intact cells, optical probes have become powerful tools for addressing systems level questions on cell metabolism.

This chapter will review optical probes for assessing the spatiotemporal dynamics of metabolism in this context of single intact cells. We will begin with strategies to engineer these probes, focusing on genetically encoded fluorescent sensors. Next, we will consider various aspects of sensor design, such as sensitivity, specificity, and calibration. Finally, we will review sensor examples that have been used to detect metabolic parameters, including glucose, glutathione redox state, reactive oxygen species (ROS), adenosine triphosphate (ATP), AMP-dependent protein kinase (AMPK) activity, and nicotinamide adenine dinucleotide (NADH). Although this review is in no way comprehensive, we hope to give our readers a sense of how to design, utilize, and evaluate optical probes of cell metabolism.

Fluorescence and Fluorescent Proteins

As many optical probes reveal the inner workings of the cell via fluorescence, we will briefly review some of its basic concepts. Fluorescence is an optical phenomenon in which light absorption by a molecule (or "fluorophore") triggers its transition from the ground state to excited state(s), followed by a return to the ground state and light emission (Lakowicz, 2006). The brightness of a fluorophore is determined by its extinction coefficient (how efficiently it absorbs light) and quantum yield (how efficiently the absorbed light is converted into the emitted light). To assess fluorescence, the most common method is to measure its intensity. Although the intensity of a fluorescent probe depends on both brightness and concentration, if the probe is ratiometric, one can normalize its measurements by dividing its signal acquired at one excitation or emission wavelength by its signal at another wavelength (Nagai et al., 2001; Berg et al., 2009). Alternatively, one can use fluorescence lifetime for quantification. Defined as the average time between fluorophore excitation and return to the ground state, fluorescence lifetime is largely independent of the fluorophore concentration and thus provides a self-normalized measurement (Lakowicz, 2006). Though technically more demanding, fluorescence lifetime imaging (FLIM) has been used in conjunction with biosensors to report intracellular events (Haj et al., 2002; Lee et al., 2009; Tantama et al., 2011).

For intensity or lifetime measurements, fluorescent probes are typically based on either small molecules or fluorescent proteins (FPs). Small molecule indicators have been engineered to report metabolic signals such as pH and ROS (Han and Burgess, 2010; Wardman, 2007). Nevertheless, a major challenge of using these indicators remains in

delivering them into cells, as well as ensuring sufficient retention for imaging. Compared with small molecule indicators, FP-based probes can be introduced into cells genetically and are more versatile for intracellular applications.

Green fluorescent protein (GFP) and its numerous color variants have become indispensable optical tools for assessing protein location and intracellular events. Despite its origin from the jellyfish *Aequorea victoria* (Shimumora et al., 1962), GFP can be expressed in various cell types in other organisms (Chalfie et al., 1994). GFP fluorescence comes from the chromophore, which resides on a central α-helix surrounded by a barrel of 11 β-strands (Ormö et al., 1996; Yang et al., 1996). The chromophore is formed from spontaneous cyclization and oxidation of a tripeptide in the central α-helix, and this maturation process requires molecular oxygen (Tsien, 1998). Starting from *Aequorea* GFP and GFP-like proteins of other organisms, FPs with a variety of colors and photophysical properties have been generated (Shaner et al., 2005; Day and Davidson, 2009). Some of these FPs have been utilized to create reporters of intracellular events. Because FP-based reporters are genetically encoded, once the encoding plasmid DNA is delivered into cells by transfection or viral transduction, the reporters will be synthesized and retained in the cells. These fluorescent reporters can be fused to organelle-targeting sequences, revealing metabolic dynamics in specific subcellular compartments (Miyawaki et al., 1997; Merksamer et al., 2008; Tsou et al., 2011). Furthermore, transgenic animals can be generated to express these FP-based reporters in defined cell types via cell-specific promoters (Guzman et al., 2010) or broadly in all cells (Albrecht et al., 2011), allowing the imaging of specific metabolic parameter *in vivo*.

Overall, genetically encoded fluorescent sensors have become powerful and versatile optical tools in cell biology. While they can be engineered by various approaches (Giepmans et al., 2006; Frommer et al., 2009; Palmer et al., 2011; Tantama et al., 2012), the following section will focus on four of the most common designs: FP translocation reporters, environmentally sensitive FP reporters, fluorescence resonance energy transfer (FRET) sensors, and circularly permuted fluorescent protein (cpFP) sensors.

DESIGN STRATEGIES FOR FLUORESCENT SENSORS OF METABOLISM

1. FP translocation reporters

Upon detecting certain metabolic signals and ions, many proteins alter their intracellular locations. By tagging these protein domains with FPs and tracking their translocation, one can monitor these signals. For instance, phosphatidylinositol 4,5-bisphosphate can be detected by using GFP-tagged pleckstrin homology (PH) domain of phospholipase C, which upon ligand binding transiently moves from the cytosol to the plasma membrane (Stauffer et al., 1998; Raucher et al., 2000). Reporters based on FP translocation have also been used to monitor metabolites such as diacylglycerol (Oancea et al., 1998; Oancea and Meyer, 1998), inositol 1,4,5-triphosphate (Hirose et al., 1999), and phosphatidylserine (Yeung et al., 2008). Nonetheless, for specific sensing, the scaffold proteins need to be chosen carefully, as many of them respond to multiple signals, the most common of which is the intracellular calcium.

2. Environmentally sensitive FP reporters

Although the FP β-barrel protects the chromophore from the bulk solvent, mutations or circular permutation can render the FP environmentally sensitive. Even though wild-type *Aequorea* GFP is fairly pH-resistant, mutations can be engineered to make it sensitive to physiological pH changes, suitable for intracellular imaging (Llopis et al., 1998; Miesenböck et al., 1998). GFP variants have been designed to detect intracellular anions such as chloride (Jayaraman et al., 2000) or to monitor intracellular chloride and pH simultaneously (Arosio et al., 2010). Besides pH and chloride, FPs can be designed to sense thiol-disulfide redox. Cysteine residues can be engineered near the chromophore to yield redox sensitive FPs, rxYFP and roGFP (Ostergaard et al., 2001; Dooley et al., 2004); these FPs can be used to assess general thiol-disulfide redox state in different subcellular compartments (Hanson et al., 2004; Merksamer et al., 2008). In addition, environmentally sensitive FPs can be created by circular permutation (see below, cpFP sensors). Circularly permuted YFP has been used to detect superoxide (Wang et al., 2008), though the sensing mechanism remains unclear. Given the few environmentally sensitive FP reporters and their particular designs, it may be difficult to generalize this approach to sense other metabolic ligands or parameters.

3. Fluorescence resonance energy transfer (FRET) sensors

Numerous genetically encoded FP-based sensors have been designed based on fluorescence (or Förster) resonance energy transfer (FRET). A common strategy to establish FRET involves using a pair of fluorophores, a donor and an acceptor, with spectral overlap between donor emission and acceptor absorption. When the two

fluorophores are in close proximity to each other, donor excitation would lead to fluorescence emission of the acceptor via FRET. The efficiency of FRET varies with both the distance between the fluorophores and their relative orientations (Zhang et al., 2002a; Campbell, 2009). For a genetically encoded FRET sensor, the two FP fluorophores, for instance CFP and YFP, can be fused either separately to two protein domains (bimolecular or intermolecular FRET) or both to a single domain (unimolecular or intramolecular FRET). Upon sensing the parameter of interest, the reporter undergoes conformational changes that alter the relative distance and/or orientation of the two FP fluorophores, creating changes in FRET (Miyawaki, 2011). After the first FP-based reporters for calcium (Miyawaki et al., 1997; Romoser et al., 1997), hundreds of genetically encoded FRET sensors have been engineered to report intracellular parameters, including protein kinase activation, membrane receptor dimerization, small ions and molecules (Frommer et al., 2009; Herbst et al., 2009; Vinkenborg et al., 2009), as well as – pertinent to cell metabolism research – glucose level (Fehr et al., 2003; Takanaga et al., 2008), ATP level (Imamura et al., 2009), and AMPK activity (Tsou et al., 2011).

With limited dynamic range in the fluorescence response, many genetically encoded FP-based FRET sensors could be difficult to use. Typically, the dynamic range in many FRET sensors could be as low as 5% to 10%. Compared to such dynamic range, signal variations across cells at baseline as well as noise variations could be substantial, making it difficult to acquire robust and accurate measurements. There have been efforts to improve the dynamic range of FRET sensors by varying the FP reorientation via

circular permutation (Nagai et al., 2004) or by varying linker length (Hires et al., 2008; Komatsu et al., 2011).

4. Circularly permuted fluorescent protein (cpFP) sensors

Circularly permuted fluorescent protein (cpFP) has become part of the standard repertoire in the FP sensor design. Circular permutation of a GFP involves linking its original amino and carboxyl termini with a polypeptide and then introducing new termini elsewhere in the protein, such as near the chromophore (Baird et al., 1999). When a cpFP is fused to a ligand-binding protein domain, this creates a conformational coupling between ligand binding and cpFP fluorescence (Nagai et al., 2001). Based on this strategy, cpFP sensors have been engineered to report calcium, hydrogen peroxide, cyclic 3′,5′-guanosine monophosphate (cGMP), ATP:ADP ratio, and NADH-NAD^+ redox state (Nagai et al., 2001; Belousov et al., 2006; Nausch et al., 2008; Berg et al., 2009; Zhao et al., 2011b; Hung et al., 2011). Typically, cpFP sensors require only single FPs to work and are spectrally ratiometric. For those that are not so, a second FP could be attached in tandem for ratiometric imaging (Shimozono et al., 2004; Hung et al., 2011). Compared to most published FRET sensors, cpFP sensors generally show greater dynamic range, in some cases ~20 fold increase in fluorescence response, that is, 2000% change (Souslova et al., 2007; Zhao et al., 2011a).

Most cpFP sensors are notably pH sensitive, and this poses a challenge to obtaining accurate measurements for cell metabolism research. The pK_a's in most cpFP sensors are near the physiological pH range (Nagai et al., 2001; Belousov et al., 2006; Nausch et al., 2008; Wang et al., 2008; Berg et al., 2009; Zhao et al., 2011b). Since

metabolic manipulations often perturb intracellular pH, occasionally by as much as 0.5 units (Llopis et al., 1998; Tantama et al., 2011), this would produce a substantial response in many cpFP sensors, aliasing a bona fide change in the nominal analyte. As a somewhat ironic example to highlight this pH artifact, a sensor for mitochondrial pH has been engineered by spoiling the ligand sensing in a cpFP sensor (Poburko et al., 2011). To correct for the pH sensitivity of many cpFP sensors, one can monitor intracellular pH using a red small molecule indicator (Berg et al., 2009) or a red FP (Tantama et al., 2011); both the pH readout and the cpFP signal can then be spectrally compatible and concurrently measured. An alternative, simpler solution is to start with other cpFP variants with lower pK_a to engineer a sensor that is fairly pH resistant (Hung et al., 2011).

The four types of sensor design – FP translocation, environmentally sensitive FP, FRET and cpFP – are not mutually exclusive, and a single probe can incorporate multiple sensing strategies. For instance, a cpFP sensor for hydrogen peroxide can be fused to a modified PH domain that undergoes translocation upon phosphatidylinositol 3,4,5-trisphosphate (PIP3) binding (Mishina et al., 2012). This single probe can be used to monitor both hydrogen peroxide and PIP3 simultaneously using distinct readouts: its fluorescence response reports hydrogen peroxide, whereas its intracellular distribution reports PIP3.

BASIC PRINCIPLES OF METABOLIC SENSOR DESIGN

While genetically encoded fluorescent sensors are powerful tools to assess metabolism in single live cells, there are caveats and questions associated with these

tools: How can one design or evaluate a fluorescent sensor of metabolism? What kinds of attributes are desirable or undesirable, with regard to its affinity, specificity, and kinetics? How can one convert its measurements into biologically meaningful parameters? These questions are important, as the sensor design and its usage underlie the accuracy and the meaning of its measurements. Currently, not many fluorescent sensors have been used beyond their laboratories of origin in published studies (Lemke and Schultz, 2011), as some of these sensors have not been carefully vetted, and the investment needed to master the imaging techniques might not be trivial. Through the following discussion, we hope to give our readers a sense of how to design or evaluate these sensors, to understand their power and limits, and to utilize them effectively in cell metabolism research.

FP characteristics and sensor engineering

The reliability of a genetically encoded fluorescent sensor depends critically on the component FP(s). Given numerous FPs with distinct colors and features (Shaner et al., 2005; Day and Davidson, 2009), one could look for the following desirable characteristics:

(1) Optimal brightness and color: The FP should be far brighter than the endogenous autofluorescence. Typically, for live-cell microscopy, the autofluorescence background is higher in the blue wavelength region (Wagnières et al., 1998). Thus, a blue FP would need to be brighter than a red FP for comparable signal detection.

(2) Ratiometric signal with large dynamic range: This is not an intrinsic property of the FP alone but rather of the FP-based sensor. As calculated from fluorescence measurements at two wavelengths, a ratiometric signal not only normalizes for sensor

concentration but also reduces artifacts due to changes in cell volume or cell movement (Nagai et al., 2001; Berg at al., 2009). Besides ratiometric signal, a large dynamic range facilitates sensor imaging, particularly given large noise and signal variations.

(3) High photostability: FPs that are photostable, or resistant to photobleaching, are extremely useful for long-term imaging. Though some FPs exhibit complex photobleaching curves (Shaner et al., 2005) and can be difficult to use in quantitative experiments.

(4) Fast maturation: Slowly maturating FPs can be difficult to express in mammalian cells in physiological temperatures (Tsien, 1998). Fortunately, FPs with improved maturation have been engineered (Nagai et al., 2002; Shaner et al., 2004) and are more suitable.

(5) Lack of oligomerization or aggregation: As some FPs, particularly of the coral family, often oligomerize and aggregate in cell cultures and *in vivo* (Yanushevich et al., 2002; Hirrlinger et al., 2005; Katayama et al., 2008), the resulting fluorescent puncta render imaging experiments difficult. Monomeric FPs are preferable.

(6) Lack of photoconversion: Many FPs can exhibit photoconversion, in which excitation at certain wavelengths changes the FP color, for instance, from yellow to cyan, red to green, or orange to far-red (Valentin et al., 2005; Kirber et al., 2007; Kremers et al., 2009). Depending on the instrumentation and the protocols, photoconversion may be evident only in some cases (Kremers et al., 2009). Ideally, FPs that can undergo photoconversion should be avoided.

(7) Lack of environmental sensitivity: Except when intended (as in environmentally sensitive FP sensors), the FP should be resistant to fluctuations in the

intracellular environment. The main factors to consider include pH and concentrations of anions such as chloride. Some FPs are notoriously pH-sensitive or chloride-sensitive (Griesbeck et al., 2001; Shaner et al., 2005) and should be avoided. In addition to the FP, the metabolite-sensing protein domain can be environmentally sensitive; in the end, an FP-based sensor should be carefully checked for potential interference before intracellular applications.

Regardless of the strategy (FRET- or cpFP-based), designing a sensor remains an empirical endeavor. While there are innumerable ways to combine an FP and a metabolite-sensing protein domain, only a small fraction may make useful sensors in the end. Initially, one can vary the lengths or the compositions of the peptide linkers, optimize the metabolite-sensing protein domain(s) by mutation or truncation, or screen iteratively for responsive candidates. Once identified, promising variants can be characterized and improved upon to yield the eventual genetically encoded FP-based sensor.

Sensor tuning and sensitivity

The sensor should be tuned to the appropriate range for the parameter of interest. For instance, for a pH indicator to work in cells effectively, its pK_a should lie within the range of intracellular pH. In general, for a sensor of metabolic ligand A, its dissociation constant (K_d, defined as the concentration of A needed for a half maximal sensor response) should be near the intracellular concentration of A; otherwise, the sensor response could be undetectable or minimal. Thus, the sensor should be sensitive, recording whenever the parameter of interest changes.

Nonetheless, for sensor design, the intracellular concentrations of metabolites measured by biochemical studies may not be applicable, as the molecules may be concentrated in subcellular compartments or microdomains. Furthermore, a substantial fraction of these molecules can be reversibly bound to cellular proteins and thus not accessible to the biosensor. For a sensor of ligand A, its K_d should thus be tuned not to the total concentration of A, but rather to the free concentration of A. If this free concentration is known or can be estimated, one can design a reporter with its K_d based on that information. Alternatively, from variants with different affinities, one can empirically test for the optimal sensor response in cells.

Most metabolite-sensing protein domains are under complex regulation of several ligands rather than a single one; in the end, such protein domains may elegantly detect the relevant energetic parameters. For instance, a bacterial ATP-binding protein Glnk1 has been found to bind both ATP and ADP with extremely high affinity in the submicromolar range, in such a way that it reports a major energetic parameter, the ATP:ADP ratio (Berg et al., 2009). As another example, a bacterial NADH-binding protein Rex has been found to bind both NADH and NAD^+ with remarkable pH sensitivity; Rex turns out to report the parameter $[NADH]/[NAD^+]\times[H^+]$, which reflects the redox potential of NAD(H) dependent dehydrogenases (Hung et al., 2011). Therefore, when working with protein domains, one should determine if they are already tuned to endogenous metabolic parameters, as well as if that can be exploited to engineer fluorescent sensors of cell metabolism.

Sensor specificity and kinetics

Besides appropriate tuning, a sensor should be specific, recognizing the target ligand(s) and ignoring all others. The sensor specificity depends on both its affinity for the target as compared with interfering ligands, as well as the abundance of the target as compared with interfering ligands. Accordingly, it can be difficult to create sensors specific for rare metabolites, due to competition from interfering ligands of high abundance. For specificity assessment, one should test if the interfering ligands activate the sensor alone, as well as if they compete with the target to modulate the sensor response.

A sensor should also be fast. Genetically encoded fluorescent sensors – based on FP translocation, environmentally sensitive FP, FRET, or cpFP – are typically so, capable of detecting dynamics changes with a time resolution of seconds or less.

Detection limit

As a sensor is expressed in cells, its intracellular concentration imposes a detection limit on its metabolic measurements. For FP-based sensors that work by direct ligand binding, when the concentration of sensor exceeds that of the ligand, the sensor response can be limited by stoichiometric binding and not by ligand titration. Typically, most FP-based sensors are expressed at 1 to 10 micromolar (Niswender et al., 1995; Akerboom et al., 2009). For rare metabolic ligands, such as at low nanomolar concentrations, at best only ~0.1% of the sensors can bind the ligands at a given time. Thus, for FP-based biosensors, the target ligands should be far more abundant, in the submillimolar to millimolar range.

For detection of rare metabolites, this concentration limit can be overcome by an amplification scheme. Using enzymatic catalysis, primary signals from direct ligand binding can be amplified to stronger secondary signals. For instance, detection of nitric oxide (NO) at extremely low, picomolar concentrations can be achieved by expressing in cells both soluble guanylate cyclase and an FP-based cGMP reporter (Sato et al., 2006). Upon binding of minute amounts of NO, the amplified generation of cGMP by guanylate cyclase leads to detectable signals in the cGMP reporter.

Measurement calibration

To assess a metabolic parameter of interest using a sensor in live cells, one should note whether the measurement is qualitative or quantitative. For qualitative use, the sensor reports *relative* changes of the parameter; whereas, for quantitative measurements, one could determine the *actual* metabolic parameter, such as an NADH:NAD^+ ratio of 0.1.

Quantitative measurements can be obtained only after careful calibration of the sensor signals in the intracellular milieu. For sensor calibration, cells are maintained in several metabolic conditions where the corresponding values of the parameter of interest are known, and the sensor signals are measured to generate a standard curve; the imaging data can then be converted into biologically meaningful measurements. One can also check if the sensor behaves as expected, by comparing the calibration data in cells with the biochemical data from purified sensor proteins. While the standard curve should contain several points, a major challenge in sensor calibration is to settle on the metabolic conditions that present well-defined parameters and are experimentally feasible.

Occasionally, when one can obtain only a single calibration point in cells, one may incorporate the purified protein data to generate a standard curve, by assuming similar sensor behaviors in cells as in purified proteins. How often a sensor should be calibrated depends on the variability of its behavior among individual cells and/or experiments in identical metabolic states. If such variations are small, calibration data from one set can be applicable to other sets. Otherwise, calibration should be conducted on a cell-by-cell or experiment-by-experiment basis, for instance at the end of each imaging experiment. Overall, only through sensor calibration can one derive from the fluorescence data the actual metabolic parameters of interest.

Several FP-based sensors of metabolism can be routinely calibrated to yield quantitative measurements; examples include pH sensors and redox sensors. To calibrate pH sensors, one can use a combination of ionophores to clamp intracellular pH at various values (Llopis et al., 1998; Tantama et al., 2011). For calibration of general thiol redox sensors of the roGFP family (Dooley et al., 2004; Hanson et al., 2004) or the glutathione sensor Grx1-roGFP2 (Gutscher et al., 2008), one can utilize oxidants such as hydrogen peroxide and reducing agents such as dithiothreitol (DTT) to generate maximal and minimal sensor responses. Finally, for calibration of the cytosolic NADH-NAD^+ redox sensor Peredox (Hung et al., 2011), one can supply cells with a mixture of lactate and pyruvate, but without glucose. By using different lactate:pyruvate ratios and exploiting the endogenous lactate dehydrogenase reaction, one can poise the cytosolic NADH-NAD^+ redox state in cells, and the sensor can be shown to exhibit similar behaviors in cells and in purified proteins.

Potential toxicity and perturbations

Expression of any proteins, including fluorescent biosensors, may adversely affect cell physiology. In addition to potential FP misfolding and aggregation, the biosensor may interact with endogenous proteins, although such possibility of signaling cross-talk could be minimized by using protein scaffolds from other organisms. Also, since most metabolic sensors detect their ligands by direct binding or via enzymatic reactions, such buffering or catalysis may drastically alter the metabolite levels and perturb cell physiology. To avoid these adverse effects, the sensor expression should ideally be maintained at the lowest level that is sufficient for imaging; also, the imaging data should be checked for any dependence on the level of the sensor expression.

EXAMPLES OF GENETICALLY ENCODED METABOLIC BIOSENSORS

After considering the basic principles in sensor design, we will focus on examples of sensors to monitor the following parameters: glucose, general and glutathione redox state, reactive oxygen species (ROS), adenosine triphosphate (ATP), AMP-dependent protein kinase (AMPK) activity, and nicotinamide adenine dinucleotide (NADH).

Glucose

Glucose is one of the major carbon sources for energetics and biosynthesis. After entering cells via specialized transporters (Carruthers, 1990), glucose is phosphorylated and metabolized by diverse pathways: glycolysis, glycogen synthesis, pentose phosphate pathway, and glycosylation pathway (Vander Heiden et al., 2009; Wellen et al., 2010).

Intracellular level of glucose can thus exert profound effects on cell metabolism and signaling.

Fluorescent analogs of glucose can be used to assess glucose in single live cells. Intracellular accumulation of these glucose derivatives, such as 2-[N-(7-nitrobenz-2-oxa-1,3-diazol-4-yl)amino]-2-deoxy-D-glucose (2-NBDG), can be optically monitored to estimate glucose uptake (Yoshioka et al., 1996; Yamada et al., 2000; Loaiza et al., 2003). However, these compounds may exhibit unconventional uptake behaviors by the glucose transporters (Barros et al., 2009). Besides, for accurate measurements of intracellular 2-NBDG, careful control of perfusion is needed to reduce the background of extracellular 2-NBDG (Yamada et al., 2007).

Genetically encoded fluorescent sensors of glucose have been used to monitor intracellular glucose level and glycolytic flux. Each of these sensors is constructed by flanking a bacterial periplasmic glucose/galactose binding protein with two FPs of a FRET pair, such that binding of glucose alters the FRET signal (Fehr et al., 2003; Hou et al., 2011). Among the published sensor variants, FLII^{12}Pglu700μΔ6 (also known as FLII^{12}Pglu600μΔ6) may be the most useful in mammalian cells; its K_d for glucose is ~600-700 μM (Takanaga et al., 2008). Using this fluorescent glucose sensor, one can assess the intracellular glucose level as well as the flux of glycolysis (Bittner et al., 2010; Bittner et al., 2011). Glycolytic flux, or technically the rate of glucose elimination by metabolism, has been estimated by abruptly lowering extracellular glucose or inhibiting glucose transport, then monitoring changes in the intracellular glucose level using the biosensor. Nevertheless, for accurate determination of glucose level and its elimination rate, proper calibration of the sensor response is essential. In this case, it would not

suffice to rely on data from purified proteins, as the glucose sensor appears to behave differently in purified proteins compared with in cells (Takanaga et al., 2008).

General thiol-disulfide and glutathione redox state

Reduction and oxidation (redox) reactions abound in the intracellular environment. To transfer reducing equivalents in biochemical reactions, cells utilize numerous sets of redox couples, such as NADH-NAD^+, NADPH-$NADP^+$, and the glutathione system. Each redox system performs distinct metabolic functions, and its spatiotemporal dynamics is tightly regulated (Meyer and Dick, 2010). Redox sensitive FP and its variants have been used to monitor the cellular thiol redox states. In the rxYFP and roGFP family of proteins, oxidation of two cysteine thiols near the FP chromophore alters its fluorescence (Ostergaard et al., 2001; Dooley et al., 2004). This redox sensing is reversible, due to regeneration of free thiols by endogenous antioxidants. These redox sensitive FPs can thus report the dynamics of the general thiol-disulfide redox in live cells. Because of their ratiometric spectral responses, roGFP variants are more widely used; they have been targeted to various subcellular compartments for redox monitoring (Hanson et al., 2004; Merksamer et al., 2008; Guzman et al., 2010). While detection by roGFP alone is not specific for any redox couple, a fluorescent sensor specific for the glutathione redox state can be engineered using roGFP. Connecting roGFP2 to the human glutaredoxin Grx1 via a peptide linker facilitates rapid equilibration between the thiol redox state of the FP and the glutathione redox state in the intracellular environment (Gutscher et al., 2008). The resulting sensor Grx1-roGFP2 can report glutathione redox dynamics associated with various physiological stimuli. Also, transgenic *Drosophila*

expressing Grx1-roGFP2 has been generated to assess the glutathione redox state in various tissues during development and aging (Albrecht et al., 2011). Overall, fluorescent probes based on roGFP variants have become convenient and versatile tools to study redox signaling.

ROS

Continuously generated by oxidative metabolism, reactive oxygen species (ROS) are key mediators in diverse physiological processes and pathologies (Balaban et al., 2005; Winterbourn, 2008; Murphy et al., 2011). ROS can be detected using various small molecule indicators (Wardman, 2007). In addition, genetically encoded fluorescent sensors have been used to study the spatiotemporal dynamics of certain ROS metabolites, such as hydrogen peroxide and superoxide. Currently, for detection of hydrogen peroxide, there are two fluorescent sensors with distinct designs: On one hand, the sensor HyPer is constructed by combining a cpFP with a bacterial peroxide-sensing domain OxyR (Belousov et al., 2006); oxidation of two cysteine thiols in OxyR alters the sensor conformation and the cpFP fluorescence. On the other hand, the sensor roGFP2-Orp1 is constructed by linking roGFP2 to the yeast peroxiredoxin Orp1 (Gutscher et al., 2009). Here, roGFP2-Orp1 senses hydrogen peroxide via a redox relay mechanism similar to that of the glutathione sensor Grx1-roGFP2. Both HyPer and roGFP2-Orp1 respond to hydrogen peroxide specifically and give a ratiometric fluorescence response. Interestingly, detection of superoxide can be achieved using a cpFP variant cpYFP alone, with no conjugation to any ROS recognition domain (Wang et al., 2008). cpYFP has been used to visualize superoxide flashes in mitochondria in mammalian cells. Yet, the

mechanism of how superoxide interacts with the cpYFP chromophore, as well as whether this interaction is specific, remains unclear. Finally, similar to many cpFP reporters, cpYFP and HyPer are sensitive to changes in physiological pH (Belousov et al., 2006; Wang et al., 2008), and pH should be monitored to rule out artifacts.

ATP

Adenosine triphosphate (ATP) is the currency for bioenergetics: Energy for cellular reactions is supplied by conversion of ATP into related cofactors, adenosine diphosphate (ADP) and adenosine monophosphate (AMP). In intracellular environments, as the free ATP:ADP ratio is kept far from the chemical equilibrium (Nicholls and Ferguson, 2002), it can be utilized to do work and drive biosynthetic reactions. For bioenergetics, what matters is not the total amounts of ATP alone, but rather the free ATP:ADP or ATP:AMP ratios (Atkinson, 1968; Pradet and Raymond, 1983). While total ATP:ADP ratios can be chemically determined, this may underestimate the free ATP:ADP ratios, as relatively more ADP is bound to cellular proteins (Mörikofer-Zwez et al., 1989).

Indirect and direct methods have been devised to assess ATP levels in live cells. ATP can be monitored indirectly via Mg^{2+} measurements. Due to stronger binding of Mg^{2+} by ATP than ADP, changes in ATP levels can be accompanied by reciprocal changes in Mg^{2+} levels, which can be detected with a small molecule indicator (Jung et al., 1990; Harman et al., 1990). Yet, this signal can be aliased by ATP-independent changes in Mg^{2+} levels. In addition, ATP can be measured directly using a luciferase reporter system to generate ATP-dependent luminescence. This approach has been used

to detect cytosol and mitochondrial ATP in single cells (Kennedy et al., 1999; Jouaville et al., 1999). However, the luminescence signal can be limited and requires a sensitive photon-counting charge coupled device (CCD) camera for detection, and consumption of ATP in this method may perturb cell metabolism.

Genetically encoded biosensors of ATP and ATP:ADP ratio have been engineered using FPs with ATP-binding protein domains. Unlike the luciferase method, these sensors do not consume ATP, and their signals are far brighter. Interestingly, physiological amounts of ATP can alter the fluorescence of a CFP-YFP FRET pair or the lifetime of CFP alone (Willemse et al., 2007; Borst et al., 2010), though this has not yet been used to measure ATP in live cells. Instead, ATP-binding protein domains have been used in conjunction to create reporters of ATP and related energetic parameters: A fluorescent sensor of cellular ATP:ADP ratio has been designed by linking a cpFP to a bacterial protein Glnk1 (Berg et al., 2009). As Glnk1 binds ATP and ADP with high affinity but with distinct conformations, the resulting sensor Perceval effectively reports the free ATP:ADP ratio. It has been used to monitor dynamic changes in the ATP:ADP ratio in mammalian cells upon energetic challenges. Currently, this sensor is tuned to detecting fairly low ATP:ADP ratios of <1. Although suitable for use in sensing energy deficits or in certain cell types, it may not be responsive in most mammalian cells, which typically have higher resting ATP:ADP ratios. Also, like many cpFP sensors, Perceval can be pH sensitive and requires correction. To account for pH interference, one would need to measure the sensor signals together with pH using a spectrally compatible dye indicator (Berg et al., 2009) or a red pH biosensor, pHRed (Tantama et al., 2011). Aside from the ATP:ADP ratio, intracellular ATP can be measured using genetically encoded

biosensors for ATP (Imamura et al., 2009). Known as the ATeams, these sensors have been created using a FRET strategy, with the ε-subunit of a bacterial F_0F_1-ATP synthase flanked by two FPs of a FRET pair; binding of ATP alters the protein conformation and FRET. Together they cover a broad range of affinities for ATP, and they can report ATP levels in distinct subcellular compartments and upon energetic challenges. By using different FPs, an ATeam variant has been designed to be spectrally compatible with fura-2, allowing simultaneous imaging of both ATP and calcium (Nakano et al., 2011). As these FP-based sensors show notable pH sensitivity in dynamic range and ATP binding affinity, pH should be measured concurrently with sensor measurements or in parallel to rule out pH artifacts.

AMPK activity

The AMP-activated protein kinase (AMPK) is a master regulator of metabolism, and its dysregulation has been implicated in various metabolic and neoplastic diseases (Sarbassov et al., 2005; Shaw and Cantley, 2006). Upon energy challenges, AMP level increases, leading to allosteric activation of AMPK (Hardie, 2004). With multiple downstream targets, AMPK maintains energy balance by promoting catabolic processes such as fatty acid oxidation, inhibiting macromolecule biosynthesis, and coordinating diverse physiological processes including autophagy, mitochondrial biogenesis, and cell division (Hardie, 2004; Reznick and Shulman, 2006; Banko et al., 2011; Mihaylova and Shaw, 2011).

The spatiotemporal dynamics of AMPK activity can be monitored in single cells using a genetically encoded fluorescent sensor. Similar to other biosensors of kinase

activity (Allen and Zhang, 2006; Gallegos et al., 2006), this sensor of AMPK activity is based on FRET, with two FPs of a FRET pair linked to an optimized substrate peptide together with a phospho-threonine binding domain FHA1 (Tsou et al., 2011). Upon AMPK activation, the phosphorylated peptide binds to the FHA1 domain, altering the sensor conformation and FRET. This fluorescent sensor AMPKAR yields reversible FRET signal changes, because the phosphorylated peptide can be acted upon by endogenous phosphatases; thus, AMPKAR technically detects the balance of activity between AMPK and endogenous phosphatases. To check for sensor specificity, the phosphorylation site on the peptide can be spoiled as a control. Using AMPKAR, one can examine the dynamics and the heterogeneity of AMPK activity among individual cells. Depending on the stimuli, AMPK activation occurs in distinct subcellular compartments: While calcium elevation leads to AMPK activation both in the cytosol and the nucleus, application of 2-deoxyglucose induces AMPK activation that is confined to the cytosol only. In addition, AMPKAR has been used to track AMPK activity during cell division, showing that AMPK coordinates energetic status with mitotic regulation (Banko et al., 2011).

NADH

Nicotinamide adenine dinucleotide (reduced: NADH; oxidized NAD^+) is a key cofactor in redox reactions. In mammalian cells, NADH-NAD^+ redox environments vastly differ between the cytosol and the mitochondrial matrix (Nicholls and Ferguson, 2002), involving distinct metabolic pathways, for instance, glycolysis in the cytosol and the tricarboxylic acid (TCA) cycle in mitochondria. Also, there are dedicated systems to

transfer reducing equivalents of NADH from the cytosol into mitochondria (Schoolwerth and LaNoue, 1985).

Although NADH can be measured using biochemical methods or autofluorescence, these traditional approaches have drawbacks. With biochemical determination one can indirectly measure the free NADH:NAD^+ ratio, the pertinent parameter in redox reactions. Though NADH and NAD^+ can be directly extracted, such measurements of total NADH:NAD^+ ratios greatly overestimate the actual free NADH:NAD^+ ratios, as a greater fraction of NADH than NAD^+ is protein-bound (Williamson et al., 1967; Zhang et al., 2002b). Instead, by assuming a constant, known pH and exploiting a dehydrogenase reaction presumably at equilibrium (such as the lactate dehydrogenase), one can use the ratio of that redox couple (the lactate:pyruvate ratio) to infer the free NADH:NAD^+ ratio (Williamson et al., 1967). However, this is not a single-cell measurement, but rather an average from millions of cells. Alternatively, autofluorescence imaging can be used to assess NADH in single cells, but it has several limitations: First, it cannot distinguish between NADH and a related cofactor NADPH (Rocheleau et al., 2004); distinction between these two cofactors is crucial, as they govern different redox reactions (Klingenberg and Bücher, 1960). Second, since autofluorescence mostly comes from protein-bound forms of the cofactors, intracellular changes such as pH can alter the signal by affecting the NAD(P)H-protein interactions (Ogikubo et al., 2011). Third, this method cannot yield the free NADH:NAD^+ ratio. Finally, mitochondrial signals often dominate the measurements, whereas cytosolic autofluorescence is notably weak (Patterson et al., 2000).

To overcome the drawbacks above, two groups have independently created FP-based sensors of NADH (Hung et al., 2011; Zhao et al., 2011b). Although both groups adopted a cpFP strategy using the bacterial NADH-binding protein Rex, their sensors differ in properties and in the redox parameters they detect. In the first report, while a cpFP inserted into Rex reports the parameter $[NADH]/[NAD^+]\times[H^+]$, the optimized sensor Peredox measures the cytosolic free $NADH:NAD^+$ ratio in mammalian cells (Hung et al., 2011). Based on a cpFP variant T-Sapphire with a low pK_a (Zapata-Hommer and Griesbeck, 2003), Peredox response is notably pH resistant, unlike many other cpFP sensors. With high-content image analysis, it can report dynamics of glycolysis as indicated by cytosolic free $NADH:NAD^+$ ratios in hundreds of live cells. With its current affinity, Peredox is tuned to sensing $NADH:NAD^+$ ratios in the cytosol but not in the mitochondrial matrix, where free $NADH:NAD^+$ ratios can be 100- to 1,000-fold higher (Williamson et al., 1967). In contrast, in the second report, the fluorescent sensor Frex detects the NADH level, rather than the $NADH:NAD^+$ ratio (Zhao et al., 2011b). The sensor was constructed by combining a cpYFP with part of the Rex protein. After targeting into the mitochondrial matrix, the sensor reveals mitochondrial NADH changes during energetic or peroxide challenges. To account for pH interference on Frex signals, cpYFP alone has been used as a control in parallel experiments; though briefly mentioned, the effect of pH on NADH binding in Frex has not been accounted for. Overall, as genetically encoded fluorescent sensors, Peredox and Frex may be used to reveal cytosolic and mitochondrial $NADH\text{-}NAD^+$ redox dynamics in single cells with unprecedented details. When used in conjunction with other fluorescent reporters, they may allow us to obtain an integrated view of metabolic dynamics and its regulation.

CONCLUSION AND FUTURE DIRECTIONS

In this chapter, we have reviewed the basic design principles to create optical probes of cell metabolism, and we have elaborated on several fluorescent biosensors as examples. Indeed, the field of metabolic sensor design is still at its infancy. Looking ahead, we anticipate the following challenges and developments: First, many existing fluorescent biosensors could be much improved, as most FRET and cpFP sensors suffer from limited dynamic range or notable pH sensitivity, rendering them difficult to use. Efficient methods to generate and screen for improved variants would be valuable (Zhao et al., 2011a); desirable properties to look for include greater dynamic range, pH resistance, distinct colors for multiplex imaging, or larger lifetime signals for two-photon FLIM in deep tissues. Furthermore, given the vastness of the metabolome, our existing toolbox remains extremely limited and could be further expanded. For sensor design of novel metabolic targets, the focus should be on key molecules that are involved in the regulation of core metabolic pathways, and potential sensor scaffolds may be found amidst the abundance of metabolite-binding protein domains from diverse organisms. In addition to FPs and metabolite-binding protein domains, fluorescent biosensors can also be engineered using RNA aptamers combined with small-molecule fluorophores to image diverse intracellular metabolites (Paige et al., 2011; Paige et al., 2012). Lastly, the current and upcoming probes may help us to elucidate metabolic regulation in diverse areas, such as microbiology, metabolic engineering, cancer metabolism, and neurobiology (Reaves and Rabinowitz, 2010; Gerosa and Sauer, 2011; Lunt and Vander Heiden, 2011; Tantama et al., 2012). While fluorescent sensors cannot monitor the fluxes of metabolic pathways *per se*, their measurements of metabolite levels or metabolic parameters in individual

intact cells provide valuable information to constrain and evaluate computational models of metabolism. In summary, genetically encoded optical probes should open the door to unraveling the elaborate organization and complexity of cell metabolism – and the consequences of such metabolic regulation in health and disease.

The primary goal of this dissertation work is to create novel optical probes of metabolism, as well as to study the regulation of glycolysis in intact, single cells using these sensors. After reviewing the field of sensor design in this Chapter, I describe in Chapter II our work to engineer Peredox, a fluorescent biosensor of the cytosolic NADH-NAD^+ redox state. In Chapter III, using Peredox with other fluorescent reporters, I investigate the dynamic behaviors and relationships between glycolysis and growth factor signaling pathways in single cells. In Chapter IV, I discuss related projects in designing other sensors related to NADH metabolism and in exploring the regulation of the cytosolic NADH-NAD^+ redox state. In Appendices II and III, I describe projects to which I have contributed, the engineering of a fluorescent ATP:ADP ratio sensor Perceval and a red pH biosensor pHRed. Overall, this thesis presents a set of optical tools to assess metabolic dynamics – and to unravel the complex integration of glucose metabolism and signaling pathways at the single cell level.

ACKNOWLEDGMENTS

This work was supported by the US National Institutes of Health (R01 NS055031 to G.Y.), an Albert J. Ryan fellowship and a Stuart H. Q. and Victoria Quan predoctoral fellowship in neurobiology (both to Y.P.H.). We thank members of the Yellen lab for

their comments. We apologize to our colleagues whose work could not be included due to lack of space.

REFERENCES

Akerboom, J., Rivera, J. D. V., Guilbe, M. M. R., Malavé, E. C. A., Hernandez, H. H., Tian, L., Hires, S. A., Marvin, J. S., Looger, L. L. and Schreiter, E. R. (2009). Crystal structures of the GCaMP calcium sensor reveal the mechanism of fluorescence signal change and aid rational design. J Biol Chem *284*, 6455–6464.

Albrecht, S. C., Barata, A. G., Grosshans, J., Teleman, A. A. and Dick, T. P. (2011). In vivo mapping of hydrogen peroxide and oxidized glutathione reveals chemical and regional specificity of redox homeostasis. Cell Metab *14*, 819–829.

Allen, M. D. and Zhang, J. (2006). Subcellular dynamics of protein kinase A activity visualized by FRET-based reporters. Biochem Biophys Res Commun *348*, 716–721.

Anastasiou, D., Poulogiannis, G., Asara, J. M., Boxer, M. B., Jiang, J.-k., Shen, M., Bellinger, G., Sasaki, A. T., Locasale, J. W., Auld, D. S., Thomas, C. J., Vander Heiden, M. G. and Cantley, L. C. (2011). Inhibition of pyruvate kinase M2 by reactive oxygen species contributes to cellular antioxidant responses. Science *334*, 1278–1283.

Arosio, D., Ricci, F., Marchetti, L., Gualdani, R., Albertazzi, L. and Beltram, F. (2010). Simultaneous intracellular chloride and pH measurements using a GFP-based sensor. Nat Methods *7*, 516–518.

Asher, G. and Schibler, U. (2011). Crosstalk between components of circadian and metabolic cycles in mammals. Cell Metab *13*, 125–137.

Atkinson, D. E. (1968). The energy charge of the adenylate pool as a regulatory parameter. Interaction with feedback modifiers. Biochemistry *7*, 4030–4034.

Bailey, E. E., Pfeifer, H. H. and Thiele, E. A. (2005). The use of diet in the treatment of epilepsy. Epilepsy Behav *6*, 4–8.

Baird, G. S., Zacharias, D. A. and Tsien, R. Y. (1999). Circular permutation and receptor insertion within green fluorescent proteins. Proc Natl Acad Sci U S A *96*, 11241–11246.

Balaban, R. S., Nemoto, S. and Finkel, T. (2005). Mitochondria, oxidants, and aging. Cell *120*, 483–495.

Banko, M. R., Allen, J. J., Schaffer, B. E., Wilker, E. W., Tsou, P., White, J. L., Villén, J., Wang, B., Kim, S. R., Sakamoto, K., Gygi, S. P., Cantley, L. C., Yaffe, M. B., Shokat,

K. M. and Brunet, A. (2011). Chemical genetic screen for AMPKÎ±2 substrates uncovers a network of proteins involved in mitosis. Mol Cell *44*, 878–892.

Barros, L. F., Bittner, C. X., Loaiza, A., Ruminot, I., Larenas, V., Moldenhauer, H., Oyarzún, C. and Alvarez, M. (2009). Kinetic validation of 6-NBDG as a probe for the glucose transporter GLUT1 in astrocytes. J Neurochem *109 Suppl 1*, 94–100.

Bass, J. and Takahashi, J. S. (2010). Circadian integration of metabolism and energetics. Science *330*, 1349–1354.

Belousov, V. V., Fradkov, A. F., Lukyanov, K. A., Staroverov, D. B., Shakhbazov, K. S., Terskikh, A. V. and Lukyanov, S. (2006). Genetically encoded fluorescent indicator for intracellular hydrogen peroxide. Nat Methods *3*, 281–286.

Berg, J., Hung, Y. P. and Yellen, G. (2009). A genetically encoded fluorescent reporter of ATP:ADP ratio. Nat Methods *6*, 161–166.

Bittner, C. X., Loaiza, A., Ruminot, I., Larenas, V., Sotelo-Hitschfeld, T., Gutiérrez, R., Córdova, A., Valdebenito, R., Frommer, W. B. and Barros, L. F. (2010). High resolution measurement of the glycolytic rate. Front Neuroenergetics *2*. pii: 26.

Bittner, C. X., Valdebenito, R., Ruminot, I., Loaiza, A., Larenas, V., Sotelo-Hitschfeld, T., Moldenhauer, H., San Martín, A., Gutiérrez, R., Zambrano, M. and Barros, L. F. (2011). Fast and reversible stimulation of astrocytic glycolysis by K^+ and a delayed and persistent effect of glutamate. J Neurosci *31*, 4709–4713.

Borst, J. W., Willemse, M., Slijkhuis, R., van der Krogt, G., Laptenok, S. P., Jalink, K., Wieringa, B. and Fransen, J. A. M. (2010). ATP changes the fluorescence lifetime of cyan fluorescent protein via an interaction with His148. PLoS One *5*, e13862.

Buchakjian, M. R. and Kornbluth, S. (2010). The engine driving the ship: metabolic steering of cell proliferation and death. Nat Rev Mol Cell Biol *11*, 715–727.

Campbell, R. E. (2009). Fluorescent-protein-based biosensors: modulation of energy transfer as a design principle. Anal Chem *81*, 5972–5979.

Carruthers, A. (1990). Facilitated diffusion of glucose. Physiol Rev *70*, 1135–1176.

Chalfie, M., Tu, Y., Euskirchen, G., Ward, W. W. and Prasher, D. C. (1994). Green fluorescent protein as a marker for gene expression. Science *263*, 802–805.

Christofk, H. R., Vander Heiden, M. G., Harris, M. H., Ramanathan, A., Gerszten, R. E., Wei, R., Fleming, M. D., Schreiber, S. L. and Cantley, L. C. (2008). The M2 splice isoform of pyruvate kinase is important for cancer metabolism and tumour growth. Nature *452*, 230–233.

Day, R. N. and Davidson, M. W. (2009). The fluorescent protein palette: tools for cellular imaging. Chem Soc Rev *38*, 2887–2921.

Dooley, C. T., Dore, T. M., Hanson, G. T., Jackson, W. C., Remington, S. J. and Tsien, R. Y. (2004). Imaging dynamic redox changes in mammalian cells with green fluorescent protein indicators. J Biol Chem *279*, 22284–22293.

Fehr, M., Lalonde, S., Lager, I., Wolff, M. W. and Frommer, W. B. (2003). In vivo imaging of the dynamics of glucose uptake in the cytosol of COS-7 cells by fluorescent nanosensors. J Biol Chem *278*, 19127–19133.

Frommer, W. B., Davidson, M. W. and Campbell, R. E. (2009). Genetically encoded biosensors based on engineered fluorescent proteins. Chem Soc Rev *38*, 2833–2841.

Gallegos, L. L., Kunkel, M. T. and Newton, A. C. (2006). Targeting protein kinase C activity reporter to discrete intracellular regions reveals spatiotemporal differences in agonist-dependent signaling. J Biol Chem *281*, 30947–30956.

Gao, P., Tchernyshyov, I., Chang, T.-C., Lee, Y.-S., Kita, K., Ochi, T., Zeller, K. I., De Marzo, A. M., Van Eyk, J. E., Mendell, J. T. and Dang, C. V. (2009). c-Myc suppression of miR-23a/b enhances mitochondrial glutaminase expression and glutamine metabolism. Nature *458*, 762–765.

Gerosa, L. and Sauer, U. (2011). Regulation and control of metabolic fluxes in microbes. Curr Opin Biotechnol *22*, 566–575.

Giepmans, B. N. G., Adams, S. R., Ellisman, M. H. and Tsien, R. Y. (2006). The fluorescent toolbox for assessing protein location and function. Science *312*, 217–224.

Griesbeck, O., Baird, G. S., Campbell, R. E., Zacharias, D. A. and Tsien, R. Y. (2001). Reducing the environmental sensitivity of yellow fluorescent protein. Mechanism and applications. J Biol Chem *276*, 29188–29194.

Gutscher, M., Pauleau, A.-L., Marty, L., Brach, T., Wabnitz, G. H., Samstag, Y., Meyer, A. J. and Dick, T. P. (2008). Real-time imaging of the intracellular glutathione redox potential. Nat Methods *5*, 553–559.

Gutscher, M., Sobotta, M. C., Wabnitz, G. H., Ballikaya, S., Meyer, A. J., Samstag, Y. and Dick, T. P. (2009). Proximity-based protein thiol oxidation by H2O2-scavenging peroxidases. J Biol Chem *284*, 31532–31540.

Guzman, J. N., Sanchez-Padilla, J., Wokosin, D., Kondapalli, J., Ilijic, E., Schumacker, P. T. and Surmeier, D. J. (2010). Oxidant stress evoked by pacemaking in dopaminergic neurons is attenuated by DJ-1. Nature *468*, 696–700.

Haj, F. G., Verveer, P. J., Squire, A., Neel, B. G. and Bastiaens, P. I. H. (2002). Imaging sites of receptor dephosphorylation by PTP1B on the surface of the endoplasmic reticulum. Science *295*, 1708–1711.

Han, J. and Burgess, K. (2010). Fluorescent indicators for intracellular pH. Chem Rev *110*, 2709–2728.

Hanson, G. T., Aggeler, R., Oglesbee, D., Cannon, M., Capaldi, R. A., Tsien, R. Y. and Remington, S. J. (2004). Investigating mitochondrial redox potential with redox-sensitive green fluorescent protein indicators. J Biol Chem *279*, 13044–13053.

Hardie, D. G. (2004). The AMP-activated protein kinase pathway–new players upstream and downstream. J Cell Sci *117*, 5479–5487.

Harman, A. W., Nieminen, A. L., Lemasters, J. J. and Herman, B. (1990). Cytosolic free magnesium, ATP and blebbing during chemical hypoxia in cultured rat hepatocytes. Biochem Biophys Res Commun *170*, 477–483.

Haymond, M. W., Howard, C., Ben-Galim, E. and DeVivo, D. C. (1983). Effects of ketosis on glucose flux in children and adults. Am J Physiol *245*, E373–E378.

Herbst, K. J., Ni, Q. and Zhang, J. (2009). Dynamic visualization of signal transduction in living cells: from second messengers to kinases. IUBMB Life *61*, 902–908.

Hires, S. A., Zhu, Y. and Tsien, R. Y. (2008). Optical measurement of synaptic glutamate spillover and reuptake by linker optimized glutamate-sensitive fluorescent reporters. Proc Natl Acad Sci U S A *105*, 4411–4416.

Hirose, K., Kadowaki, S., Tanabe, M., Takeshima, H. and Iino, M. (1999). Spatiotemporal dynamics of inositol 1,4,5-trisphosphate that underlies complex Ca^{2+} mobilization patterns. Science *284*, 1527–1530.

Hirrlinger, P. G., Scheller, A., Braun, C., Quintela-Schneider, M., Fuss, B., Hirrlinger, J. and Kirchhoff, F. (2005). Expression of reef coral fluorescent proteins in the central nervous system of transgenic mice. Mol Cell Neurosci *30*, 291–303.

Hou, B.-H., Takanaga, H., Grossmann, G., Chen, L.-Q., Qu, X.-Q., Jones, A. M., Lalonde, S., Schweissgut, O., Wiechert, W. and Frommer, W. B. (2011). Optical sensors for monitoring dynamic changes of intracellular metabolite levels in mammalian cells. Nat Protoc *6*, 1818–1833.

Hung, Y. P., Albeck, J. G., Tantama, M. and Yellen, G. (2011). Imaging cytosolic NADH-NAD^+ redox state with a genetically encoded fluorescent biosensor. Cell Metab *14*, 545–554.

Imamura, H., Nhat, K. P. H., Togawa, H., Saito, K., Iino, R., Kato-Yamada, Y., Nagai, T. and Noji, H. (2009). Visualization of ATP levels inside single living cells with fluorescence resonance energy transfer-based genetically encoded indicators. Proc Natl Acad Sci U S A *106*, 15651–15656.

Jayaraman, S., Haggie, P., Wachter, R. M., Remington, S. J. and Verkman, A. S. (2000). Mechanism and cellular applications of a green fluorescent protein-based halide sensor. J Biol Chem *275*, 6047–6050.

Jouaville, L. S., Pinton, P., Bastianutto, C., Rutter, G. A. and Rizzuto, R. (1999). Regulation of mitochondrial ATP synthesis by calcium: evidence for a long-term metabolic priming. Proc Natl Acad Sci U S A *96*, 13807–13812.

Jung, D. W., Apel, L. and Brierley, G. P. (1990). Matrix free Mg^{2+} changes with metabolic state in isolated heart mitochondria. Biochemistry *29*, 4121–4128.

Katayama, H., Yamamoto, A., Mizushima, N., Yoshimori, T. and Miyawaki, A. (2008). GFP-like proteins stably accumulate in lysosomes. Cell Struct Funct *33*, 1–12.

Kennedy, H. J., Pouli, A. E., Ainscow, E. K., Jouaville, L. S., Rizzuto, R. and Rutter, G. A. (1999). Glucose generates sub-plasma membrane ATP microdomains in single islet beta-cells. Potential role for strategically located mitochondria. J Biol Chem *274*, 13281–13291.

Kirber, M. T., Chen, K. and Keaney, Jr, J. F. (2007). YFP photoconversion revisited: confirmation of the CFP-like species. Nat Methods *4*, 767–768.

Klingenberg, M. and Bücher, T. (1960). Biological oxidations. Annu Rev Biochem *29*, 669–708.

Komatsu, N., Aoki, K., Yamada, M., Yukinaga, H., Fujita, Y., Kamioka, Y. and Matsuda, M. (2011). Development of an optimized backbone of FRET biosensors for kinases and GTPases. Mol Biol Cell *22*, 4647–4656.

Krebs, H. A. (1977). Regulatory mechanisms in purine biosynthesis. Adv Enzyme Regul *16*, 409–422.

Kremers, G.-J., Hazelwood, K. L., Murphy, C. S., Davidson, M. W. and Piston, D. W. (2009). Photoconversion in orange and red fluorescent proteins. Nat Methods *6*, 355–358.

Lakowicz, J. R. (2006). Principles of Fluorescence Spectroscopy. 3rd edition, Springer.

Lee, S.-J. R., Escobedo-Lozoya, Y., Szatmari, E. M. and Yasuda, R. (2009). Activation of CaMKII in single dendritic spines during long-term potentiation. Nature *458*, 299–304.

Lemke, E. A. and Schultz, C. (2011). Principles for designing fluorescent sensors and reporters. Nat Chem Biol *7*, 480–483.

Llopis, J., McCaffery, J. M., Miyawaki, A., Farquhar, M. G. and Tsien, R. Y. (1998). Measurement of cytosolic, mitochondrial, and Golgi pH in single living cells with green fluorescent proteins. Proc Natl Acad Sci U S A *95*, 6803–6808.

Loaiza, A., Porras, O. H. and Barros, L. F. (2003). Glutamate triggers rapid glucose transport stimulation in astrocytes as evidenced by real-time confocal microscopy. J Neurosci *23*, 7337–7342.

Locasale, J. W., Grassian, A. R., Melman, T., Lyssiotis, C. A., Mattaini, K. R., Bass, A. J., Heffron, G., Metallo, C. M., Muranen, T., Sharfi, H., Sasaki, A. T., Anastasiou, D., Mullarky, E., Vokes, N. I., Sasaki, M., Beroukhim, R., Stephanopoulos, G., Ligon, A. H., Meyerson, M., Richardson, A. L., Chin, L., Wagner, G., Asara, J. M., Brugge, J. S., Cantley, L. C. and Vander Heiden, M. G. (2011). Phosphoglycerate dehydrogenase diverts glycolytic flux and contributes to oncogenesis. Nat Genet *43*, 869–874.

Lowry, O. H. and Passonneau, J. V. (1964). The relationships between substrates and enzymes of glycolysis in brain. J Biol Chem *239*, 31–42.

Lunt, S. Y. and Vander Heiden, M. G. (2011). Aerobic glycolysis: meeting the metabolic requirements of cell proliferation. Annu Rev Cell Dev Biol *27*, 441–464.

Merksamer, P. I., Trusina, A. and Papa, F. R. (2008). Real-time redox measurements during endoplasmic reticulum stress reveal interlinked protein folding functions. Cell *135*, 933–947.

Meyer, A. J. and Dick, T. P. (2010). Fluorescent protein-based redox probes. Antioxid Redox Signal *13*, 621–650.

Miesenböck, G., De Angelis, D. A. and Rothman, J. E. (1998). Visualizing secretion and synaptic transmission with pH-sensitive green fluorescent proteins. Nature *394*, 192–195.

Mihaylova, M. M. and Shaw, R. J. (2011). The AMPK signalling pathway coordinates cell growth, autophagy and metabolism. Nat Cell Biol *13*, 1016–1023.

Mishina, N., Bogeski, I., Bolotin, D. A., Hoth, M., Niemeyer, B. A., Schultz, C., Zagaynova, E. V., Lukyanov, S. and Belousov, V. (2012). Can we see PIP3 and hydrogen peroxide with a single probe? Antioxid Redox Signal .

Miyawaki, A. (2011). Development of probes for cellular functions using fluorescent proteins and fluorescence resonance energy transfer. Annu Rev Biochem *80*, 357–373.

Miyawaki, A., Llopis, J., Heim, R., McCaffery, J. M., Adams, J. A., Ikura, M. and Tsien, R. Y. (1997). Fluorescent indicators for Ca^{2+} based on green fluorescent proteins and calmodulin. Nature *388*, 882–887.

Mörikofer-Zwez, S. and Walter, P. (1989). Binding of ADP to rat liver cytosolic proteins and its influence on the ratio of free ATP/free ADP. Biochem J *259*, 117–124.

Murphy, M. P., Holmgren, A., Larsson, N.-G., Halliwell, B., Chang, C. J., Kalyanaraman, B., Rhee, S. G., Thornalley, P. J., Partridge, L., Gems, D., Nyström, T., Belousov, V., Schumacker, P. T. and Winterbourn, C. C. (2011). Unraveling the biological roles of reactive oxygen species. Cell Metab *13*, 361–366.

Nagai, T., Ibata, K., Park, E. S., Kubota, M., Mikoshiba, K. and Miyawaki, A. (2002). A variant of yellow fluorescent protein with fast and efficient maturation for cell-biological applications. Nat Biotechnol *20*, 87–90.

Nagai, T., Sawano, A., Park, E. S. and Miyawaki, A. (2001). Circularly permuted green fluorescent proteins engineered to sense Ca^{2+}. Proc Natl Acad Sci U S A *98*, 3197–3202.

Nagai, T., Yamada, S., Tominaga, T., Ichikawa, M. and Miyawaki, A. (2004). Expanded dynamic range of fluorescent indicators for Ca^{2+} by circularly permuted yellow fluorescent proteins. Proc Natl Acad Sci U S A *101*, 10554–10559.

Nakano, M., Imamura, H., Nagai, T. and Noji, H. (2011). Ca^{2+} regulation of mitochondrial ATP synthesis visualized at the single cell level. ACS Chem Biol *6*, 709–715.

Nausch, L. W. M., Ledoux, J., Bonev, A. D., Nelson, M. T. and Dostmann, W. R. (2008). Differential patterning of cGMP in vascular smooth muscle cells revealed by single GFP-linked biosensors. Proc Natl Acad Sci U S A *105*, 365–370.

Nicholls, D. G. and Ferguson, S. J. (2002). Bioenergetics, Third Edition. 3 edition, Academic Press.

Niswender, K. D., Blackman, S. M., Rohde, L., Magnuson, M. A. and Piston, D. W. (1995). Quantitative imaging of green fluorescent protein in cultured cells: comparison of microscopic techniques, use in fusion proteins and detection limits. J Microsc *180*, 109–116.

Oancea, E. and Meyer, T. (1998). Protein kinase C as a molecular machine for decoding calcium and diacylglycerol signals. Cell *95*, 307–318.

Oancea, E., Teruel, M. N., Quest, A. F. and Meyer, T. (1998). Green fluorescent protein (GFP)-tagged cysteine-rich domains from protein kinase C as fluorescent indicators for diacylglycerol signaling in living cells. J Cell Biol *140*, 485–498.

Ogikubo, S., Nakabayashi, T., Adachi, T., Islam, M. S., Yoshizawa, T., Kinjo, M. and Ohta, N. (2011). Intracellular pH sensing using autofluorescence lifetime microscopy. J Phys Chem B *115*, 10385–10390.

Ormö, M., Cubitt, A. B., Kallio, K., Gross, L. A., Tsien, R. Y. and Remington, S. J. (1996). Crystal structure of the *Aequorea victoria* green fluorescent protein. Science *273*, 1392–1395.

Ostergaard, H., Henriksen, A., Hansen, F. G. and Winther, J. R. (2001). Shedding light on disulfide bond formation: engineering a redox switch in green fluorescent protein. EMBO J *20*, 5853–5862.

Owen, O. E., Morgan, A. P., Kemp, H. G., Sullivan, J. M., Herrera, M. G. and Cahill, Jr, G. (1967). Brain metabolism during fasting. J Clin Invest *46*, 1589–1595.

Paige, J. S., Wu, K. Y. and Jaffrey, S. R. (2011). RNA mimics of green fluorescent protein. Science *333*, 642–646.

Paige, J. S., Nguyen-Duc, T., Song, W. and Jaffrey, S. R. (2012). Fluorescence imaging of cellular metabolites with RNA. Science *335*, 1194.

Palmer, A. E., Qin, Y., Park, J. G. and McCombs, J. E. (2011). Design and application of genetically encoded biosensors. Trends Biotechnol *29*, 144–152.

Patterson, G. H., Knobel, S. M., Arkhammar, P., Thastrup, O. and Piston, D. W. (2000). Separation of the glucose-stimulated cytoplasmic and mitochondrial NAD(P)H responses in pancreatic islet beta cells. Proc Natl Acad Sci U S A *97*, 5203–5207.

Poburko, D., Santo-Domingo, J. and Demaurex, N. (2011). Dynamic regulation of the mitochondrial proton gradient during cytosolic calcium elevations. J Biol Chem *286*, 11672–11684.

Possemato, R., Marks, K. M., Shaul, Y. D., Pacold, M. E., Kim, D., Birsoy, K., Sethumadhavan, S., Woo, H.-K., Jang, H. G., Jha, A. K., Chen, W. W., Barrett, F. G., Stransky, N., Tsun, Z.-Y., Cowley, G. S., Barretina, J., Kalaany, N. Y., Hsu, P. P., Ottina, K., Chan, A. M., Yuan, B., Garraway, L. A., Root, D. E., Mino-Kenudson, M., Brachtel, E. F., Driggers, E. M. and Sabatini, D. M. (2011). Functional genomics reveal that the serine synthesis pathway is essential in breast cancer. Nature *476*, 346–350.

Pradet, A. and Raymond, P. (1983). Adenine nucleotide ratios and adenylate energy charge in energy metabolism. Annual Review of Plant Physiology *34*, 199–224.

Raucher, D., Stauffer, T., Chen, W., Shen, K., Guo, S., York, J. D., Sheetz, M. P. and Meyer, T. (2000). Phosphatidylinositol 4,5-bisphosphate functions as a second messenger that regulates cytoskeleton-plasma membrane adhesion. Cell *100*, 221–228.

Reaves, M. L. and Rabinowitz, J. D. (2011). Metabolomics in systems microbiology. Curr Opin Biotechnol *22*, 17–25.

Reznick, R. M. and Shulman, G. I. (2006). The role of AMP-activated protein kinase in mitochondrial biogenesis. J Physiol *574*, 33–39.

Rocheleau, J. V., Head, W. S. and Piston, D. W. (2004). Quantitative NAD(P)H/flavoprotein autofluorescence imaging reveals metabolic mechanisms of pancreatic islet pyruvate response. J Biol Chem *279*, 31780–31787.

Romoser, V. A., Hinkle, P. M. and Persechini, A. (1997). Detection in living cells of Ca^{2+}-dependent changes in the fluorescence emission of an indicator composed of two green fluorescent protein variants linked by a calmodulin-binding sequence. A new class of fluorescent indicators. J Biol Chem *272*, 13270–13274.

Sarbassov, D. D., Ali, S. M. and Sabatini, D. M. (2005). Growing roles for the mTOR pathway. Curr Opin Cell Biol *17*, 596–603.

Sato, M., Nakajima, T., Goto, M. and Umezawa, Y. (2006). Cell-based indicator to visualize picomolar dynamics of nitric oxide release from living cells. Anal Chem *78*, 8175–8182.

Schoolwerth, A. C. and LaNoue, K. F. (1985). Transport of metabolic substrates in renal mitochondria. Annu Rev Physiol *47*, 143–171.

Shaner, N. C., Campbell, R. E., Steinbach, P. A., Giepmans, B. N. G., Palmer, A. E. and Tsien, R. Y. (2004). Improved monomeric red, orange and yellow fluorescent proteins derived from Discosoma sp. red fluorescent protein. Nat Biotechnol *22*, 1567–1572.

Shaner, N. C., Steinbach, P. A. and Tsien, R. Y. (2005). A guide to choosing fluorescent proteins. Nat Methods *2*, 905–909.

Shaw, R. J. and Cantley, L. C. (2006). Ras, PI(3)K and mTOR signalling controls tumour cell growth. Nature *441*, 424–430.

Shimomura, O., Johnson, F. H. and Saiga, Y. (1962). Extraction, purification and properties of aequorin, a bioluminescent protein from the luminous hydromedusan, *Aequorea*. J Cell Comp Physiol *59*, 223–239.

Shimozono, S., Fukano, T., Kimura, K. D., Mori, I., Kirino, Y. and Miyawaki, A. (2004). Slow Ca^{2+} dynamics in pharyngeal muscles in *Caenorhabditis elegans* during fast pumping. EMBO Rep *5*, 521–526.

Sokoloff, L., Reivich, M., Kennedy, C., Des Rosiers, M. H., Patlak, C. S., Pettigrew, K. D., Sakurada, O. and Shinohara, M. (1977). The [14C]deoxyglucose method for the measurement of local cerebral glucose utilization: theory, procedure, and normal values in the conscious and anesthetized albino rat. J Neurochem *28*, 897–916.

Souslova, E. A., Belousov, V. V., Lock, J. G., Strömblad, S., Kasparov, S., Bolshakov, A. P., Pinelis, V. G., Labas, Y. A., Lukyanov, S., Mayr, L. M. and Chudakov, D. M. (2007). Single fluorescent protein-based Ca^{2+} sensors with increased dynamic range. BMC Biotechnol *7*, 37.

Stauffer, T. P., Ahn, S. and Meyer, T. (1998). Receptor-induced transient reduction in plasma membrane PtdIns(4,5)P2 concentration monitored in living cells. Curr Biol *8*, 343–346.

Takanaga, H., Chaudhuri, B. and Frommer, W. B. (2008). GLUT1 and GLUT9 as major contributors to glucose influx in HepG2 cells identified by a high sensitivity intramolecular FRET glucose sensor. Biochim Biophys Acta *1778*, 1091–1099.

Tantama, M., Hung, Y. P. and Yellen, G. (2011). Imaging intracellular pH in live cells with a genetically encoded red fluorescent protein sensor. J Am Chem Soc *133*, 10034–10037.

Tantama, M., Hung, Y. P. and Yellen, G. (2012). Optogenetic reporters: Fluorescent protein-based genetically encoded indicators of signaling and metabolism in the brain. Prog Brain Res *196*, 235–263.

Tsien, R. Y. (1998). The green fluorescent protein. Annu Rev Biochem *67*, 509–544.

Tsou, P., Zheng, B., Hsu, C.-H., Sasaki, A. T. and Cantley, L. C. (2011). A fluorescent reporter of AMPK activity and cellular energy stress. Cell Metab *13*, 476–486.

Valentin, G., Verheggen, C., Piolot, T., Neel, H., Coppey-Moisan, M. and Bertrand, E. (2005). Photoconversion of YFP into a CFP-like species during acceptor photobleaching FRET experiments. Nat Methods *2*, 801.

Vander Heiden, M. G., Cantley, L. C. and Thompson, C. B. (2009). Understanding the Warburg effect: the metabolic requirements of cell proliferation. Science *324*, 1029–1033.

Vaughn, A. E. and Deshmukh, M. (2008). Glucose metabolism inhibits apoptosis in neurons and cancer cells by redox inactivation of cytochrome c. Nat Cell Biol *10*, 1477–1483.

Vining, E. P. (1999). Clinical efficacy of the ketogenic diet. Epilepsy Res *37*, 181–190.

Vinkenborg, J. L., Koay, M. S. and Merkx, M. (2010). Fluorescent imaging of transition metal homeostasis using genetically encoded sensors. Curr Opin Chem Biol *14*, 231–237.

Vousden, K. H. and Ryan, K. M. (2009). p53 and metabolism. Nat Rev Cancer *9*, 691–700.

Wagnières, G. A., Star, W. M. and Wilson, B. C. (1998). In vivo fluorescence spectroscopy and imaging for oncological applications. Photochem Photobiol *68*, 603–632.

Wang, W., Fang, H., Groom, L., Cheng, A., Zhang, W., Liu, J., Wang, X., Li, K., Han, P., Zheng, M., Yin, J., Wang, W., Mattson, M. P., Kao, J. P. Y., Lakatta, E. G., Sheu, S.-S., Ouyang, K., Chen, J., Dirksen, R. T. and Cheng, H. (2008). Superoxide flashes in single mitochondria. Cell *134*, 279–290.

Warburg, O. (1956). On the origin of cancer cells. Science *123*, 309–314.

Warburg, O., Wind, F. and Negelein, E. (1927). The metabolism of tumors in the body. J Gen Physiol *8*, 519–530.

Wardman, P. (2007). Fluorescent and luminescent probes for measurement of oxidative and nitrosative species in cells and tissues: progress, pitfalls, and prospects. Free Radic Biol Med *43*, 995–1022.

Wellen, K. E., Hatzivassiliou, G., Sachdeva, U. M., Bui, T. V., Cross, J. R. and Thompson, C. B. (2009). ATP-citrate lyase links cellular metabolism to histone acetylation. Science *324*, 1076–1080.

Wellen, K. E., Lu, C., Mancuso, A., Lemons, J. M. S., Ryczko, M., Dennis, J. W., Rabinowitz, J. D., Coller, H. A. and Thompson, C. B. (2010). The hexosamine biosynthetic pathway couples growth factor-induced glutamine uptake to glucose metabolism. Genes Dev *24*, 2784–2799.

Willemse, M., Janssen, E., de Lange, F., Wieringa, B. and Fransen, J. (2007). ATP and FRET–a cautionary note. Nat Biotechnol *25*, 170–172.

Williamson, D. H., Lund, P. and Krebs, H. A. (1967). The redox state of free nicotinamide-adenine dinucleotide in the cytoplasm and mitochondria of rat liver. Biochem J *103*, 514–527.

Winterbourn, C. C. (2008). Reconciling the chemistry and biology of reactive oxygen species. Nat Chem Biol *4*, 278–286.

Yamada, K., Nakata, M., Horimoto, N., Saito, M., Matsuoka, H. and Inagaki, N. (2000). Measurement of glucose uptake and intracellular calcium concentration in single, living pancreatic beta-cells. J Biol Chem *275*, 22278–22283.

Yamada, K., Saito, M., Matsuoka, H. and Inagaki, N. (2007). A real-time method of imaging glucose uptake in single, living mammalian cells. Nat Protoc *2*, 753–762.

Yang, F., Moss, L. G. and Phillips, Jr, G. (1996). The molecular structure of green fluorescent protein. Nat Biotechnol *14*, 1246–1251.

Yanushevich, Y. G., Staroverov, D. B., Savitsky, A. P., Fradkov, A. F., Gurskaya, N. G., Bulina, M. E., Lukyanov, K. A. and Lukyanov, S. A. (2002). A strategy for the generation of non-aggregating mutants of Anthozoa fluorescent proteins. FEBS Lett *511*, 11–14.

Yellen, G. (2008). Ketone bodies, glycolysis, and KATP channels in the mechanism of the ketogenic diet. Epilepsia *49 Suppl 8*, 80–82.

Yeung, T., Gilbert, G. E., Shi, J., Silvius, J., Kapus, A. and Grinstein, S. (2008). Membrane phosphatidylserine regulates surface charge and protein localization. Science *319*, 210–213.

Yi, C. H., Pan, H., Seebacher, J., Jang, I.-H., Hyberts, S. G., Heffron, G. J., Vander Heiden, M. G., Yang, R., Li, F., Locasale, J. W., Sharfi, H., Zhai, B., Rodriguez-Mias, R., Luithardt, H., Cantley, L. C., Daley, G. Q., Asara, J. M., Gygi, S. P., Wagner, G., Liu, C.-F. and Yuan, J. (2011). Metabolic regulation of protein N-alpha-acetylation by Bcl-xL promotes cell survival. Cell *146*, 607–620.

Yoshioka, K., Takahashi, H., Homma, T., Saito, M., Oh, K. B., Nemoto, Y. and Matsuoka, H. (1996). A novel fluorescent derivative of glucose applicable to the assessment of glucose uptake activity of Escherichia coli. Biochim Biophys Acta *1289*, 5–9.

Yuneva, M. O., Fan, T. W. M., Allen, T. D., Higashi, R. M., Ferraris, D. V., Tsukamoto, T., Matés, J. M., Alonso, F. J., Wang, C., Seo, Y., Chen, X. and Bishop, J. M. (2012). The metabolic profile of tumors depends on both the responsible genetic lesion and tissue type. Cell Metab *15*, 157–170.

Zapata-Hommer, O. and Griesbeck, O. (2003). Efficiently folding and circularly permuted variants of the Sapphire mutant of GFP. BMC Biotechnol *3*, 5.

Zhang, J., Campbell, R. E., Ting, A. Y. and Tsien, R. Y. (2002a). Creating new fluorescent probes for cell biology. Nat Rev Mol Cell Biol *3*, 906–918.

Zhang, Q., Piston, D. W. and Goodman, R. H. (2002b). Regulation of corepressor function by nuclear NADH. Science *295*, 1895–1897.

Zhao, Y., Araki, S., Wu, J., Teramoto, T., Chang, Y.-F., Nakano, M., Abdelfattah, A. S., Fujiwara, M., Ishihara, T., Nagai, T. and Campbell, R. E. (2011a). An expanded palette of genetically encoded Ca^{2+} indicators. Science *333*, 1888–1891.

Zhao, Y., Jin, J., Hu, Q., Zhou, H.-M., Yi, J., Yu, Z., Xu, L., Wang, X., Yang, Y. and Loscalzo, J. (2011b). Genetically encoded fluorescent sensors for intracellular NADH detection. Cell Metab *14*, 555–566.

Zheng, L., Roeder, R. G. and Luo, Y. (2003). S phase activation of the histone H2B promoter by OCA-S, a coactivator complex that contains GAPDH as a key component. Cell *114*, 255–266.

Chapter II

Imaging cytosolic NADH-NAD^+ redox state with a genetically encoded fluorescent biosensor

Yin Pun Hung [1], John G. Albeck [2], Mathew Tantama [1], and Gary Yellen [1]

[1] Department of Neurobiology and [2] Department of Cell Biology, Harvard Medical School, 220 Longwood Avenue, Boston, Massachusetts 02115, USA

Reproduced from Hung YP, Albeck JG, Tantama M, Yellen G. (2011). Imaging cytosolic NADH-NAD^+ redox state with a genetically encoded fluorescent biosensor. *Cell Metabolism*. 14(4):545-554.

Yin Pun Hung contributed all figures in this chapter, with help from Mathew Tantama on Figure 2.3A and collaboration with John G. Albeck on Figure 2.6.

ABSTRACT

NADH is a key metabolic cofactor whose sensitive and specific detection in the cytosol of live cells has been difficult. We constructed a fluorescent biosensor of the cytosolic NADH-NAD^+ redox state by combining a circularly permuted GFP T-Sapphire with a bacterial NADH-binding protein Rex. Although the initial construct reported [NADH] × [H^+] / [NAD^+], its pH sensitivity was eliminated by mutagenesis. The engineered biosensor, Peredox, reports cytosolic NADH:NAD^+ ratios and can be calibrated with exogenous lactate and pyruvate. We demonstrated its utility in several cultured and primary cell types. We found glycolysis opposed the lactate dehydrogenase equilibrium to produce a reduced cytosolic NADH-NAD^+ redox state. We also observed different redox states in primary mouse astrocytes and neurons, consistent with hypothesized metabolic differences. Furthermore, using high-content image analysis, we monitored NADH responses to PI3K pathway inhibition in hundreds of live cells. As an NADH reporter, Peredox should enable better understanding of bioenergetics.

INTRODUCTION

Nicotinamide adenine dinucleotide (reduced: NADH or oxidized: NAD^+) is a key cofactor for electron transfer in metabolism. Reduction-oxidation (redox) reactions catalyzed by various NAD(H)-dependent dehydrogenases are vital for biochemical processes such as glycolysis and mitochondrial metabolism. In addition, NADH-NAD^+ redox has been implicated in the regulation of embryonic development and aging (Dumollard et al., 2007; Chen et al., 2009), as well as in pathological conditions such as diabetes, cancer, and epilepsy (Eto et al., 1999; Zhang et al., 2006; Garriga-Canut et al., 2006).

To assess the cellular NADH-NAD^+ redox state, there have been two general approaches. Chemical methods infer the NADH:NAD^+ ratio indirectly from the concentrations of redox couples such as lactate and pyruvate (Williamson et al., 1967). However, this requires the use of cell extracts and is thus incompatible with studying dynamics in intact, individual cells. A less invasive optical approach monitors cellular NAD(P)H autofluorescence. Under ultraviolet excitation, NADH and another related cofactor NADPH are fluorescent, whereas their oxidized counterparts NAD^+ and $NADP^+$ are not (Chance et al., 1962). As NADH and NADPH give identical autofluorescence signals, they are collectively denoted as NAD(P)H, although the two cofactors govern distinct metabolic reactions (Klingenberg and Bücher, 1960). Since NADH is present at higher levels than NADPH in many tissues, the NAD(P)H signal has often been interpreted as changes in NADH (Lowry et al., 1957; Klingenberg and Bücher, 1960; Chance et al., 1962). However, data from simultaneous imaging of both NAD(P)H and flavoprotein autofluorescence underscore the ambiguity of the NAD(P)H signal,

suggesting that the NAD(P)H signal may primarily report protein-bound NADPH instead of NADH (Rocheleau et al., 2004). In addition to the signal ambiguity, in general, cytosolic and mitochondrial NAD(P)H autofluorescence have been assumed to reflect glycolysis and oxidative metabolism, respectively (Patterson et al., 2000; Shuttleworth et al., 2003; Kasischke et al., 2004; Gordon et al., 2008). In practice, mitochondrial signals dominate the measurements, whereas cytosolic signals are small and difficult to separate from the bright mitochondrial signals. For more specific and sensitive detection of the cytosolic NADH-NAD^+ redox state, a fluorescent NADH biosensor would be valuable.

One strategy to create genetically encoded fluorescent biosensors involves circularly permuted fluorescent proteins (cpFPs), derived from green fluorescent proteins (GFPs). Circular permutation joins the original N and C termini with a peptide linker and creates new termini near the chromophore (Baird et al., 1999). A specific detector or binding protein fused to the new N and C termini creates conformational coupling between binding and fluorescence. With this strategy, fluorescent biosensors have been engineered to report calcium, hydrogen peroxide, cyclic 3′,5′-guanosine monophosphate (cGMP), and ATP:ADP ratio (Nagai et al., 2001; Belousov et al., 2006; Nausch et al., 2008; Berg et al., 2009). For a detector domain, we chose the redox sensing repressor Rex, a bacterial NADH-binding protein that links metabolic state to gene expression (Brekasis and Paget, 2003). Rex is a homodimer; each subunit comprises an N-terminal domain and a C-terminal NADH-binding domain (Sickmier et al., 2005). Upon NADH binding, Rex adopts a closed instead of an open conformation (Sickmier et al., 2005; Wang et al., 2008; McLaughlin et al., 2010). Here, we found that integration of a cpFP T-Sapphire into Rex yielded a fluorescent sensor of NADH. The initial construct (and likely

the native Rex protein) reported [NADH] × [H^+] / [NAD^+]. By eliminating its pH dependence via targeted mutagenesis, we constructed a genetically encoded fluorescent biosensor of cytosolic NADH:NAD^+ ratios. This reporter, Peredox, revealed cytosolic NADH-NAD^+ redox dynamics in mammalian cells upon metabolic challenges. With transient or stable expression, we demonstrated the utility of Peredox in a variety of primary and cultured cell types. We found different cytosolic NADH-NAD^+ redox states in primary mouse cortical astrocytes versus neurons, as well as changes in cytosolic NADH-NAD^+ redox in cultured epithelial cells upon perturbation of PI3K pathway signaling.

RESULTS

A cpFP inserted into T-Rex reports [NADH] × [H^+] / [NAD^+]

To engineer an NADH biosensor, we inserted a cpFP variant of T-Sapphire (Zapata-Hommer and Griesbeck, 2003) into a tandem dimer of Rex from *Thermus aquaticus* (T-Rex), between the two subunits. By PCR we created a library of peptide linkers for the cpFP insertion, expressed the protein library in bacteria, and assayed the purified proteins for fluorescence responses. We found that a cpFP inserted into T-Rex could couple conformational changes with fluorescence to report NADH (Figure 2.1A). A construct, named P0, exhibited an increase in green fluorescence upon NADH application (Figure 2.1B). Its spectra were similar to that of T-Sapphire, with an excitation peak around 400 nm and an emission peak around 510 nm. While NADH application enhanced the green fluorescence, it did not change the red fluorescence of a

tandemly attached mCherry (Shaner et al., 2004), which was included to normalize the signal for protein expression. The affinity of P0 for NADH was less than 5 nM (Appendix I), which was surprising given that the estimated concentration of free NADH in the cytosol is in the hundreds of nanomolar (Zhang et al., 2002). In addition to NADH, NAD^+ can bind to Rex. Unlike NADH, application of NAD^+ yielded only minimal change in fluorescence (Figure 2.1B). However, increasing NAD^+ concentration effectively lowered the sensor's apparent affinity for NADH (Figure 2.1C), indicating that NAD^+ competes with NADH for binding. According to this competitive scheme, when the concentrations of NADH and NAD^+ exceed their affinity constants, the sensor's steady state fluorescence response would report the NADH:NAD^+ ratio (Figure 2.1D; Berg et al., 2009). Although conventionally the ratio R = [NAD^+] / [NADH] is reported, we plotted the response against the alternative ratio R' = [NADH] / [NAD^+] × 1000. The R' at which the response is half maximal is called the '$K_{R'}$' of the sensor, analogous to the dissociation constant (K_d) of a receptor. At pH 7.2, P0 had ~8000-fold higher affinity for NADH than for NAD^+; its half maximal response corresponded to a $K_{R'}$ of 0.12. Because P0 was constructed with a pH resistant GFP T-Sapphire, its fluorescence in the unoccupied state or in the NADH-bound state was pH resistant as expected. Nevertheless, the ability of NAD^+ to compete with NADH for binding did vary substantially with pH (Figure 2.1D). With higher pH, competition by NAD^+ became stronger, further lowering the sensor's apparent affinity for NADH and increasing $K_{R'}$. Remarkably, this pH dependence could be described as a strict dependence of the sensor on [NADH] × [H^+] / [NAD^+] (Figure 2.1E). Indeed, this expression is a component of the equilibrium constant of any NAD(H)-dependent dehydrogenase, and it is proportional to the ratio of the redox

couple. For instance, when the lactate dehydrogenase (LDH) reaction is at equilibrium, the lactate:pyruvate ratio is proportional to [NADH] × [H^+] / [NAD^+].

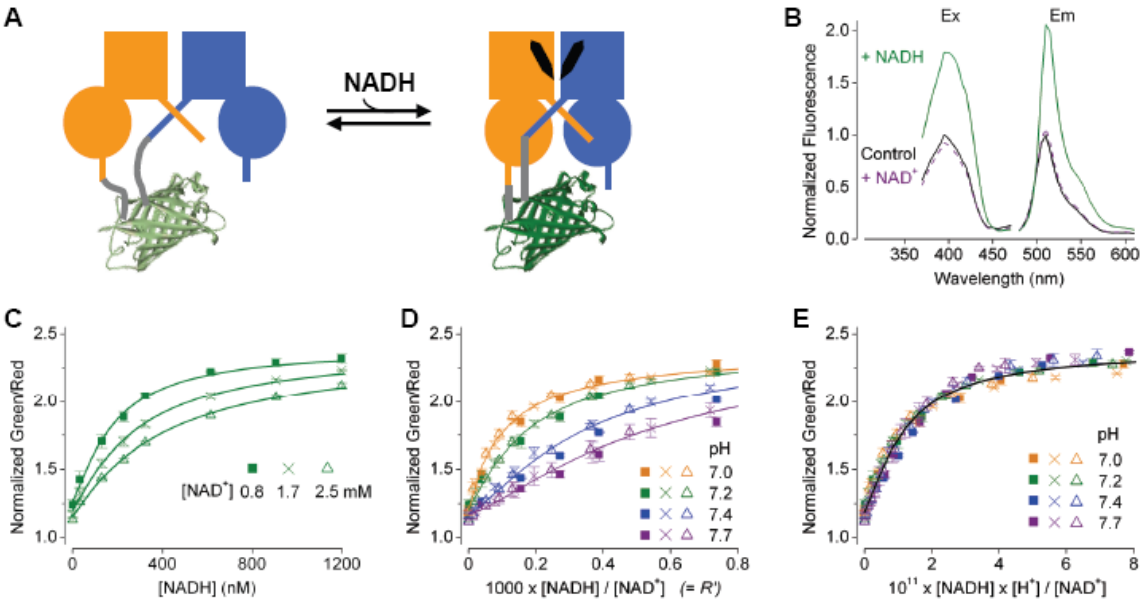

Figure 2.1. Characterization of purified P0, a Rex-cpFP chimera

(A) Schematic showing the sensor design, with a cpFP (PDB: 3evp) interposed between the two T-Rex subunits (blue and orange), and a change of fluorescence upon binding of NADH (black). (B) Excitation and emission spectra in the control condition (solid black), after addition of 100 µM NAD^+ (dash purple), or 100 µM NAD^+ and 0.2 µM NADH (solid green), normalized to the peak intensity in the control condition. For excitation spectra, emission was measured at 510 ± 5 nm; for emission spectra, excitation was at 400 ± 2.5 nm. (C) Green to red fluorescence ratios at the indicated [NAD^+] at pH 7.2 plotted against [NADH]. (D) Fluorescence ratios at the indicated [NAD^+] and pH plotted against *R′*. (E) Fluorescence ratios at the indicated [NAD^+] and pH plotted against [NADH] × [H^+] / [NAD^+]. Fluorescence ratios (mean ± SEM, n = 3) were normalized to the control condition in the absence of pyridine nucleotides at pH 7.2 at 25°C.

Optimization eliminates the pH sensitivity of the NADH biosensor

Many factors other than metabolism perturb cellular pH. Although P0 reports the interesting quantity [NADH] × [H^+] / [NAD^+], its pH sensitivity renders the signal non-specific to cytosolic NADH-NAD^+ redox and thus not highly useful. Nonetheless, this

quantity [NADH] × [H^+] / [NAD^+] suggests that, similar to NADH-binding dehydrogenases, there is a single proton or charge transfer for each NAD^+ (or NADH) binding event. We reasoned that the highly conserved residue Tyr98, located near the nicotinamide moiety of the NADH molecule in the T-Rex structure (Sickmier et al., 2005), might participate in the proton transfer upon NAD^+ binding (Jörnvall et al., 1995). We then made a protein library with various mutations on Tyr98. In addition, to speed up kinetics (see below), we performed error-prone PCR mutagenesis and screened for improved sensor variants. The best product of the screen contained the mutations Tyr98Trp and Phe189Ile in the first subunit and Tyr98Trp in the second subunit.

This circularly permuted GFP based sensor of NADH-NAD^+ redox, named Peredox, demonstrated notable improvements in pH resistance and kinetics for cytosolic NADH-NAD^+ redox sensing. While Peredox retained the spectral properties of the original P0 construct, it was far more resistant to pH changes in the physiological range (Figure 2.2A). For an increase of one pH unit, which produced a 10-fold increase of $K_{R'}$ in P0 (Figure 2.1D), the $K_{R'}$ of Peredox changed only slightly by ~20%, with a crossover point (signal insensitive to pH) at $R' \approx 3$ (Figure 2.2A). Upon NADH saturation, Peredox displayed an increase of ~150% in fluorescence response (i.e. a 2.5-fold increase). Due to its lower affinities for NAD^+ and NADH, Peredox reported the cytosolic NADH level, partly compensated for the NAD^+ level, rather than strictly the NADH:NAD^+ ratio. The NADH:NAD^+ ratio required for a half maximal response was somewhat resistant to changes in the overall [NADH + NAD^+]: a 3-fold change in the NAD^+ pool size in the physiological range produced a ~2-fold change in the sensor midpoint for NADH:NAD^+ ratio (Appendix I). Peredox was specific against other metabolites structurally related to

NADH, such as NADPH, $NADP^+$, ADP ribose, nicotinamide, β-nicotinamide mononucleotide, AMP, and adenosine. Not only was there no change in its fluorescence response upon addition of these metabolites, but also the NADH:NAD^+ titrations in their presence were similar to that of control (Appendix I). The main interference came from ADP and ATP, with an apparent affinity (K_i) in the millimolar range, consistent with published data on B-Rex (Wang et al., 2008). In Peredox, while the specificity of binding NADH over ADP or ATP was roughly 30,000-fold, NADH is far less abundant than ADP or ATP in typical intracellular environments. Although physiological levels of ADP and ATP could compete with NADH and NAD^+ for binding, ADP and ATP act similarly to each other, at various pH's and temperatures; also, the interference from ADP and ATP is less prominent with increasing NAD^+ (Figure 2.2B). Thus, while Peredox might be slightly sensitive to changes in the total adenine nucleotide pool size, its response is not affected by changes in the cellular energy charge, or the ATP:ADP ratio (Appendix I). While metabolic challenges often lead to energy deprivation and decrease in cytosolic ATP:ADP ratio, changes in cytosolic adenine nucleotide pool size are minimal (Schwenke et al., 1981; Malaisse and Sener, 1987) and would not be expected to interfere with Peredox response. In addition, Peredox exhibited much improved kinetics over P0. To determine the rate of NADH dissociation from the biosensor, we added the LDH enzyme with pyruvate to consume the free NADH and monitored the response over time. While NADH dissociation from P0 was slow, with a time constant of 25 minutes at 25°C, NADH dissociation from Peredox was much faster, with a time constant of 50 seconds at 25°C and 16 seconds at 35°C (Figure 2.2C).

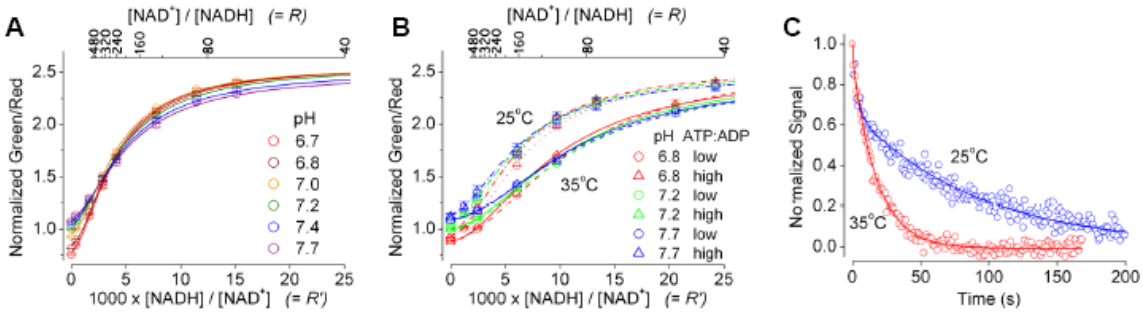

Figure 2.2. Characterization of purified Peredox

(A) Green to red fluorescence ratios at the indicated pH, plotted against *R′* or *R* (above the plot), with 80 μM NAD^+ at 25°C. (B) Fluorescence ratios at the indicated pH, temperature, and ATP:ADP ratios (low, 0.3; high, 3.6; with total adenine nucleotides of 4.6 mM), plotted against *R′* or *R* (above the plot), with 80 μM NAD^+. Fluorescence ratios (mean ± SEM, $n = 3$) were normalized to the control condition in the absence of pyridine nucleotides at pH 7.2. (C) Kinetics of fluorescence signal upon addition of pyruvate and LDH to Peredox pre-equilibrated with saturating NADH at 25°C or 35°C, normalized to initial and final values.

Peredox reports the cytosolic NADH-NAD^+ redox state in mammalian cells

After characterizing Peredox-mCherry as a purified protein, we validated its utility in mammalian cells. We expressed Peredox-mCherry in cultured mouse neuroblastoma Neuro-2a cells and monitored its fluorescence response. Under confocal microscopy, the sensor fluorescence in both green and red images was fairly uniform through the cell (Figure 2.3A). The pixel-by-pixel ratio of the green image divided by the red image appeared consistent, with no apparent difference observed between cytosolic and nuclear signals. To test whether Peredox could report the cytosolic NADH-NAD^+ redox state, we varied the concentrations of lactate and pyruvate in the extracellular solution, thereby altering the intracellular concentrations of these metabolites (Bücher et al., 1972). Interconversion between lactate and pyruvate catalyzed by endogenous LDH should lead to concomitant exchange between cytosolic NADH and NAD^+ species. Note

that cells were not permeabilized, and glucose was absent in the extracellular solution. With widefield time-lapse microscopy, we monitored changes in fluorescence response of Peredox. In addition, we established that cellular background autofluorescence was far weaker and did not interfere with Peredox fluorescence signal. In the presence of lactate (10 mM), the green to red fluorescence ratio of Peredox was maximal (Figure 2.3B). After adding incremental amounts of pyruvate, we observed a stepwise decrease in the green to red fluorescence ratio, with millimolar pyruvate reducing the ratio down to 40% of the maximal value. This signal change was consistent with oxidation of NADH into NAD^+ and a concurrent reduction of pyruvate into lactate. After each solution switch, the signal adjusted rapidly and arrived at a new steady state in a few minutes. The steady state fluorescence response of Peredox depended systematically on the lactate:pyruvate ratio in the extracellular solution (Figure 2.3C); the lactate:pyruvate ratio required for a half maximal response was ~40. To test the robustness of this ratio-sensing behavior, we repeated the experiments with different total concentrations of lactate and pyruvate. In each case, the lactate:pyruvate ratio, rather than their absolute concentrations, determined the response. We could also plot the Peredox response to the extracellular lactate:pyruvate ratio as a function of predicted NADH:NAD^+ ratio (Figure 2.3D), by using the known equilibrium constant of the LDH reaction (Williamson et al., 1967) and assuming a constant physiological pH of 7.4. For comparison we also show the data from purified Peredox proteins, with total adenine nucleotide of 4.6 mM and free NAD^+ of 80 μM, consistent with published estimates (Veech et al., 1979; Zhang et al., 2002).

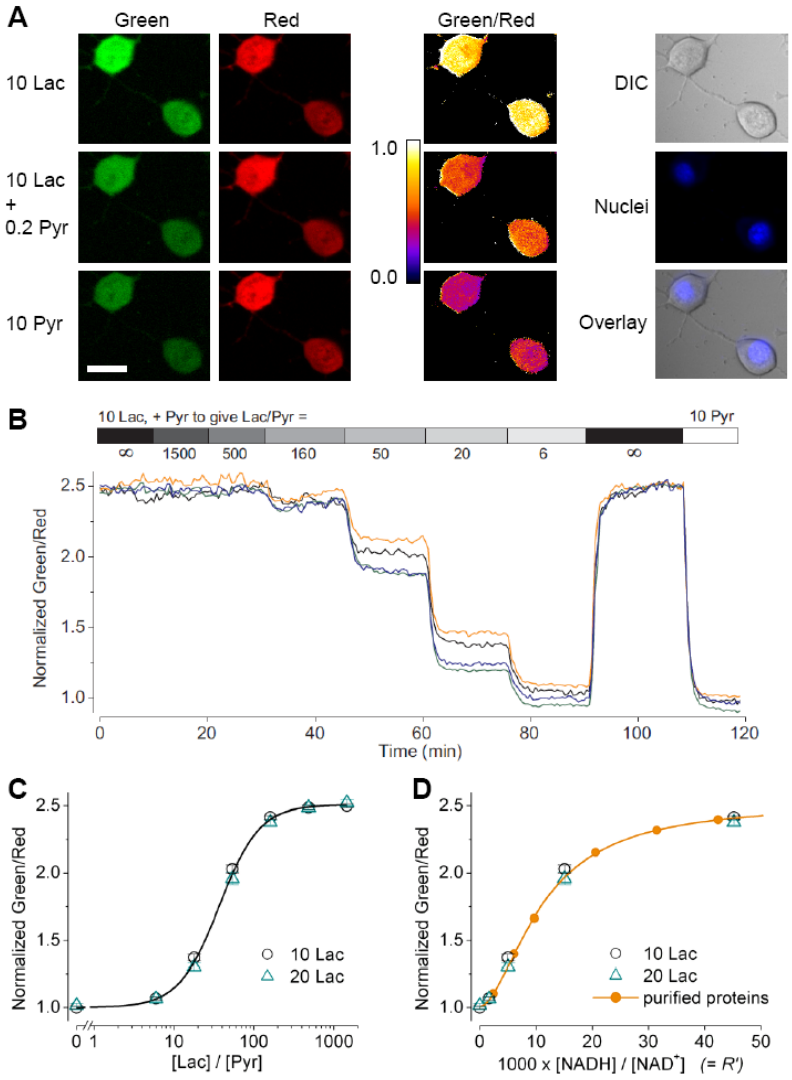

Figure 2.3. Imaging the cytosolic NADH-NAD$^+$ redox state in various extracellular lactate:pyruvate ratios

(A) Left: Confocal green and red fluorescence images of two cultured mouse neuroblastoma Neuro-2a cells expressing Peredox supplied with 10 mM lactate, 10 mM lactate plus 0.2 mM pyruvate, or 10 mM pyruvate. Scale bar 20 µm. Middle: Pseudocolored pixel by pixel green to red ratio images. The slight edge effect seen is likely due to the optical z-shift of 1.5 µm between the green and red confocal images. Right: Widefield differential interference contrast (DIC), nuclear staining, and the overlay image. (B) Time course of fluorescence ratios of four Neuro-2a cells perfused with the indicated lactate:pyruvate ratios. (C) Steady state fluorescence responses of Neuro-2a cells plotted against extracellular lactate:pyruvate ratios, with lactate of 10 mM or 20 mM (mean ± SEM, n = 12–15 cells from two independent experiments). (D) Steady state fluorescence responses in (D) plotted against the predicted R', by assuming the LDH reaction was at equilibrium and a pH of 7.4. Data of purified Peredox proteins were with 80 µM NAD$^+$ and 4.6 mM total adenine nucleotides at 35°C. Line fitted with a logistic function using a Hill coefficient of 1.8.

In both the dynamic range and the relative affinities for NADH and NAD^+, there is good agreement between the sensor responses in cells and from purified proteins. Therefore, Peredox reports cytosolic NADH:NAD^+ ratios in mammalian cells. Furthermore, since in the absence of glucose we could use exogenous lactate and pyruvate to set the cytosolic NADH:NAD^+ redox, it appears that lactate and pyruvate equilibrate readily between extracellular and intracellular environments, and that the LDH reaction is approximately at equilibrium.

Glycolysis opposes the LDH equilibrium to produce a reduced cytosolic NADH-NAD^+ redox state in cultured cells

In addition to LDH, glucose metabolism via glycolysis at the glyceraldehyde-3-phosphate dehydrogenase (GAPDH) reaction would be expected to affect the cytosolic NADH-NAD^+ redox state. In cultured Neuro-2a cells supplied with glucose alone, we found the sensor signal to be maximal (Appendix I). To test whether such a strongly reduced cytosolic NADH-NAD^+ redox state depended on glucose metabolism, we performed the following experiments. First, we varied the concentration of glucose in the extracellular solution. Not only was the signal minimal in the absence of glucose, but also its steady state fluorescence response depended on the glucose supply; the glucose concentration required for a half maximal response was ~0.2 mM (Figure 2.4A). Second, when we applied iodoacetate, which irreversibly inhibits GAPDH, the signal promptly decreased (Appendix I), indicating a decline in cytosolic NADH consistent with glycolytic inhibition. Therefore, the reduced cytosolic NADH-NAD^+ redox state in cultured Neuro-2a cells supplied with glucose depended on both the presence of glucose

and the GAPDH reaction. Nevertheless, given that lactate and pyruvate could equilibrate across the cell membrane readily, intracellular lactate and pyruvate might be washed away in cells that were perfused with glucose alone. If availability of intracellular pyruvate were to become limiting for the LDH reaction, this could account for the reduced NADH-NAD^+ redox state in these cultured cells. To address this concern, we systematically varied the total concentrations of extracellular lactate and pyruvate (while keeping a constant lactate:pyruvate ratio of 10), with or without supplying glucose (Figure 2.4B). On one hand, when glucose was absent, Peredox indicated a cytosolic NAD^+:NADH ratio of ~300 across a wide range of total lactate and pyruvate concentrations. On the other hand, when glucose was present, the cytosolic NADH-NAD^+ redox state became significantly more reduced. While this observation appeared more pronounced at lower concentrations of lactate and pyruvate, it held across a wide concentration range. With physiological amounts of lactate and pyruvate (totaling 0.8 to 4 mM; Williamson et al., 1967), glucose metabolism reduced cytosolic NAD^+:NADH ratios by 2- to 4-fold to 70–130, when availability of intracellular pyruvate should not be limiting. We obtained similar results in another cultured tumor cell line, rat glioma C6 (Appendix I). In both cases, the redox status of cytosolic NADH-NAD^+ was no longer determined by the LDH reaction alone, but rather by a balance between the LDH reaction and glycolysis.

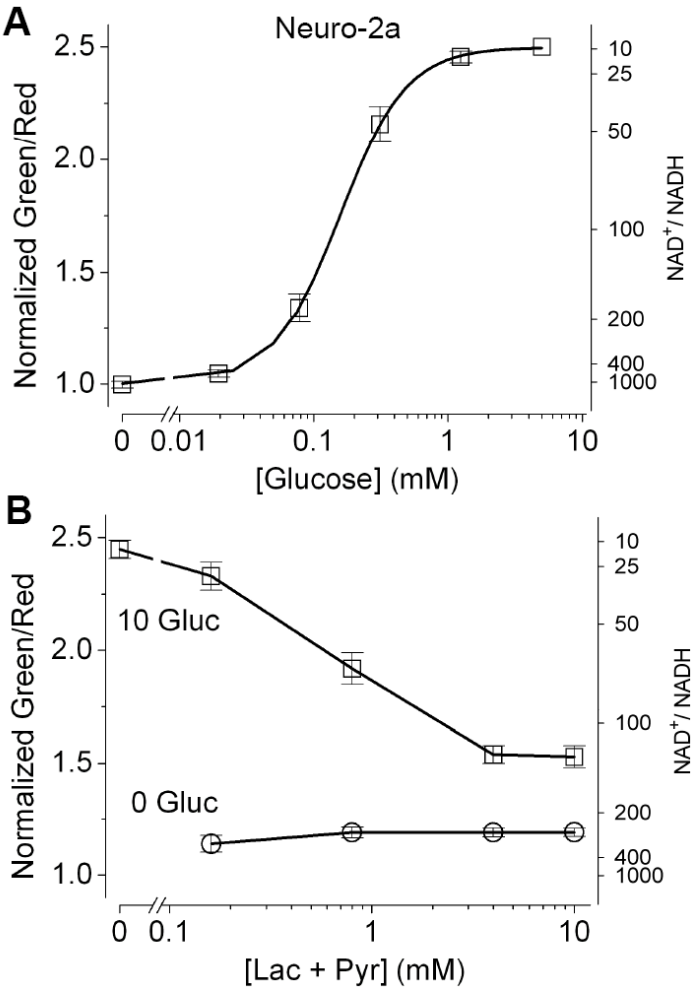

Figure 2.4. Cultured mouse neuroblastoma Neuro-2a cells supplied with glucose show a more reduced cytosolic NADH-NAD^+ redox state

(A) Steady state fluorescence responses of Neuro-2a cells plotted against concentrations of extracellular glucose (mean ± SEM, n = 19 cells from two independent experiments). (B) Steady state fluorescence responses of Neuro-2a cells plotted against total concentrations of extracellular lactate and pyruvate, with a constant lactate:pyruvate ratio of 10, and glucose of 10 mM or 0 mM (mean ± SEM, n = 7 cells from three independent experiments). For the alternate y axis, the predicted NAD^+:NADH ratio was calculated from purified protein measurements. $p < 0.001$ (paired t-test) for all conditions in 10 mM vs. 0 mM glucose.

Primary cultured cortical astrocytes and neurons differ in their cytosolic NADH-NAD^+ redox states

Glucose metabolism has been proposed to differ in astrocytes and neurons (Pellerin and Magistretti, 1994; Herrero-Mendez et al., 2009). To investigate whether their cytosolic NADH-NAD^+ redox states differ, we expressed Peredox-mCherry in primary cultured mouse cortical astrocytes and neurons. However, we observed bright red puncta that appeared to be lysosomal aggregates due to accumulation of mCherry (Katayama et al., 2008); these red puncta rendered the normalized signal unreliable. To circumvent this problem, we used a nuclear targeted version (Nagai et al., 2001) of Peredox to measure nuclear NADH signals. Since there is presumably no diffusion barrier for free NADH and NAD^+ between nuclear and cytosolic compartments (and we saw no difference between nuclear and cytosolic signals in cultured cells), our nuclear signals should indicate the cytosolic NADH-NAD^+ redox state (Zhang et al., 2002). When measured under the same conditions, primary astrocytes showed significantly more reduced cytosolic NADH-NAD^+ redox states than primary neurons (Figure 2.5). Furthermore, upon glucose withdrawal, both cell types promptly showed a decline in cytosolic NADH. For both primary astrocytes and neurons, similar to cultured Neuro-2a cells (Figure 2.3B), perfusion with lactate (10 mM) alone yielded maximal fluorescence response, whereas the signal became minimal upon pyruvate (10 mM) perfusion.

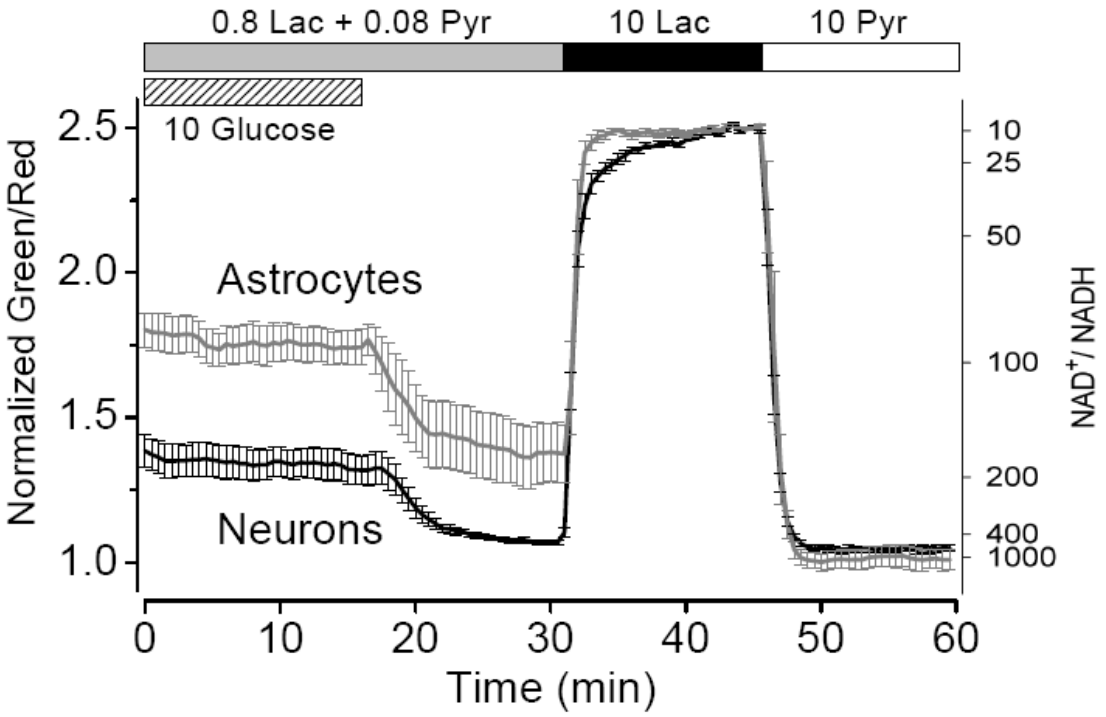

Figure 2.5. Primary cultured mouse cortical astrocytes and neurons differ in their cytosolic NADH-NAD$^+$ redox states

Time course of fluorescence ratios of primary mouse cortical astrocytes or neurons expressing Peredox-NLS and perfused with solutions as indicated (mean ± SEM, n = 4–5 cells from four independent experiments). For the alternate y axis, the predicted NAD$^+$:NADH ratio was calculated from purified protein measurements. $p < 0.01$ (paired t-test) for astrocytes vs. neurons prior to the 10 mM lactate condition.

Stably expressed in MCF-10A cells, Peredox reports cytosolic NADH decrease upon PI3K pathway inhibition

Given that glucose metabolism is regulated by growth factor signaling including the PI3K/Akt/mTOR pathway (Vander Heiden et al., 2009, Sengupta et al., 2010), we explored the effects of PI3K pathway signaling on glucose metabolism as indicated by the cytosolic NADH-NAD^+ redox state. To this end, we generated a cultured mammary epithelial MCF-10A cell line stably expressing nuclear targeted Peredox-mCherry; the nuclear targeting allowed us to distinguish individual cells easily and enabled the use of high-content image analysis to monitor hundreds of cells concurrently in a multi-well imaging experiment (Jones et al., 2008). At the baseline condition, MCF-10A cells showed reduced cytosolic NADH-NAD^+ redox states (Figure 2.6A). Upon the application of a dual inhibitor of PI3K and mTOR, NVP-BEZ235 (Maira et al., 2008), we observed a decrease in cytosolic NADH level in nearly all cells over the course of an hour (Figure 2.6B). This NADH decline was consistent with the expected glycolytic inhibition as a consequence of inhibiting PI3K pathway signaling. Cytosolic NADH-NAD^+ redox states were unaffected in cells treated with the DMSO vehicle control. Afterwards, as a control, we applied reagents that were known to perturb cytosolic NADH-NAD^+ redox states: application of lactate (20 mM) alone, lactate (20 mM) and pyruvate (1 mM), and pyruvate (20 mM) with the glycolytic inhibitor iodoacetate (0.4 mM) could poise these cells to high, medium, and low cytosolic NADH levels, respectively. The fluorescence responses to these control treatments were remarkably similar between the drug-treated and the control groups (Figure 2.6C).

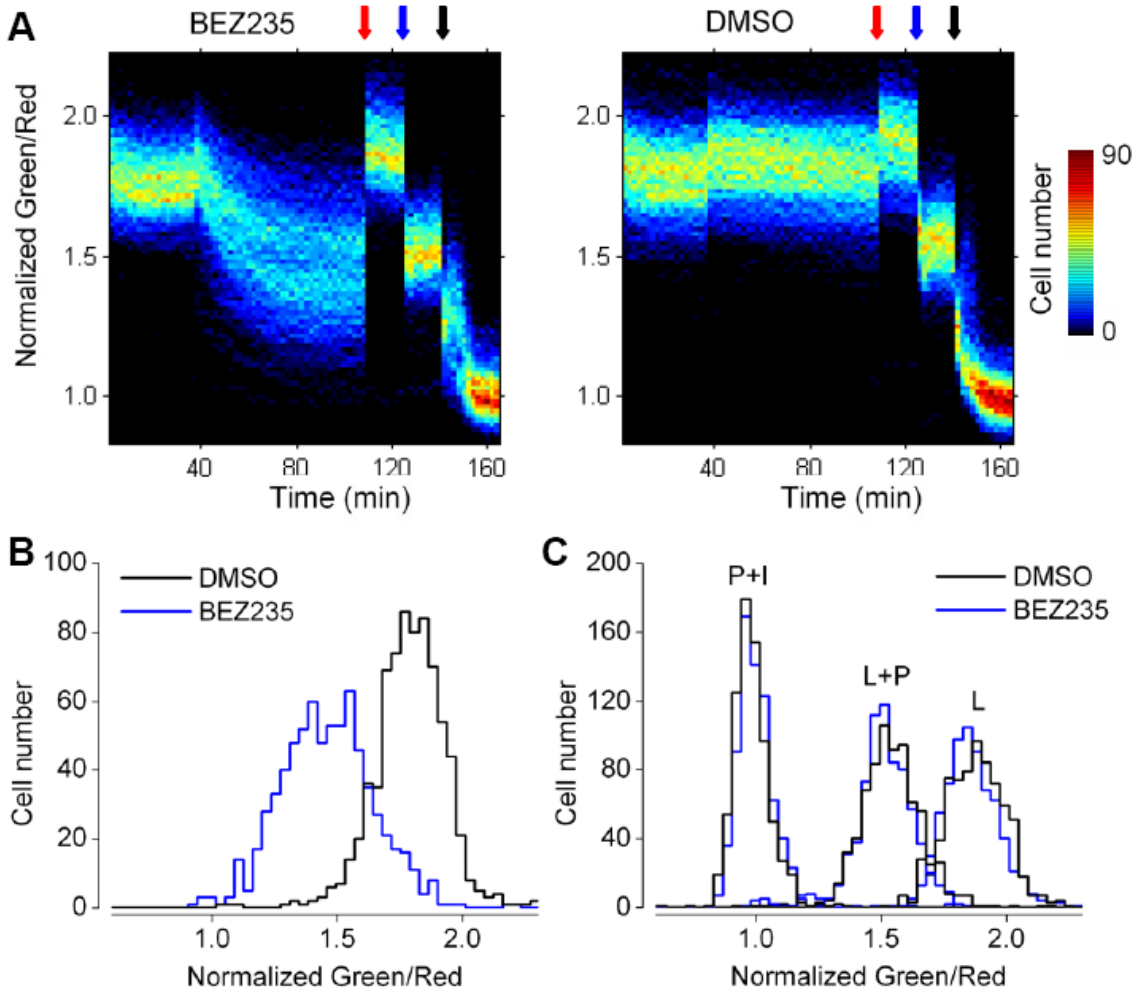

Figure 2.6. Stably expressed in mammary epithelial MCF-10A cells, Peredox reports cytosolic NADH decrease upon PI3K pathway inhibition

(A) Heat maps of normalized fluorescence ratios of MCF-10A cells stably expressing Peredox-NLS plotted against time. After 38 minutes of baseline, cells were treated with 1 µM NVP-BEZ235 (left) or DMSO (right). As a control, 20 mM lactate, 20 mM lactate and 1 mM pyruvate, and 20 mM pyruvate and 0.4 mM iodoacetate were applied at red, blue, and black arrows, respectively. For each group, ~700 cells from six fields in two experiments were collected. While the dynamic range was less than the usual 2.5-fold, this was likely due to inadequate control of extracellular lactate and pyruvate concentrations, as these cells were imaged in the 24-well plate formats and solutions were changed without rinsing, as opposed to imaging in a chamber under continuous perfusion of fresh solutions. Fluorescence ratios binned in increments of 0.012. (B) Histograms of normalized fluorescence ratios after one-hour treatment with DMSO (black) or NVP-BEZ235 (blue), binned in increments of 0.027. (C) Histograms of normalized fluorescence ratios from the indicated groups after calibration with 20 mM lactate (L), 20 mM lactate and 1 mM pyruvate (L+P), and 20 mM pyruvate and 0.4 mM iodoacetate (P+I).

DISCUSSION

We exploited the conformational change of the Rex protein upon NADH binding to engineer a cpFP-based biosensor of the cytosolic NADH-NAD^+ redox state. Although the initial construct reported [NADH] × [H^+] / [NAD^+], optimization via targeted mutagenesis eliminated its pH sensitivity. This genetically encoded fluorescent biosensor, Peredox, reported cytosolic NADH:NAD^+ ratios in mammalian cells. Its fluorescence signal could be calibrated with exogenous lactate and pyruvate. With transient or stable expression, we demonstrated its utility in various cultured and primary cell types. In cultured mammalian cells, we found that glucose metabolism via glycolysis opposed the lactate dehydrogenase equilibrium to produce a reduced NADH-NAD^+ redox state. We also observed different cytosolic NADH-NAD^+ redox states in primary mouse astrocytes and neurons under identical conditions, consistent with their hypothesized metabolic differences. Finally, using Peredox stably expressed in cultured MCF-10A cells, we monitored changes in cytosolic NADH-NAD^+ redox states from hundreds of individual cells upon inhibition of PI3K pathway signaling.

Peredox presents several advantages over conventional chemical methods and NAD(P)H autofluorescence in monitoring the cytosolic NADH-NAD^+ redox state. Using chemical methods, NADH and NAD^+ can be quantified directly in cell extracts, but these measurements detect the total amounts of NAD(H) and ignore their subcellular location. As most cellular NADH resides in the mitochondria, cytosolic NADH determination with such methods can be complicated by substantial contamination from the mitochondrial NADH pool. Also, such direct chemical methods cannot distinguish between protein-bound and free species of NAD(H). These measurements of total NADH:NAD^+ ratios

often vastly overestimate the actual cytosolic free NADH:NAD^+ ratios, owing to sequestration from cellular proteins that is greater for NADH than for NAD^+. Considering that free NADH:NAD^+ ratio is the pertinent parameter for biological NADH-NAD^+ redox reactions, other chemical methods have been devised to extract and quantify redox couples such as lactate and pyruvate. Assuming that the LDH reaction is at equilibrium, the lactate:pyruvate ratios can be used to infer the free NADH:NAD^+ ratios in the cytosol, assuming a constant known pH (Williamson et al., 1967). However, such indirect methods can be affected by changes in cellular pH as well as by contamination from the mitochondrial fraction. More importantly, the assumption that the LDH reaction is at equilibrium has not been examined. As we have shown, cultured tumor cells such as Neuro-2a and C6 supplied with glucose showed a reduced cytosolic NADH-NAD^+ redox state, despite the abundance of exogenous lactate and pyruvate present at a ratio chosen to keep it oxidized. From a measurement standpoint, this indicates that the LDH reaction was likely not at equilibrium, and thus the measurement of cytosolic free NADH:NAD^+ ratios using Peredox is likely to be more reliable than indirect methods using lactate:pyruvate ratios. Besides, unlike chemical methods, Peredox can be used to monitor cytosolic NADH-NAD^+ redox states in intact, individual cells.

In comparison to the endogenous NAD(P)H autofluorescence, Peredox is a bit slower, but much more specific and sensitive in monitoring the cytosolic NADH-NAD^+ redox state. Given its kinetics, Peredox can report NADH-NAD^+ redox dynamics with a time resolution of a few seconds. It may be difficult to use it to monitor faster events, such as the dip and the overshoot of endogenous NAD(P)H autofluorescence observed in

brain slices (Shuttleworth et al., 2003; Kasischke et al., 2004). Nonetheless, NAD(P)H autofluorescence reflects the combined signal of NADH and NADPH and is therefore not specific for NADH alone (Avi-Dor et al., 1962; Rocheleau et al., 2004). Also, since the autofluorescence is contributed mostly by protein-bound NAD(P)H species, changes in intracellular environment such as pH could affect the NAD(P)H-protein interaction and the autofluorescence signal (Ogikubo et al., 2011). In contrast, Peredox detects free NADH and reports the biologically relevant NADH:NAD^+ ratio, and its response is highly specific for NADH over NADPH. Furthermore, Peredox is roughly 100-fold brighter than NAD(P)H autofluorescence. With Peredox we could reliably monitor cytosolic NADH, which is difficult to measure with autofluorescence imaging, particularly in the face of bright mitochondrial autofluorescence (nuclear autofluorescence has been used as a proxy for cytosolic autofluorescence; Patterson et al., 2000). Lastly, since NAD(P)H autofluorescence requires ultraviolet (one-photon) excitation, which could induce cell toxicity, two-photon microscopy is usually performed instead. Conversely, with a red-shifted excitation wavelength and brighter fluorescence, Peredox can be used in conventional one-photon microscopy, thereby simplifying the technical requirements for imaging experiments.

In designing Peredox, we have substantially minimized the interference of pH. In general, upon metabolic manipulations, changes in intracellular pH are common. This may interfere with biosensor measurements by altering the GFP fluorescence or the ligand-binding protein scaffold. Many cpFP-based fluorescent biosensors are pH sensitive, with pK_a's near the physiological range (Nagai et al., 2001; Belousov et al., 2006; Nausch et al., 2008; Berg et al., 2009). For some biosensors, a pH fluctuation of

0.3 units could be mistaken for the entire excursion of the sensor response. Fluorescence modulation in cpFP-based sensors has been attributed to a shift in the pK_a of the chromophore upon ligand binding to the detector domain (Baird et al., 1999). Despite the apparent requirement for pH sensitivity inherent in this proposed mechanism, we decided to use a pH-resistant GFP. In doing so we hoped to modulate the cpFP's quantum yield rather than its pK_a upon NADH sensing. For this reason we chose the circularly permuted T-Sapphire (Zapata-Hommer and Griesbeck, 2003), a GFP variant notable for a low pK_a of ~5. Its chromophore remains almost neutral in the ground-state and ionizes only upon excitation, leading to green emission with a substantial Stokes shift of ~110 nm. We optimized the sensor response in the pH insensitive regime of the GFP (corresponding to the physiological pH range in cells). The resulting biosensor is far more pH resistant and, unlike many other cpFP-based sensors, does not need pH measurement and correction, unless large pH changes are expected and high precision is needed. Moreover, the use of a pH resistant cpFP in the sensor design allowed us to uncover the inherent pH sensitivity of the NADH-binding protein scaffold. We initially conceived T-Rex as a sensor of the NADH:NAD^+ ratio, so we were surprised to find that it depended on [NADH] × [H^+] / [NAD^+]. Given the tight hydrophobic nicotinamide-binding pocket, the implication of a single proton transfer upon NAD(H) binding in Rex was unexpected. We were nevertheless able to eliminate its intrinsic pH dependence via directed mutagenesis of the conserved residue Tyr98.

In using a genetically encoded biosensor, a potential concern is whether it will perturb the biological systems that it is used to measure; however, Peredox seems unlikely to perturb cellular free NADH by either catalysis or buffering. The dependence

of Rex on [NADH] × [H^+] / [NAD^+] is reminiscent of the equilibrium constant of NADH-binding dehydrogenases, raising the question of whether Rex is not just an NADH-binding protein but also a redox enzyme. If the Rex-based biosensor were to have catalytic activity, it could alter the level of cellular NADH, and binding or release of NAD(H) might depend on the presence of substrate (Kumar et al., 2002). Yet, structural and biochemical evidence seems to suggest that Rex does not possess any catalytic activity. The T-Rex structure reveals a compact hydrophobic pocket enclosing the nicotinamide moiety of the NADH molecule, without a cavity for substrate accommodation or polar functional groups characteristic of redox enzymes (Sickmier et al., 2005). Also, most NADH-binding dehydrogenases exhibit some catalysis even with non-optimal substrates. We however observed no oxidation of NADH in Rex upon pyruvate application (50 mM for >20 hours), unlike the case for the eukaryotic transcriptional corepressor C-terminal binding protein (Kumar et al., 2002). Even if Rex were a redox enzyme, the mutation at the highly conserved Tyr98 residue would likely spoil any potential catalytic activity in Peredox. In addition, another concern was that Peredox might perturb the cytosolic free NADH pool by direct binding and buffering. However, this effect is likely to be negligible, as cytosolic NADH is probably buffered by the endogenous protein-bound pool, constituting ~95% of the total cytosolic NADH (Zhang et al., 2002). With a total cytosolic NADH concentration of 3 μM, biosensor expression (at 1–10 μM; Akerboom et al., 2009) is expected to change cellular NADH buffering capacity by roughly 4-fold or less.

To normalize Peredox measurements, a second FP mCherry was attached in tandem. In primary cultured cells, we found expression of RFP such as mCherry led to

lysosomal aggregates as previously reported (Katayama et al., 2008). As these puncta preclude reliable comparison of the green-to-red fluorescence ratios, we instead used a nuclear targeted version of Peredox-mCherry. Possible alternative approaches to avoid puncta include the use of another FP such as mCitrine (Griesbeck et al., 2001) for normalization, or fluorescence lifetime imaging to obtain self-normalized measurements without using a second FP (Tantama et al., 2011).

Being genetically encoded, Peredox may be targeted to various cell types and compartments to monitor cellular and subcellular variations in NADH metabolism. However, Peredox with its current affinity would not be expected to work well in mitochondria, as mitochondrial NADH:NAD^+ ratio has been estimated to be 100- to 1000-fold higher than cytosolic NADH:NAD^+ ratio (Williamson et al., 1967). Consistent with this estimate, when we targeted Peredox to mitochondrial matrix, we did not observe any signal change upon metabolic challenges. Nevertheless, it may be possible to re-engineer its NADH binding sites for mitochondrial redox sensing.

Glycolysis opposes the lactate dehydrogenase equilibrium to produce a reduced cytosolic NADH-NAD^+ redox state in cultured Neuro2a and C6 cancer cells. From a biological standpoint, the measured value of the cytosolic NADH-NAD^+ redox is surprisingly reduced, corresponding to an NAD^+:NADH ratio of <150, compared with a typical range of 200–700 from tissue estimates under a range of conditions (Williamson et al., 1967). Qualitatively, this is not unexpected: cancer cells are known to undergo aerobic glycolysis (Warburg, 1956), whereby most of the glucose is metabolized into lactate, and the production of lactate from pyruvate is presumably driven by elevated NADH:NAD^+ ratios. However, at these extremely reduced redox values, it seems

surprising that the GAPDH reaction can proceed forward to establish net glycolysis and a net production of NADH (Cerdán et al., 2006). The reduced redox level is dependent on the presence of glucose, arguing against net gluconeogenic flux. Perhaps the net forward flux through glycolysis is driven by rapid consumption of intermediate metabolites via pathways downstream of the GAPDH reaction, in accordance with the high biosynthetic requirements of cancer cells (Vander Heiden et al., 2009). In addition, considering that the GAPDH reaction has been proposed to be coupled to the subsequent step, the 3-phosphoglycerate kinase (PGK) reaction (Veech et al., 1979), future imaging experiments of both cytosolic NADH:NAD^+ ratio and ATP:ADP ratio (Berg et al., 2009) could yield insights on how these parameters and the potential coupling between these two reactions regulate the state of glycolysis.

We found a difference in cytosolic NADH-NAD^+ redox between primary cultures of cortical astrocytes and neurons, measured under identical conditions of extracellular glucose, lactate, and pyruvate. This redox difference, as observed in separately cultured cells, is consistent with the proposed redox gradient between astrocytes and neurons (Cerdán et al., 2006). More generally, this redox difference is consistent with the hypothesis that glucose metabolism in the brain is compartmentalized, with different cell types performing distinct metabolic functions. While cytosolic NADH-NAD^+ redox states in cultured cells are likely to be different from *in vivo*, Peredox, being genetically encoded, should in the future allow us to monitor NADH metabolism in astrocytes and neurons more physiologically, such as in brain slice preparations and *in vivo*.

By expressing Peredox stably in a cultured cell line, we could monitor changes in cytosolic NADH-NAD^+ redox states in hundreds of individual cells upon perturbation of

PI3K pathway signaling. We demonstrated that Peredox can be used in a high-content imaging format to obtain kinetically detailed metabolic data from individual cells. In the future, Peredox should facilitate studies on how NADH-NAD^+ redox metabolism is regulated by growth factor signaling pathways in live cells, as well as how individual cell responses correlate with the status of other signaling systems. As a reporter of the cellular NADH-NAD^+ redox state, Peredox should open the door to a better understanding of such potentially elaborate organization of metabolism and bioenergetics, as well as the consequences of such metabolic regulation for cellular signaling and physiology.

EXPERIMENTAL PROCEDURES

Gene Construction and Protein Characterization

Gene construction and characterization of the sensor are described in Supplemental Information. Sequences and plasmids for expression of Peredox have been deposited with Addgene.

Cell Culture, Transfection, and Transduction

Cells were maintained in 95% air and 5% CO_2 at 37°C. Mouse neuroblastoma Neuro-2a cells (CCL-131, American Type Culture Collection) were cultured in Minimal Essential Medium (MEM; all media and serum from Invitrogen) with 10% fetal bovine serum (FBS), 24 mM $NaHCO_3$, 2 mM HEPES, and 1 mM sodium pyruvate. Rat glioma C6 cells (CCL-107, ATCC) were cultured in Dulbecco's modified Eagle's medium–nutrient mixture Ham's F-12 (DMEM/F-12) with 2.5% FBS and 14 mM $NaHCO_3$, pH 7.1 (NaOH). Neuro-2a and C6 cells were plated onto protamine coated coverslips 4–8 hr prior to transfection using Effectene (Qiagen). The next day, Neuro-2a and C6 cells were rinsed with phosphate buffered saline and maintained in MEM with 1% FBS, 24 mM $NaHCO_3$, 2 mM HEPES, 1 mM sodium pyruvate, and 100 units/ml penicillin with 100 μg/ml streptomycin (pen-strep; Lonza). For Neuro-2a differentiation, 10–20 μM retinoic acid was added. Primary dissociated mouse cortical astrocytes (P0–P2) and neurons (E16–E18) were prepared as described (Bartlett and Banker, 1984) and seeded onto poly-D-lysine coated plates in MEM supplemented with 10% horse serum, 33 mM glucose, 2 mM glutamine (Lonza), 1 mM sodium pyruvate, and pen-strep for 3 hr. Then, primary astrocytes were maintained in DMEM/F-12 with 10% FBS, 24 mM $NaHCO_3$, and pen-

strep, and they were passed twice before transfection using Effectene on DIV (days in vitro) 21. Primary neurons were maintained in Neurobasal medium with B27 serum free supplements, 2 mM glutamine, and pen-strep before transfection using calcium phosphate on DIV 4. For stable expression of Peredox-NLS, mammary epithelial MCF-10A cells (CRL-10317, ATCC) were transduced using the retroviral pMSCV vector followed by puromycin selection. MCF-10A cells were cultured in DMEM/F-12 with 5% horse serum, 20 ng/ml epidermal growth factor (EGF), 0.5 μg/ml hydrocortisone, 100 ng/ml cholera toxin, 10 μg/ml insulin, and pen-strep, as described (Debnath et al., 2003).

Confocal and Widefield Time-lapse Microscopy

Cells were imaged 2–5 days after transient transfection. The extracellular solution contained (in mM): 121.5 NaCl, 25 $NaHCO_3$, 2.5 KCl, 2 $CaCl_2$, 1.25 NaH_2PO_4, and 1 $MgCl_2$, bubbled with 95% air and 5% CO_2, delivered at 2–3 ml / min at 33–35°C. Glucose, lactate, and pyruvate were supplemented as indicated. Primary astrocytes and neurons were in the initial condition for 40–60 min prior to image acquisition. Confocal images were acquired on an inverted Nikon Eclipse TE300 microscope mounted with an Andor Revolution Differential Spinning Disk (DSD) unit for optical sectioning controlled by iQ software. Excitation light from Prior Lumen Pro passed through Semrock 405/10 nm or 578/16 nm filters. The DSD unit contained a Chroma 59022bs dichroic with Omega 490 nm and 590 nm short pass filters. Emission light passed through a Chroma 59022m filter with Semrock 525/50 nm or 629/56 nm filters. Using the high sectioning mode, confocal images were acquired with ~4.5 μm thickness with 2 s exposure and 1×1 binning, using a Nikon 20×/0.75 Plan Apo objective. Nuclei were stained with

InVitrogen SYBR-safe. Widefield images were acquired with a PCO Sensicam QE CCD camera mounted on an Olympus BX51 upright microscope, with a Zeiss 20×/0.5 Achroplan or an Olympus 60×/0.9 LUMPlanFl/IR objective. A TILL Photonics Polychrome IV monochromator with a 12.5 nm slit width was used with a Chroma 69002x exciter, a 69002bs dichroic, and a dual band Semrock FF01-524/628-25 emitter. Green and red images were acquired at 405 nm and 575 nm excitation every 20–30 s with 3–40 ms exposure and 4×4 binning. Using TILLvisION v4.0.1 image software or ImageJ, we subtracted background, set threshold to avoid ratioing artifacts, and generated a pixel-by-pixel green to red ratio image for each time point. Fluorescence response of each cell in 10 mM lactate was defined as 2.5, and data was normalized accordingly. For stable MCF-10A experiments, ~500 cells were plated onto the center of each well of a 24-well plate 2-3 days prior. Prior to image acquisition, cells were in phenol red-free RPMI supplemented with 0.3% BSA, EGF, hydrocortisone, cholera toxin, and insulin, at 37°C and 5% CO_2 for 40–60 min. Cells were then treated with BEZ235 (1 μM) or the vehicle control DMSO and calibrated with lactate, pyruvate, and iodoacetate as indicated. Widefield images were acquired using a Nikon inverted Eclipse Ti microscope, equipped with a Nikon 20×/0.75 Plan Apo objective and an environmental chamber. Green fluorescence was obtained with a Chroma ET405/20x exciter, a T425LPXR dichroic, and an ET525/50m emitter; red fluorescence, a HQ575/50x exciter, a Q610LP dichroic, and a HQ640/50m emitter. Images were taken every 2 min with 100 ms exposure and 2×2 binning. Using a custom built MATLAB program (Jones et al., 2008), we subtracted background, set threshold and cell segmentation, and generated a green to red ratio for

each cell for each time point. Data were analyzed using MATLAB (MathWorks) and Origin 6.0 (MicroCal).

ACKNOWLEDGMENTS

We thank T. Abramson for expert technical assistance; D. Clapham and B. Sabatini for providing GFP constructs; J. Flanagan for providing Neuro-2a; J. Berg, J. Brugge, L. Cantley, D. Clapham, J. Cohen, N. Danial, T. Schwarz, M. Vander Heiden, and members of the Yellen lab for their comments. This work was supported by the US National Institutes of Health (R01 NS055031 to G.Y.), an NIH postdoctoral fellowship (F32 NS066613 to M.T.), the U.S. Army Breast Cancer Research Program multidisciplinary postdoctoral fellowship (W81XWH-08-1-0609 to J.G.A.), as well as an Albert J. Ryan fellowship and a Stuart H. Q. and Victoria Quan predoctoral fellowship in neurobiology (to Y.P.H.).

REFERENCES

Akerboom, J., Rivera, J. D. V., Guilbe, M. M. R., Malavé, E. C. A., Hernandez, H. H., Tian, L., Hires, S. A., Marvin, J. S., Looger, L. L. and Schreiter, E. R. (2009). Crystal structures of the GCaMP calcium sensor reveal the mechanism of fluorescence signal change and aid rational design. J Biol Chem *284*, 6455–6464.

Avi-Dor, Y., Olson, J. M., Doherty, M. D. and Kaplan, N. O. (1962). Fluorescence of pyridine nucleotides in mitochondria. J Biol Chem *237*, 2377–2383.

Baird, G. S., Zacharias, D. A. and Tsien, R. Y. (1999). Circular permutation and receptor insertion within green fluorescent proteins. Proc Natl Acad Sci U S A *96*, 11241–11246.

Bartlett, W. P. and Banker, G. A. (1984). An electron microscopic study of the development of axons and dendrites by hippocampal neurons in culture. I. Cells which develop without intercellular contacts. J Neurosci *4*, 1944–1953.

Bücher, T., Brauser, B., Conze, A., Klein, F., Langguth, O. and Sies, H. (1972). State of oxidation-reduction and state of binding in the cytosolic NADH-system as disclosed by equilibration with extracellular lactate-pyruvate in hemoglobin-free perfused rat liver. Eur J Biochem *27*, 301–317.

Belousov, V. V., Fradkov, A. F., Lukyanov, K. A., Staroverov, D. B., Shakhbazov, K. S., Terskikh, A. V. and Lukyanov, S. (2006). Genetically encoded fluorescent indicator for intracellular hydrogen peroxide. Nat Methods *3*, 281–286.

Berg, J., Hung, Y. P. and Yellen, G. (2009). A genetically encoded fluorescent reporter of ATP:ADP ratio. Nat Methods *6*, 161–166.

Brekasis, D. and Paget, M. S. B. (2003). A novel sensor of NADH/NAD^+ redox poise in Streptomyces coelicolor A3(2). EMBO J *22*, 4856–4865.

Cerdán, S., Rodrigues, T. B., Sierra, A., Benito, M., Fonseca, L. L., Fonseca, C. P. and García-Martín, M. L. (2006). The redox switch/redox coupling hypothesis. Neurochem Int *48*, 523–530.

Chance, B., Cohen, P., Jobsis, F. and Schoener, B. (1962). Intracellular oxidation-reduction states in vivo. Science *137*, 499–508.

Chen, S., Whetstine, J. R., Ghosh, S., Hanover, J. A., Gali, R. R., Grosu, P. and Shi, Y. (2009). The conserved NAD(H)-dependent corepressor CTBP-1 regulates Caenorhabditis elegans life span. Proc Natl Acad Sci U S A *106*, 1496–1501.

Debnath, J., Muthuswamy, S. K. and Brugge, J. S. (2003). Morphogenesis and oncogenesis of MCF-10A mammary epithelial acini grown in three-dimensional basement membrane cultures. Methods *30*, 256–268.

Dumollard, R., Ward, Z., Carroll, J. and Duchen, M. R. (2007). Regulation of redox metabolism in the mouse oocyte and embryo. Development *134*, 455–465.

Eto, K., Tsubamoto, Y., Terauchi, Y., Sugiyama, T., Kishimoto, T., Takahashi, N., Yamauchi, N., Kubota, N., Murayama, S., Aizawa, T., Akanuma, Y., Aizawa, S., Kasai, H., Yazaki, Y. and Kadowaki, T. (1999). Role of NADH shuttle system in glucose-induced activation of mitochondrial metabolism and insulin secretion. Science *283*, 981–985.

Garriga-Canut, M., Schoenike, B., Qazi, R., Bergendahl, K., Daley, T. J., Pfender, R. M., Morrison, J. F., Ockuly, J., Stafstrom, C., Sutula, T. and Roopra, A. (2006). 2-Deoxy-D-glucose reduces epilepsy progression by NRSF-CtBP-dependent metabolic regulation of chromatin structure. Nat Neurosci *9*, 1382–1387.

Gordon, G. R. J., Choi, H. B., Rungta, R. L., Ellis-Davies, G. C. R. and MacVicar, B. A. (2008). Brain metabolism dictates the polarity of astrocyte control over arterioles. Nature *456*, 745–749.

Griesbeck, O., Baird, G. S., Campbell, R. E., Zacharias, D. A. and Tsien, R. Y. (2001). Reducing the environmental sensitivity of yellow fluorescent proteins. Mechanism and applications. J Biol Chem *276*, 29188–29194.

Herrero-Mendez, A., Almeida, A., Fernández, E., Maestre, C., Moncada, S. and Bolaños, J. P. (2009). The bioenergetic and antioxidant status of neurons is controlled by continuous degradation of a key glycolytic enzyme by APC/C-Cdh1. Nat Cell Biol *11*, 747–752.

Jones, T. R., Kang, I. H., Wheeler, D. B., Lindquist, R. A., Papallo, A., Sabatini, D. M., Golland, P. and Carpenter, A. E. (2008). CellProfiler Analyst: data exploration and analysis software for complex image-based screens. BMC Bioinformatics *15*, 482.

Jörnvall, H., Persson, B., Krook, M., Atrian, S., Gonzàlez-Duarte, R., Jeffery, J. and Ghosh, D. (1995). Short-chain dehydrogenases/reductases (SDR). Biochemistry *34*, 6003–6013.

Kasischke, K. A., Vishwasrao, H. D., Fisher, P. J., Zipfel, W. R. and Webb, W. W. (2004). Neural activity triggers neuronal oxidative metabolism followed by astrocytic glycolysis. Science *305*, 99–103.

Katayama, H., Yamamoto, A., Mizushima, N., Yoshimori, T. and Miyawaki, A. (2008). GFP-like proteins stably accumulate in lysosomes. Cell Struct Funct *33*, 1–12.

Klingenberg, M. and Bücher, T. (1960). Biological oxidations. Annu Rev Biochem *29*, 669–708.

Kumar, V., Carlson, J. E., Ohgi, K. A., Edwards, T. A., Rose, D. W., Escalante, C. R., Rosenfeld, M. G. and Aggarwal, A. K. (2002). Transcription corepressor CtBP is an NAD^+-regulated dehydrogenase. Mol Cell *10*, 857–869.

Lowry, O. H., Roberts, N. R. and Kapphahn, J. I. (1957). The fluorometric measurement of pyridine nucleotides. J Biol Chem *224*, 1047–1064.

Maira, S. M., Stauffer, F., Brueggen, J., Furet, P., Schnell, C., Fritsch, C., Brachmann, S., Chène, P., De Pover, A., Schoemaker, K., Fabbro, D., Gabriel, D., Simonen, M., Murphy, L., Finan, P., Sellers, W. and García-Echeverría, C. (2008). Identification and characterization of NVP-BEZ235, a new orally available dual phosphatidylinositol 3-kinase/mammalian target of rapamycin inhibitor with potent in vivo antitumor activity. Mol Cancer Ther *7*:1851–1863.

Malaisse, W. J. and Sener, A. (1987). Glucose-induced changes in cytosolic ATP content in pancreatic islets. Biochim Biophys Acta *927*, 190–195.

McLaughlin, K. J., Strain-Damerell, C. M., Xie, K., Brekasis, D., Soares, A. S., Paget, M. S. B. and Kielkopf, C. L. (2010). Structural basis for NADH/NAD^+ redox sensing by a Rex family repressor. Mol Cell *38*, 563–575.

Nagai, T., Sawano, A., Park, E. S. and Miyawaki, A. (2001). Circularly permuted green fluorescent proteins engineered to sense Ca^{2+}. Proc Natl Acad Sci U S A *98*, 3197–3202.

Nausch, L. W. M., Ledoux, J., Bonev, A. D., Nelson, M. T. and Dostmann, W. R. (2008). Differential patterning of cGMP in vascular smooth muscle cells revealed by single GFP-linked biosensors. Proc Natl Acad Sci U S A *105*, 365–370.

Ogikubo, S., Nakabayashi, T., Adachi, T., Islam, M. S., Yoshizawa, T., Kinjo, M. and Ohta, N. (2011). Intracellular pH sensing using autofluorescence lifetime microscopy. J Phys Chem B DOI: 10.1021/jp2058904.

Patterson, G. H., Knobel, S. M., Arkhammar, P., Thastrup, O. and Piston, D. W. (2000). Separation of the glucose-stimulated cytoplasmic and mitochondrial NAD(P)H responses in pancreatic islet beta cells. Proc Natl Acad Sci U S A *97*, 5203–5207.

Pellerin, L. and Magistretti, P. J. (1994). Glutamate uptake into astrocytes stimulates aerobic glycolysis: a mechanism coupling neuronal activity to glucose utilization. Proc Natl Acad Sci U S A *91*, 10625–10629.

Rocheleau, J. V., Head, W. S. and Piston, D. W. (2004). Quantitative NAD(P)H/flavoprotein autofluorescence imaging reveals metabolic mechanisms of pancreatic islet pyruvate response. J Biol Chem *279*, 31780–31787.

Schwenke, W. D., Soboll, S., Seitz, H. J. and Sies, H. (1981). Mitochondrial and cytosolic ATP/ADP ratios in rat liver in vivo. Biochem J *200*, 405–408.

Sengupta, S., Peterson, T. R. and Sabatini, D. M. (2010). Regulation of the mTOR complex 1 pathway by nutrients, growth factors, and stress. Mol Cell *40*, 310–322.

Shaner, N. C., Campbell, R. E., Steinbach, P. A., Giepmans, B. N. G., Palmer, A. E. and Tsien, R. Y. (2004). Improved monomeric red, orange and yellow fluorescent proteins derived from Discosoma sp. red fluorescent protein. Nat Biotechnol *22*, 1567–1572.

Shuttleworth, C. W., Brennan, A. M. and Connor, J. A. (2003). NAD(P)H fluorescence imaging of postsynaptic neuronal activation in murine hippocampal slices. J Neurosci *23*, 3196–3208.

Sickmier, E. A., Brekasis, D., Paranawithana, S., Bonanno, J. B., Paget, M. S. B., Burley, S. K. and Kielkopf, C. L. (2005). X-ray structure of a Rex-family repressor/NADH complex insights into the mechanism of redox sensing. Structure *13*, 43–54.

Tantama, M., Hung, Y. P. and Yellen, G. (2011). Imaging intracellular pH in live cells with a genetically encoded red fluorescent protein sensor. J Am Chem Soc *133*, 10034–10037.

Vander Heiden, M. G. V., Cantley, L. C. and Thompson, C. B. (2009). Understanding the Warburg effect: the metabolic requirements of cell proliferation. Science *324*, 1029–1033.

Veech, R. L., Lawson, J. W., Cornell, N. W. and Krebs, H. A. (1979). Cytosolic phosphorylation potential. J Biol Chem *254*, 6538–6547.

Wang, E., Bauer, M. C., Rogstam, A., Linse, S., Logan, D. T. and von Wachenfeldt, C. (2008). Structure and functional properties of the Bacillus subtilis transcriptional repressor Rex. Mol Microbiol *69*, 466–478.

Warburg, O. (1956). On the origin of cancer cells. Science *123*, 309–314.

Williamson, D. H., Lund, P. and Krebs, H. A. (1967). The redox state of free nicotinamide-adenine dinucleotide in the cytoplasm and mitochondria of rat liver. Biochem J *103*, 514–527.

Zapata-Hommer, O. and Griesbeck, O. (2003). Efficiently folding and circularly permuted variants of the Sapphire mutant of GFP. BMC Biotechnol *3*, 5.

Zhang, Q., Piston, D. W. and Goodman, R. H. (2002). Regulation of corepressor function by nuclear NADH. Science *295*, 1895–1897.

Zhang, Q., Wang, S.-Y., Nottke, A. C., Rocheleau, J. V., Piston, D. W. and Goodman, R. H. (2006). Redox sensor CtBP mediates hypoxia-induced tumor cell migration. Proc Natl Acad Sci U S A *103*, 9029–9033.

Chapter III

Single cell oscillations in glycolysis and signal transduction states

Yin Pun Hung [1*], John G. Albeck [2*], Joan S. Brugge [2], and Gary Yellen [1]

[1] Department of Neurobiology and [2] Department of Cell Biology, Harvard Medical School, 220 Longwood Avenue, Boston, Massachusetts 02115, USA

***** Yin Pun Hung and John G. Albeck worked in collaboration to design and implement the experiments. Yin Pun Hung, John G. Albeck, and Gary Yellen analyzed the data presented in this chapter.

ABSTRACT

Cells utilize signaling networks to regulate metabolism, but a quantitative understanding of the relationship between signal transduction and metabolic state remains limited. Using high-content time-lapse microscopy with fluorescent biosensors, we examined the dynamics of glycolysis and signal transduction pathways in individual mammalian cells. Perturbation of growth factor signaling or energetic challenge elicited a dynamic response in glycolysis as indicated by the cytosolic NADH-NAD^+ redox state. Notably, partial glycolytic inhibition by iodoacetate led to sustained, coordinated oscillations in glycolytic NADH-NAD^+ redox, PI3K/Akt pathway activity, and AMPK activity. These single cell oscillations appeared cell-autonomous and persisted for hours, with an approximately half-hour period. In each cycle, an increase in glycolytic NADH coincided with PI3K/Akt activation and AMPK inactivation. These results highlighted a dynamic coupling between signaling pathways and metabolic parameters at the single cell level and should allow us to interrogate the adaptive responses of this metabolic-signaling network to energetic or signaling perturbation.

INTRODUCTION

Cells utilize various signal transduction networks to control metabolic processes. A prominent example in mammalian cells is the regulation of glycolysis, the core pathway of glucose metabolism, by the phosphatidylinositol 3-kinase (PI3K)/Akt and the AMP-dependent protein kinase (AMPK) signaling pathways. As a major component of growth factor signaling, the PI3K/Akt/mTOR pathway activates glycolysis by stimulating glucose uptake and regulatory enzymes such as hexokinase (Plas and Thompson, 2005; Vander Heiden et al., 2009). As a key sensor of cellular energy status, AMPK can activate glycolysis by phosphorylation of multiple phosphofructokinase isoforms, increasing ATP production and thus maintaining energy balance during metabolic stress (Hardie, 2004; Shackelford and Shaw, 2009). Nevertheless, how glycolysis and these signaling pathways are modulated dynamically at the single cell level remains unclear, as both the signal transduction states and metabolic dynamics can vary widely among individual cells, with such cell-to-cell variations masked by bulk biochemical measurements.

By combining high-content microscopy and genetically encoded fluorescent biosensors, we assessed the dynamics of glycolysis and signal transduction pathways at the single cell level. Perturbation of growth factor signaling elicited a dynamic response in the cytosolic NADH-NAD^+ redox state. Moreover, partial glycolytic inhibition triggered sustained, coordinated single-cell oscillations of glycolytic NADH, PI3K/Akt pathway activity, and AMPK activity. In each cycle, stimulation of glycolysis coincided with PI3K/Akt activation (as indicated by a fluorescently-tagged protein domain from FOXO3a) and AMPK inactivation. As these coordinated oscillations could be altered or

abrogated by PI3K/mTOR inhibition, it appeared that growth factor signal transduction was not simply following but rather sustaining the oscillations. These results highlighted a dynamic coupling between glycolytic state and signal transduction at the single cell level and should allow us to interrogate the adaptive responses of this elaborate metabolic-signaling network to energetic or signaling perturbation.

RESULTS

Dynamics of glycolysis upon perturbation of growth factor signaling

We monitored glycolysis by its effect on the cytosolic NADH-NAD^+ redox states in cultured human mammary epithelial MCF-10A cell lines stably expressing nuclear-targeted Peredox-mCherry (Hung et al., 2011). When epidermal growth factor (EGF) and insulin were removed from the culture medium, cytosolic NADH:NAD^+ ratios decreased but promptly recovered within the first 5 hours (Figure 3.1). Upon dual PI3K/mTOR inhibition with BEZ-235 (1 μM; Maira et al., 2008), cytosolic NADH:NAD^+ ratios also decreased but recovered to the initial values after 12 hours. Cytosolic NADH-NAD^+ redox states were unaffected by inhibiting MEK/ERK signaling with PD0325901 (0.5 μM) or EGF signaling with Gefitinib (1 μM), mTORC1 with rapamycin (20 nM), or Akt with inhibitor XIV (10 μM). Dual PI3K/mTOR inhibition appeared to be necessary and sufficient to induce changes, albeit transient, in the cytosolic NADH-NAD^+ redox state. In the case of growth factor withdrawal or dual PI3K/mTOR inhibition, the initial NADH decline was consistent with the expected glycolytic inhibition as a consequence of perturbing growth factor signaling.

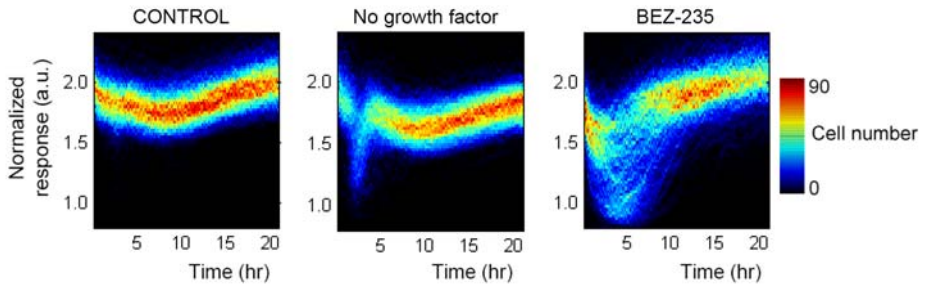

Figure 3.1. Cytosolic NADH-NAD$^+$ redox state of MCF-10A cells under perturbation of growth factor signaling

(A) Heat maps of normalized fluorescence ratios of MCF-10A cells stably expressing Peredox-mCherry-NLS in the control condition, upon removal of growth factor (EGF and insulin), or upon dual PI3K/mTOR inhibition with NVP-BEZ235 (1 μM).

Furthermore, under dual PI3K/mTOR inhibition by BEZ235 (0.2 μM) or AMPK activation by AICAR (1 mM; Henin et al., 1996), cytosolic NADH:NAD$^+$ ratios oscillated in individual cells (Figure 3.2). These oscillations had a period of roughly two to four hours and appeared neither synchronous nor regular within the population. As perturbation to growth factor signaling triggered transient or oscillatory dynamics of the cytosolic NADH-NAD$^+$ redox state, such dynamic response suggested the involvement of negative feedback to maintain glycolysis against perturbations. Although negative feedback typically maintains system stability, it can also underlie oscillatory behaviors in many instances (Hess and Boiteux, 1971; Lahav et al., 2004; Novák and Tyson, 2008).

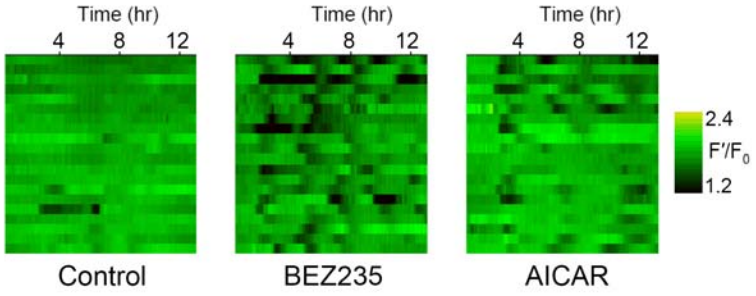

Figure 3.2. Perturbation of PI3K/Akt/mTOR signaling alone induces oscillations in glycolytic NADH

Single cell traces of Peredox NADH signal in MCF-10A cells in the control condition (left), treated with 0.2 μM BEZ-235 (middle), or with 1 mM AICAR (right). *n*=20.

Cytosolic NADH:NAD^+ ratios oscillate in single cells upon partial inhibition of glycolysis

Glycolysis is a negative feedback system, in which its downstream products inhibit the activity of its enzymes and reduce its flux (Figure 3.3A; Hess and Boiteux, 1971). We explored how glycolytic inhibition would affect the dynamics of cytosolic NADH-NAD^+ redox state and related signaling pathways. Inhibition of glycolysis by iodoacetate (IAA; >100 μM) promptly decreased cytosolic NADH:NAD^+ ratios in all cells as expected. However, upon partial inhibition by a lower concentration of IAA (10 μM), cytosolic NADH:NAD^+ ratios oscillated in individual cells (Figure 3.3B). These oscillations appeared undamped and persisted for >12 hours, with a somewhat regular, approximately half-hour period. Cytosolic NADH:NAD^+ ratios as determined by the sensor response oscillated by more than 10-fold in these cells. A majority of cells (~90%) displayed NADH oscillations, which were not synchronous and collectively led to a smear in the ensemble heat map. The asynchronous nature of these individual oscillations argued against their origin from imaging artifacts or environmental fluctuations.

Indeed, the oscillations were of cytosolic NADH:NAD^+ ratios, as supported by the following lines of evidence: First, they became less pronounced in the presence of lactate or pyruvate, which shifted the cytosolic NADH-NAD^+ redox state via the lactate dehydrogenase (LDH) reaction (Figure 3.3C); also, the IAA-induced oscillations exhibited a shorter period in the presence of an LDH inhibitor oxamate (2 mM). Second, the oscillations were not seen using a control reporter Y98D, which contained mutations to abrogate its binding to NADH. Third, the oscillations were dependent on the presence of glucose, signifying that they were of glycolytic origin (Figure 3.3D). Finally, they

were dependent on the concentration of IAA. The minimal concentration of IAA needed to elicit glycolytic NADH oscillations was around 10 μM, with an abrupt transition from stationary to oscillatory behaviors (Figure 3.3E).

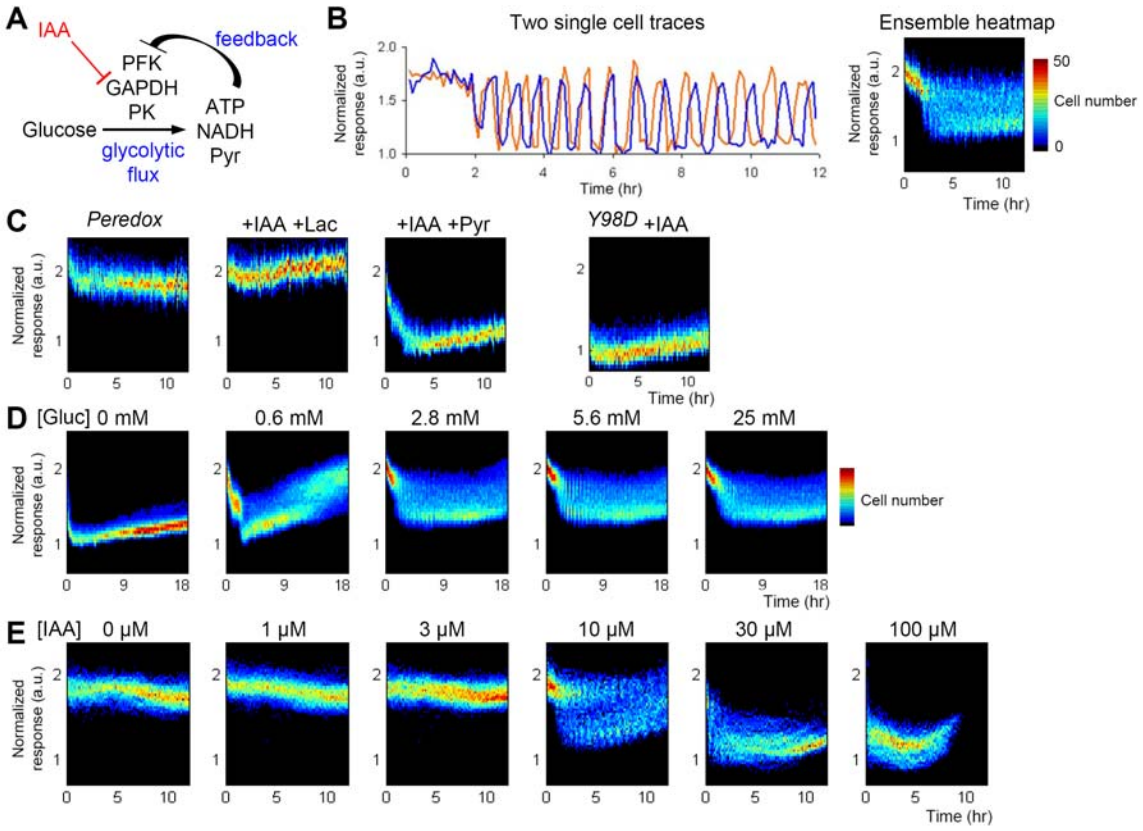

Figure 3.3. Cytosolic NADH:NAD$^+$ ratios oscillate in single cells upon partial inhibition of glycolysis

(A) Glycolysis is a negative feedback system, in which its downstream products inhibit the activity of its enzymes and reduce its flux. (B) Peredox response of MCF-10A cells under partial inhibition of glycolysis by 10 μM iodoacetate (IAA), the time course of two cells (left) and the ensemble heat map of the population (right). (C) Peredox response heat maps of cells in the control condition, treated with 10 μM IAA plus 10 mM lactate, or 10 μM IAA plus 10 mM pyruvate, and the heat map of the control Y98D reporter in cells with 10 μM IAA. (D) Peredox response heat maps of cells treated with 10 μM IAA in the presence of various concentrations of glucose. (E) Peredox response heat maps of cells treated with various concentrations of IAA.

This nonlinearity was reminiscent of the sharp dependence on the glucose flow rate to induce metabolic oscillations in a bio-reactor of yeast cell suspensions (Danø et al.,

1999), and it could be described mathematically by the Hopf bifurcation in the framework of dynamical systems (Danø et al., 1999; Chandra et al., 2011). In addition to sustained application, brief IAA treatment of 15−30 minutes also elicited NADH oscillations with similar characteristics. No oscillations were observed with application of 2-deoxyglucose or glucose withdrawal alone, and this may reflect distinct modes and severities of glycolytic inhibition from these treatments.

Oscillations in PI3K/Akt and AMPK pathway activity in single cells upon partial inhibition of glycolysis

As PI3K/Akt and AMPK signaling pathways are key regulators of glycolysis, we investigated if they participate in the glycolytic NADH oscillations. To assess the PI3K/Akt pathway activity in single cells, we utilized a fluorescent protein tagged N-terminal domain of FOXO3a (with a mutated DNA binding domain and deleted transactivation domain; Tran et al., 2002). Akt phosphorylates the Forkhead transcription factor FOXO3a to promote its cytoplasmic retention; with low Akt activity, the dephosphorylated FOXO3a translocates to the nucleus (Brunet et al., 1999). Upon glycolytic inhibition by IAA, FOXO3a-YFP cycled back and forth between the cytosol and the nucleus (Figure 3.4A), indicating that the PI3K/Akt pathway was oscillating between high and low activity states. When we examined the AMPK pathway activity using the FRET biosensor AMPKAR (Tsou et al., 2011), we observed IAA-induced oscillations in the cytosolic YFP:CFP ratios but fairly constant nuclear YFP:CFP ratios (Figure 3.4B). Thus, cytosolic but not nuclear AMPK was also oscillating between high and low activity states upon partial glycolytic inhibition; notably, AMPK activation

confined to the cytosol had been observed in cells under energy stress from metabolic inhibition (Tsou et al., 2011). While no oscillations were seen in the control condition, partial glycolytic inhibition led to oscillations in both the PI3K/Akt and AMPK pathway activity, with a roughly half-hour period similar to that of glycolytic NADH oscillations.

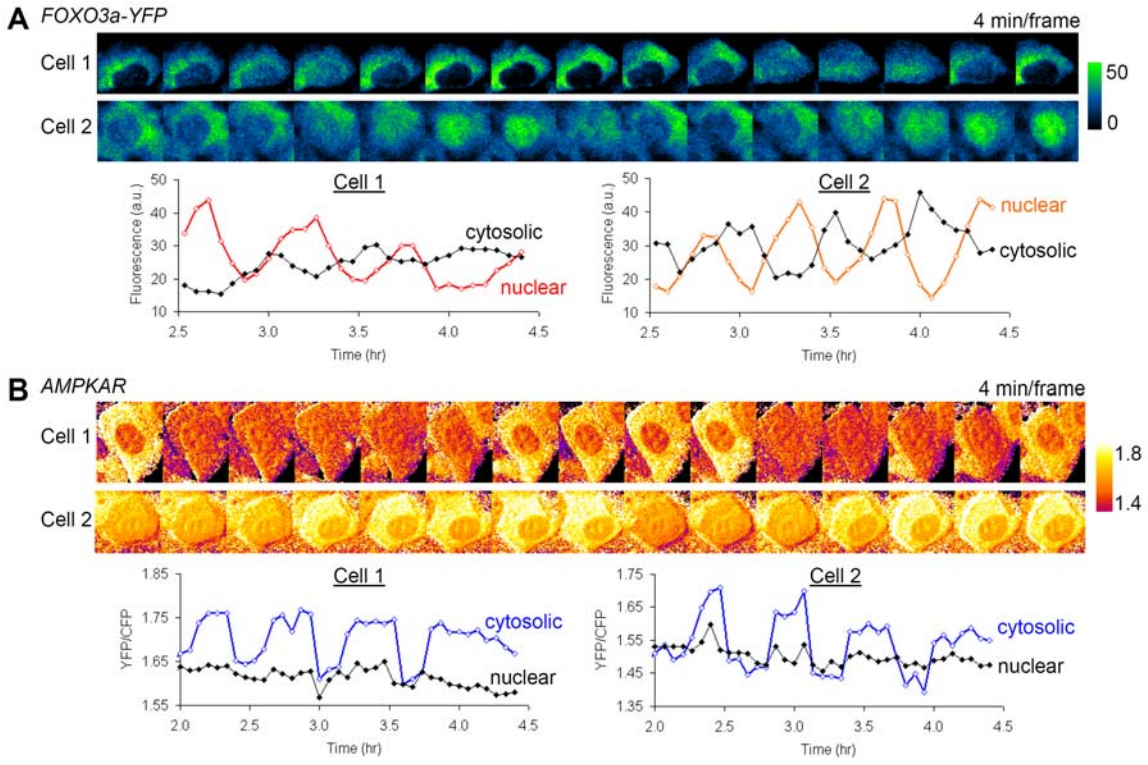

Figure 3.4. Oscillations in FOXO3a nucleocytoplasmic shuttling and AMPK activity in single cells upon partial inhibition of glycolysis

(A) Pseudocolored time-lapse images (top) and time courses (bottom) of FOXO3a-YFP fluorscence in two MCF-10A cells treated with 10 μM IAA. (B) Pseudocolored time-lapse images (top) and time courses (bottom) of AMPKAR YFP:CFP ratios in two cells treated with 10 μM IAA. Images were acquired every 4 minutes. Time courses showed signals from both cytosolic and nuclear regions.

Coordinated single cell oscillations in glycolytic NADH, PI3K/Akt activation, and AMPK activity

After observing similar oscillations in glycolysis and signal transduction states, we proceeded to determine whether they are interrelated and, if so, their relative phase relationships. To assess the PI3K/Akt pathway activity with concurrent readouts of NADH or AMPK, we generated MCF-10A cell lines stably expressing FOXO3a-RFP together with Peredox-mCitrine or AMPKAR (Figures 3.5A and 3.5B). Since nuclear FOXO level decreases upon Akt activation, the inverted nuclear FOXO3a signal was used as an indicator of the PI3K/Akt pathway activity and plotted alongside the NADH or AMPK biosensor signal (Figure 3.5C).

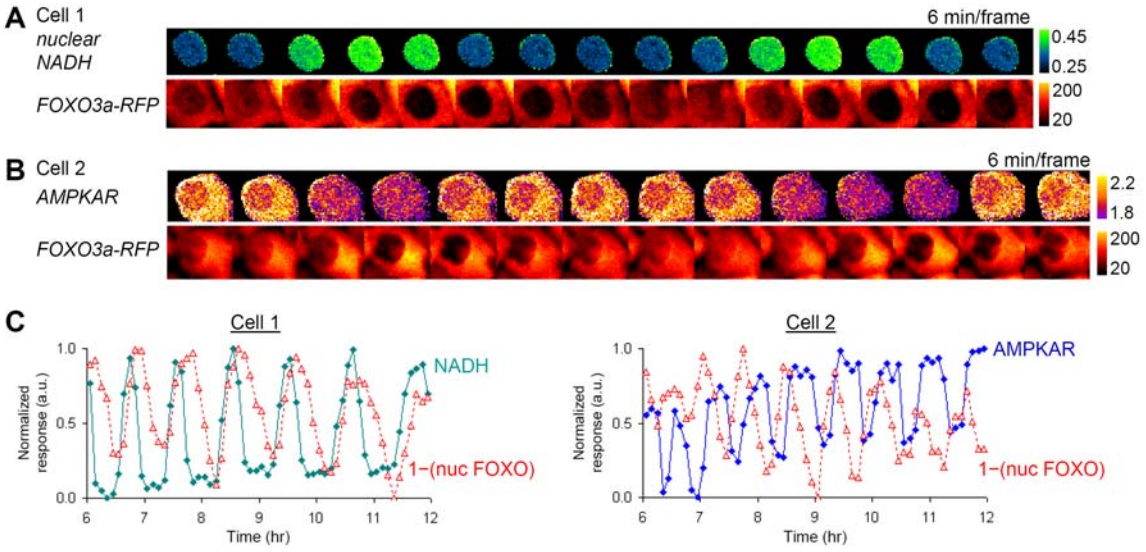

Figure 3.5. Coordinated single cell oscillations in glycolytic NADH, FOXO3a nucleocytoplasmic shuttling, and AMPK activity upon partial inhibition of glycolysis

Pseudocolored time-lapse images of single MCF-10A cells, expressing (A) Peredox-mCitrine and FOXO3a-RFP or (B) AMPKAR and FOXO3a-RFP, during partial inhibition of glycolysis by 10 μM IAA. Images were acquired every 6 minutes. (C) Time courses of the inverted nuclear FOXO3a signal (red), along with NADH signal (green) or cytosolic AMPKAR signal (blue).

During partial inhibition of glycolysis, the single cell oscillations in cytosolic NADH, PI3K/Akt activation, and AMPK activity were temporally coordinated: In each cycle, PI3K/Akt activation appeared to coincide with an increase in glycolytic NADH level (Figures 3.5A and 3.5C). The several-minute delay of nuclear FOXO3a-RFP disappearance as compared with NADH increase may reflect differential sensitivity of these two readouts to Akt activation: additional time may be required for activated Akt to induce FOXO3a cytoplasmic retention as compared with glycolytic activation. In addition, PI3K/Akt activation coincided with AMPK inactivation and vice versa in each cycle, revealing a coordination of these signaling pathways (Figures 3.5B and 3.5C).

Consistent with the microscopy data, the NADH biosensor measurements also correlated with the immunofluorescence of phosphorylated Akt, phosphorylated S6 kinase (S6K), and FOXO in individual cells at single time points during the oscillations. Furthermore, upon application of Akt inhibitor XIV (10 μM) or dual PI3K/mTOR inhibitor BEZ-235 (1 μM), the NADH oscillations decreased in frequency or disappeared altogether (Figure 3.6A). While many cells treated with Akt inhibitor XIV continued to exhibit NADH oscillations, albeit of a longer period, continued oscillations in FOXO3a nucleocytoplasmic shuttling indicated an incomplete pharmacological inhibition of the PI3K/Akt pathway (Figure 3.6B). Under dual PI3K/mTOR inhibition, most cells did not show IAA-induced oscillations in both NADH and FOXO3a signals, and the remaining few cells that showed NADH oscillations also displayed FOXO3a oscillations. Therefore, the PI3K/Akt/mTOR signaling pathway was not simply following but rather sustaining the NADH oscillations.

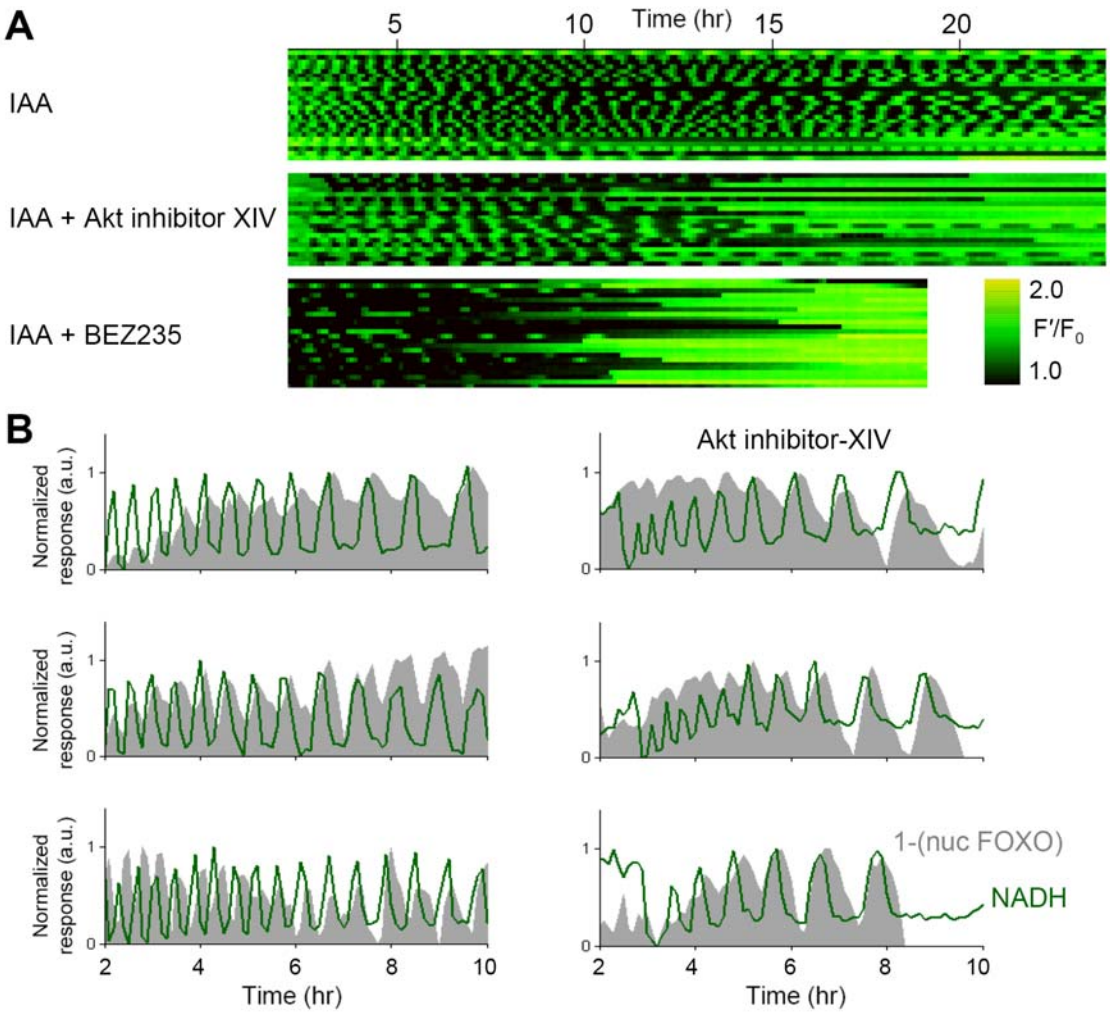

Figure 3.6. Perturbation of PI3K/Akt/mTOR signaling alters the IAA-induced oscillations in glycolytic NADH and FOXO3a nucleocytoplasmic shuttling

(A) Single cell traces of NADH signal in MCF-10A cells treated with 10 μM IAA alone (top; *n*=24), IAA plus 10 μM Akt inhibitor XIV (middle; *n*=20), or IAA plus 1 μM BEZ-235 (bottom; *n*=24). (B) Normalized time course of the inverted nuclear FOXO3a signal (grey area plot) with the NADH signal (green) for three individual cells treated with 10 μM IAA alone (left) or IAA plus 10 μM Akt inhibitor XIV (right).

DISCUSSION

Using live-cell measurements with genetically encoded fluorescent biosensors, we assessed the dynamics of signal transduction states and glycolysis during acute perturbation of growth factor signaling or energetic challenge. Dual PI3K/mTOR inhibition by BEZ235, AMPK activation by AICAR, or glycolytic inhibition by iodoacetate triggered single cell oscillations in glycolysis as indicated by the cytosolic NADH:NAD^+ ratios. Compared with oscillations induced by BEZ235 or AICAR, the IAA-induced NADH oscillations appeared more regular with a shorter, roughly half-hour period. The oscillations appeared cell-autonomous and persisted for hours. Such oscillatory dynamics signified the presence of negative feedback to maintain system stability under energetic or signaling crisis. Furthermore, during partial glycolytic inhibition, we observed coordinated oscillations in glycolysis, PI3K/Akt pathway activity, and AMPK activity. In each cycle, stimulation of glycolysis coincided with PI3K/Akt activation (as indicated by a fluorescently-tagged protein domain from FOXO3a) and AMPK inactivation (Figure 3.7A), revealing a dynamic relationship between signal transduction states and glycolysis in individual live cells.

Compared with published studies on metabolic oscillations, this work differs in the following aspects: First, most studies presumably detect oscillations in mitochondrial metabolism rather than genuine oscillations in glycolysis, as they rely on mitochondrial inhibitors such as cyanide for oscillation induction and measure NAD(P)H autofluorescence as readouts (Romashko et al., 1998; Aon et al., 2003). Second, most studies primarily focus on yeast suspensions or extracts (Chance et al., 1964; Danø et al., 1999; Chandra et al., 2011); studies in mammalian cells are limited but have been

conducted in muscle cells, pancreatic β-cells, and cardiomyocytes (Tornheim and Lowenstein, 1973; Chou et al., 1992; O'Rourke et al., 1994; Yang et al., 2008). Third, most previous studies show an oscillation period of seconds, whereas the period in our glycolytic and signaling oscillations is much longer, in the range of half-hour to hours.

We explore how glycolytic oscillations are coordinated with related signal transduction states, as well as whether this metabolic-signaling network modulates the oscillatory dynamics. Negative feedback networks, with delay or signal amplification, often underlie oscillatory behaviors in biological systems (Lahav et al., 2004; Novák and Tyson, 2008). To account for oscillatory dynamics of glycolysis, several computational models have been constructed based on the negative feedback of glycolytic products on the main regulatory enzyme phosphofructokinase. Here, we propose that glycolytic and signaling oscillations in mammalian cells are sustained by a larger negative feedback network involving glycolysis and the signal transduction pathways (Figure 3.7B). PI3K/Akt activation triggers glycolysis and exerts negative feedback on AMPK activity through generation of metabolites such as ATP; AMPK inactivation leads to derepression of mTORC1/S6K and suppression of PI3K/Akt activity, thus constituting a negative feedback system of this metabolic-signaling network (Plas and Thompson, 2005; Manning and Cantley, 2007; Guertin and Sabatini, 2009). Our preliminary data on immunofluorescence of phosphorylated S6K appeared to corroborate this model. The induction of glycolytic oscillations by BEZ235, IAA, or AICAR presumably relate to the weakening of mTORC1/S6K activity and of its suppression on the PI3K/Akt activity. This may render the PI3K/Akt pathway more reliant on nutrient-dependent feedback regulation and prone to oscillations (Plas and Thompson, 2005).

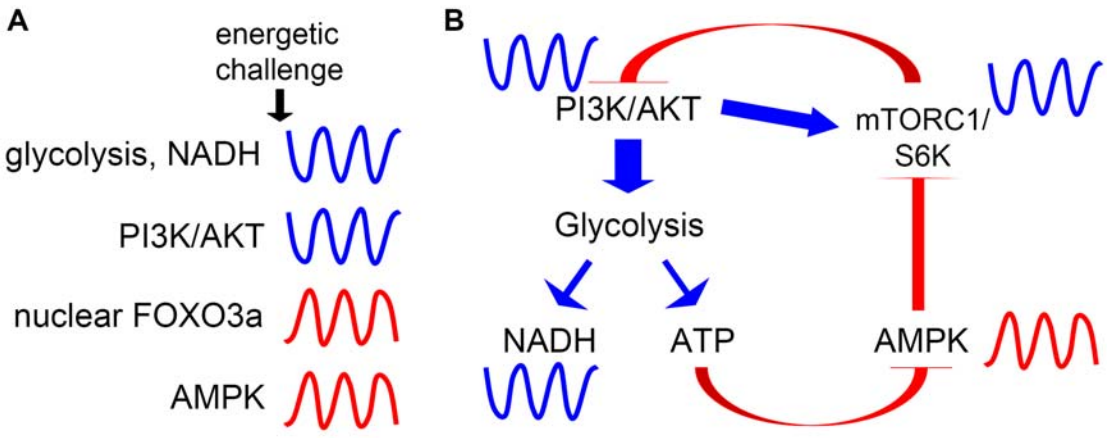

Figure 3.7. Summary and proposed model of the single cell oscillations in glycolysis, the PI3K/Akt pathway activity, and the AMPK activity.

(A) Data summary: Upon energetic challenge, the metabolic-signaling network undergoes coordinated oscillations, with glycolysis concurrent with PI3K/Akt activation and AMPK inactivation. (B) Proposed model: PI3K/Akt pathway activates glycolysis and generation of ATP that exerts negative feedback on AMPK activity; AMPK inactivation leads to derepression of mTORC1/S6K and suppression of PI3K/Akt activity, thus constituting a negative feedback system.

This work highlighted a dynamic coupling between signal transduction and metabolic parameters at the single cell level and may allow us to dissect further the mechanistic basis of metabolic dysregulation. While alteration of cell metabolism and signaling networks are common in many diseases, the dynamic adaptive response of this metabolic-signaling network may pose challenges on creating effective pharmacotherapy. In addition, under the framework of control theory, glycolytic oscillations have been shown to be an inevitable trade-off to optimize robustness and efficiency (Chandra et al., 2011). This begets the question of whether the related signaling pathways could be subject to similar trade-offs between robustness and efficiency. The oscillatory dynamics of glycolysis and signal transduction states may shed light on the general design principles of this elaborate metabolic-signaling network.

EXPERIMENTAL PROCEDURES

Gene construction and materials

Peredox-mCitrine-NLS was generated by replacing mCherry with mCitrine (Shaner et al., 2005) in pMSCV-Peredox-mCherry-NLS (Hung et al., 2011). AMPKAR (Tsou et al., 2011; in a lentiviral vector with a pHR backbone and a CMV promoter) was provided by P. Tsou and L. Cantley. For FOXO3a-YFP or -RFP, the N-terminal domain (amino acid residues 1−400) of human FOXO3a DNA binding mutant H212R (Tran et al., 2002; from Addgene) was subcloned into a pMSCV vector with a C-terminal mVenus or mCherry (Shaner et al., 2005). Reagents were from Sigma unless noted. The following compounds were used: Akt inhibitor XIV (Calbiochem), BEZ-235 (Axon Medchem), Gefitinib (Axon Medchem), PD0325901 (Calbiochem), rapamycin (Calbiochem), and Torin-1 (N. Gray). The following antibodies were used: antibodies against pAkt-S^{473} (Cell Signaling), FoxO3a (Cell Signaling), pS6-$S^{235}S^{236}$ (Cell Signaling), and pS6-$S^{240}S^{244}$ (Cell Signaling), and Alexa Fluor 488, 555, and 647 (Invitrogen).

Cell Culture

Human mammary epithelial MCF-10A cells (CRL-10317, ATCC) and the clonal derivative 5E (Janes et al., 2010) were maintained in 95% air and 5% CO_2 at 37°C and cultured as previously described (Debnath et al., 2003) in the MCF-10A growth medium: Dulbecco's modified Eagle's medium (DMEM)/F-12 (Invitrogen), supplemented with 5% horse serum (Invitrogen), epidermal growth factor (EGF; 20 ng/ml; Peprotech), insulin (10 μg/ml), hydrocortisone (0.5 μg/ml), cholera toxin (100 ng/ml), penicillin and streptomycin (both 50 μg/ml; Invitrogen). For biosensor expression, cells were infected

with the retroviral or lentiviral vectors, followed by puromycin (2 μg/ml) selection and expansion of single clones.

Fluorescence microscopy

About 500−2000 cells were plated onto the center of each well of a 24-well (MatTek) or 96-well glass-bottom plate (Matrical) 2−4 days prior. Cells were imaged in the phenol red-free RPMI (Invitrogen), supplemented with 0.3% bovine serum albumin, EGF, insulin, hydrocortisone, cholera toxin, and pen-strep, at 37°C and 5% CO_2. Experimental treatments with varying glucose concentration were prepared in custom DMEM/F12 media, supplemented with dialyzed horse serum, EGF, insulin, hydrocortisone, cholera toxin, and pen-strep. Wide-field images were acquired using a Nikon inverted Eclipse Ti microscope, equipped with a Nikon 20×/0.75 Plan Apo objective and Chroma filter cubes for the following: T-Sapphire (ET405/20x, T425LPXR, and ET525/50m), CFP (31044v2), YFP (41028), and RFP (41043). Images were collected every 4−6 min with an exposure time of 40−400 ms and 2×2 binning. Fluorescence response heat maps were generated in MATLAB (MathWorks) using custom programs based on CellProfiler (Jones et al., 2008), which subtracted background, set threshold and cell segmentation, and generated a green to red ratio for each cell at each time point. Single cell traces were generated by manual tracking in ImageJ (http://rsb.info.nih.gov/ij/) with custom plugins or by automated tracking using custom MATLAB program with DCellIQ (Li et al., 2010). Cell traces from automated tracking were validated manually, and dividing cells were excluded from data analysis.

ACKNOWLEDGMENTS

We thank the Nikon Imaging Center at Harvard Medical School for help with microscopy; J. Locasale for providing media and support; D. Clapham, T. Schwarz, and members of the Brugge lab and the Yellen lab for their comments. This work was supported by a Stuart H. Q. and Victoria Quan predoctoral fellowship (to Y.P.H.), a U.S. Army Breast Cancer Research Program multidisciplinary postdoctoral fellowship (W81XWH-08-1-0609 to J.G.A.), and the US National Institutes of Health (R01 NS055031 to G.Y.).

REFERENCES

Aon, M. A., Cortassa, S., Marbán, E. and O'Rourke, B. (2003). Synchronized whole cell oscillations in mitochondrial metabolism triggered by a local release of reactive oxygen species in cardiac myocytes. J Biol Chem *278*, 44735–44744.

Brunet, A., Bonni, A., Zigmond, M. J., Lin, M. Z., Juo, P., Hu, L. S., Anderson, M. J., Arden, K. C., Blenis, J. and Greenberg, M. E. (1999). Akt promotes cell survival by phosphorylating and inhibiting a Forkhead transcription factor. Cell *96*, 857–868.

Chance, B., Estabrook, R. W. and Ghosh, A. (1964). Damped sinusoidal oscillations of cytoplasmic reduced pyridine nucleotide in yeast cells. Proc Natl Acad Sci U S A *51*, 1244–1251.

Chandra, F. A., Buzi, G. and Doyle, J. C. (2011). Glycolytic oscillations and limits on robust efficiency. Science *333*, 187–192.

Chou, H. F., Berman, N. and Ipp, E. (1992). Oscillations of lactate released from islets of Langerhans: evidence for oscillatory glycolysis in beta-cells. Am J Physiol *262*, E800–E805.

Danø, S., Sørensen, P. G. and Hynne, F. (1999). Sustained oscillations in living cells. Nature *402*, 320–322.

Debnath, J., Muthuswamy, S. K. and Brugge, J. S. (2003). Morphogenesis and oncogenesis of MCF-10A mammary epithelial acini grown in three-dimensional basement membrane cultures. Methods *30*, 256–268.

Guertin, D. A. and Sabatini, D. M. (2009). The pharmacology of mTOR inhibition. Sci Signal *2*, pe24.

Hardie, D. G. (2004). The AMP-activated protein kinase pathway–new players upstream and downstream. J Cell Sci *117*, 5479–5487.

Henin, N., Vincent, M. F. and den Berghe, G. V. (1996). Stimulation of rat liver AMP-activated protein kinase by AMP analogues. Biochim Biophys Acta *1290*, 197–203.

Hess, B. and Boiteux, A. (1971). Oscillatory phenomena in biochemistry. Annu Rev Biochem *40*, 237–258.

Hung, Y. P., Albeck, J. G., Tantama, M. and Yellen, G. (2011). Imaging cytosolic NADH-NAD^+ redox state with a genetically encoded fluorescent biosensor. Cell Metab *14*, 545–554.

Janes, K. A., Wang, C.-C., Holmberg, K. J., Cabral, K. and Brugge, J. S. (2010). Identifying single-cell molecular programs by stochastic profiling. Nat Methods *7*, 311–317.

Jones, T. R., Kang, I. H., Wheeler, D. B., Lindquist, R. A., Papallo, A., Sabatini, D. M., Golland, P. and Carpenter, A. E. (2008). CellProfiler Analyst: data exploration and analysis software for complex image-based screens. BMC Bioinformatics *9*, 482.

Lahav, G., Rosenfeld, N., Sigal, A., Geva-Zatorsky, N., Levine, A. J., Elowitz, M. B. and Alon, U. (2004). Dynamics of the p53-Mdm2 feedback loop in individual cells. Nat Genet *36*, 147–150.

Li, F., Zhou, X., Ma, J. and Wong, S. T. C. (2010). Multiple nuclei tracking using integer programming for quantitative cancer cell cycle analysis. IEEE Trans Med Imaging *29*, 96–105.

Maira, S.-M., Stauffer, F., Brueggen, J., Furet, P., Schnell, C., Fritsch, C., Brachmann, S., Chène, P., Pover, A. D., Schoemaker, K., Fabbro, D., Gabriel, D., Simonen, M., Murphy, L., Finan, P., Sellers, W. and García-Echeverría, C. (2008). Identification and characterization of NVP-BEZ235, a new orally available dual phosphatidylinositol 3-kinase/mammalian target of rapamycin inhibitor with potent in vivo antitumor activity. Mol Cancer Ther *7*, 1851–1863.

Manning, B. D. and Cantley, L. C. (2007). AKT/PKB signaling: navigating downstream. Cell *129*, 1261–1274.

Novák, B. and Tyson, J. J. (2008). Design principles of biochemical oscillators. Nat Rev Mol Cell Biol *9*, 981–991.

O'Rourke, B., Ramza, B. M. and Marban, E. (1994). Oscillations of membrane current and excitability driven by metabolic oscillations in heart cells. Science *265*, 962–966.

Plas, D. R. and Thompson, C. B. (2005). Akt-dependent transformation: there is more to growth than just surviving. Oncogene *24*, 7435–7442.

Romashko, D. N., Marban, E. and O'Rourke, B. (1998). Subcellular metabolic transients and mitochondrial redox waves in heart cells. Proc Natl Acad Sci U S A *95*, 1618–1623.

Shackelford, D. B. and Shaw, R. J. (2009). The LKB1-AMPK pathway: metabolism and growth control in tumour suppression. Nat Rev Cancer *9*, 563–575.

Shaner, N. C., Steinbach, P. A. and Tsien, R. Y. (2005). A guide to choosing fluorescent proteins. Nat Methods *2*, 905–909.

Tornheim, K. and Lowenstein, J. M. (1973). The purine nucleotide cycle. 3. Oscillations in metabolite concentrations during the operation of the cycle in muscle extracts. J Biol Chem *248*, 2670–2677.

Tran, H., Brunet, A., Grenier, J. M., Datta, S. R., Fornace, A. J., DiStefano, P. S., Chiang, L. W. and Greenberg, M. E. (2002). DNA repair pathway stimulated by the forkhead transcription factor FOXO3a through the Gadd45 protein. Science *296*, 530–534.

Tsou, P., Zheng, B., Hsu, C.-H., Sasaki, A. T. and Cantley, L. C. (2011). A fluorescent reporter of AMPK activity and cellular energy stress. Cell Metab *13*, 476–486.

Vander Heiden, M. G., Cantley, L. C. and Thompson, C. B. (2009). Understanding the Warburg effect: the metabolic requirements of cell proliferation. Science *324*, 1029–1033.

Yang, J.-H., Yang, L., Qu, Z. and Weiss, J. N. (2008). Glycolytic oscillations in isolated rabbit ventricular myocytes. J Biol Chem *283*, 36321–36327.

Chapter IV

Discussion

Yin Pun Hung contributed all figures in this chapter and worked with John G. Albeck on Figures 4.3, 4.4, and 4.5.

DESIGN OF ADDITIONAL SENSORS RELATED TO NADH

In Chapter II, we have established that Peredox reports the cytosolic NADH-NAD^+ redox state in single individual mammalian cells. Beyond sensing cytosolic NADH-NAD^+ redox state, Peredox could be a starting point to engineer biosensors for other metabolic parameters related to NADH metabolism, such as mitochondrial NADH:NAD^+ ratio, NAD^+ pool size, cytosolic NADPH:$NADP^+$ ratio, and NADPH pool size.

Mitochondrial NADH:NAD^+ ratio sensor

In contrast with the endogenous NAD(P)H autofluorescence, a mitochondrial NADH:NAD^+ ratio biosensor would specifically report the free pool rather than the protein-bound pool of mitochondrial NADH. For mitochondrial NADH-NAD^+ redox sensing, the current version of Peredox would not be expected to work. In mammalian cells, the NADH:NAD^+ ratio has been estimated to be 100- to 1000-fold higher in the mitochondria than in the cytosol (Williamson et al., 1967). Therefore, the affinity of Peredox for NAD^+ relative to NADH would need improvement by a similar factor in order to report mitochondrial NADH:NAD^+ ratio. With targeted mutagenesis near the NADH binding pocket of Peredox, we generated variants, MitoV1 and MitoV2, with NADH:NAD^+ ratio sensing shifted by about 8-fold (Figure 4.1).

The mitochondrial environment, with potential abundance of reactive oxygen species and a more alkaline pH (Nicholls and Ferguson, 2002), could prove challenging for designing GFP-based biosensors. For instance, as it has been reported that cpYFP alone is sensitive to superoxide (Wang et al,. 2008), other fluorescent sensors using

cpYFP can be susceptible to artifacts from ROS. Compared with other cpFPs, circularly permuted T-Sapphire contains one fewer cysteine (Zapata-Hommer and Griesbeck, 2003) and would be expected to be resistant to superoxide and other redox agents. More importantly, unlike many other cpFPs, circularly permuted T-Sapphire and the resulting NADH sensor Peredox appear notably resistant to pH changes in the physiological range (Hung et al., 2011). Future efforts to expand the mutagenesis process may yield a sensor appropriate for detecting changes in the mitochondrial NADH:NAD^+ ratio.

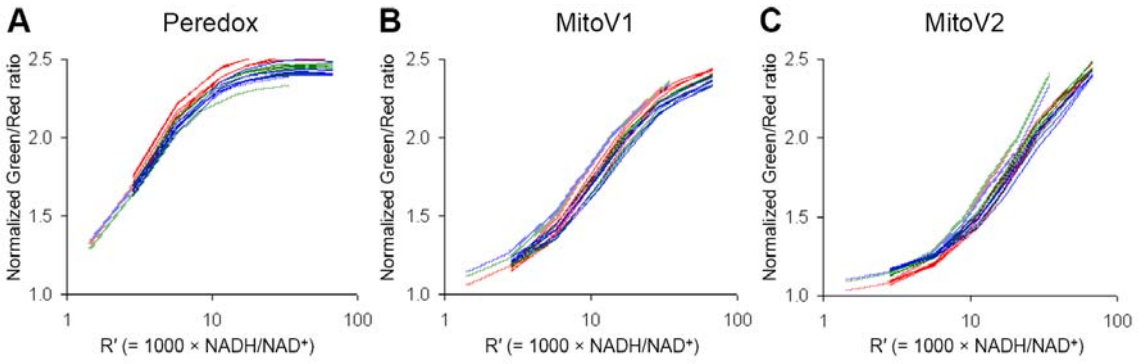

Figure 4.1. Comparison among Peredox and two variants, MitoV1 and MitoV2, for sensing higher NADH:NAD^+ ratios

Green to red fluorescence ratios plotted against R' (= 1000 × [NADH] / [NAD^+]) in Peredox (A) and sensor variants with additional mutations: (B) MitoV1 (Ile189Phe in the first subunit and Arg90Asn and Val122Ala in the second subunit) and (C) MitoV2 (Ile189Phe in the first subunit and Arg90Gln in the second subunit). NADH titrations were at room temperature in the presence of NAD^+ (0.3 mM, dotted line; 0.6, solid line) and ADP/ATP (0 mM, dotted line; 1 mM, solid line; 4 mM, thick solid line, with 0.3 mM NAD^+) at the indicated pH (7.2, red; 7.6, green; 8.0, blue). Fluorescence ratios were normalized to the control condition in the absence of pyridine nucleotides at pH 7.2.

NAD pool sensor

Considering the diverse regulatory roles of NAD^+ in DNA repair (Durkacz et al., 1980), aging (Imai et al., 2000), and circadian rhythms (Nakahata et al., 2009; Ramsey et al., 2009), it would be valuable to monitor the dynamics of the cellular NAD^+ pool using a GFP-based biosensor. A major challenge to create such NAD^+ sensor from Peredox is that, currently, its conformational open-to-closed transition takes place upon binding to NADH and not NAD^+. Mutagenesis in the binding pocket, particularly the residues near the nicotinamide moiety of NADH, may swap the preference for reduced versus oxidized species to yield a biosensor of NAD^+.

$NADPH:NADP^+$ ratio and NADPH pool sensors

In view of the importance of NADPH-$NADP^+$ redox in glutathione regeneration and biosynthesis of macromolecules (Pollak et al., 2007), it would be valuable to engineer a fluorescent biosensor of NADPH-$NADP^+$ redox. However, to do so using Peredox as a scaffold, we would need to accomplish the two following steps:

First, the specificity of Peredox for NADH over NADPH needs to be altered. Structurally almost identical, NADH and NADPH differ only at the adenosine 2′ position. In the structure of T-Rex (Sickmier et al., 2005), the residues Asp112 and Asp114 interact with the adenosine 2′ hydroxyl group to discriminate NADH from NADPH (Figure 4.2A). Focused mutagenesis at these and nearby residues could dramatically disfavor NADH binding and favor NADPH binding. Indeed, using site directed mutagenesis based on Peredox, we generated NADPH sensor #1, which was specific for NADPH rather than NADH (Figures 4.2B and 4.2C), with a dissociation constant for

NADPH at ~1 μM. NADPH sensor #1 was sensitive to physiological concentrations of ATP and ADP, which could shift its NADPH binding affinity by about 2-fold. Compared with NADPH sensor #1, the problem of ATP/ADP interference is less severe in Peredox, as the presence of physiological concentrations of NAD^+ reduced the interference of ATP or ADP on NADH sensing (Hung et al., 2011).

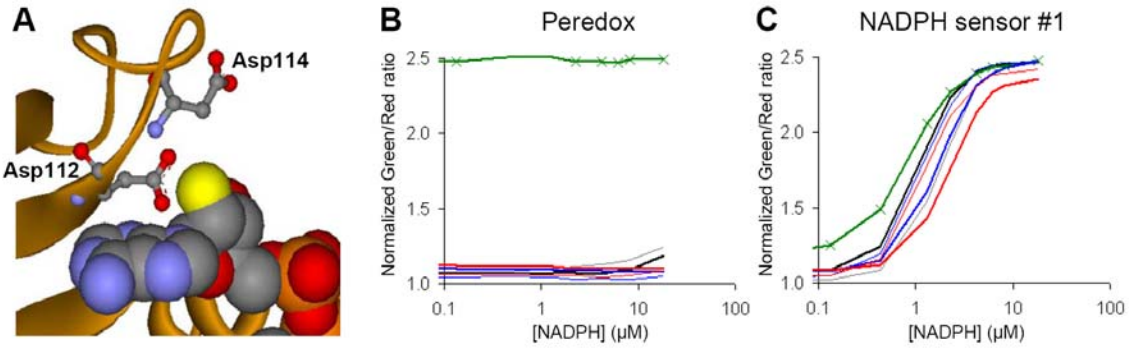

Figure 4.2. Comparison between Peredox and a variant for NADPH sensing

(A) Close-up view of the NADH binding site in T-Rex (PDB: 1xcb). The two residues Asp112 and Asp114 (balls and sticks) interact with the adenosine 2′ hydroxyl group (yellow) of NADH. (B) Green to red fluorescence ratios plotted against NADPH concentration in Peredox. (C) Green to red fluorescence ratios plotted against NADPH concentration in NADPH sensor #1, which contains the following mutations: Ile189Phe in the first subunit of Rex, as well as Asp112Thr, Val113Arg, and Asp114Thr in both Rex subunits. NADPH titrations were at room temperature at pH 7.3 (black), in the presence of NADH (10 μM; green), $NADP^+$ (100 μM; gray), ADP (1 mM and 4 mM; thin and thick blue lines), or ATP (1 mM and 4 mM; thin and thick red lines). Fluorescence ratios were normalized to the control condition in the absence of pyridine nucleotides at pH 7.3.

Second, to make a sensor of NADPH-$NADP^+$ redox, we would need to alter the sensor specificity for reduced versus oxidized nucleotides. In the cytosolic environment in mammalian cells, while NADH is in the minority for the NADH-NAD^+ redox couple, NADPH is the prevailing form in the NADPH-$NADP^+$ redox couple (Veech et al., 1969; Hedeskov et al., 1987). Changes in NADPH-$NADP^+$ redox owing to the interconversion

of the two species are presumably due to changes in the concentration of $NADP^+$ rather than NADPH. The sensor preference for reduced versus oxidized species thus would need to be altered, so that it could report $NADP^+$ instead of NADPH. Hence, NADPH sensor #1 strictly reports the NADPH pool size, not changes in the NADPH-$NADP^+$ redox state.

Nonetheless, we examined whether NADPH sensor #1 could detect changes in the cytosolic NADPH pool size in individual live cells. We generated MCF-10A cell lines stably expressing NADPH sensor #1. Cell lines expressing Peredox or the control Y98D reporter, which could bind neither NADH nor NADPH, were used as experimental controls (Figure 4.3).

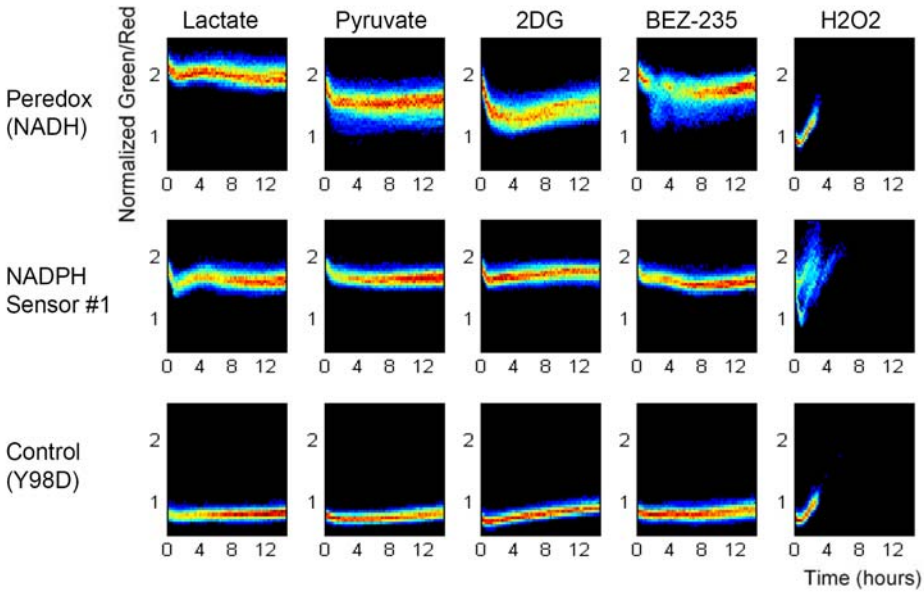

Figure 4.3. MCF-10A cells stably expressing Peredox, NADPH sensor #1, or the control Y98D reporter upon metabolic or signaling challenges

Heat maps of normalized fluorescence ratios of MCF-10A cells stably expressing nuclear-targeted Peredox (top), NADPH sensor #1 (middle), or the control Y98D reporter (bottom). Cells were treated with lactate (25 mM), pyruvate (25 mM), 2-deoxyglucose (2DG; 25 mM), BEZ235 (1 μM), or hydrogen peroxide (H2O2; 0.4 mM).

No significant changes in the cytosolic NADPH pool were observed upon the application of lactate (25 mM), pyruvate (25 mM), the glycolytic inhibitor 2-deoxyglucose (2DG; 25 mM), or the dual PI3K/mTOR inhibitor BEZ-235 (1 μM), which perturbed the cytosolic NADH-NAD^+ redox state in parallel experiments. Oxidative challenge by hydrogen peroxide (H2O2; 0.4 mM) led to a decrease in the fluorescence response of NADPH sensor #1 in most cells, indicating a decrease in the cytosolic NADPH pool; however, all cells died quickly within several hours. Future experiments using lower concentrations of hydrogen peroxide or other milder oxidative challenges may elucidate the regulation of cytosolic NADPH pool in live cells. While the cytosolic NADPH pool did not appear to be altered by our glycolytic or signaling perturbations, NADPH sensor #1 may be targeted to subcellular compartments to see if the local changes in the NADPH pool size could be greater, as a result of subcellular production and microdomains of oxidants such as hydrogen peroxide (Mishina et al., 2012).

DETERMINANTS OF THE CYTOSOLIC NADH-NAD^+ REDOX STATE

Dependence on culture condition and cell density

The cytosolic NADH-NAD^+ redox state in cultured MCF-10A cells depended on the culture condition and the cell density (Figure 4.4). In general, cells maintained in the RPMI culture media displayed a higher cytosolic NADH:NAD^+ ratio; this may be due to the absence of pyruvate in the culture media. In contrast, cells in the DMEM/F12 culture media (containing 0.5 mM pyruvate) exhibited lower cytosolic NADH:NAD^+ ratios. Furthermore, given the same culture condition, the cytosolic NADH:NAD^+ ratios

appeared to increase with the cell number/density, presumably due to greater accumulation of lactate.

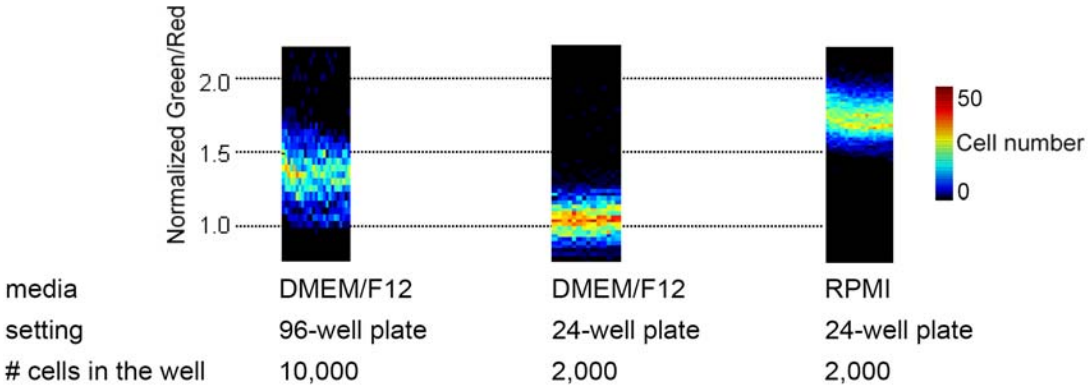

Figure 4.4. Cytosolic NADH-NAD$^+$ redox states of MCF-10A cells vary with the culture condition and the cell number/density

Heat maps of normalized fluorescence ratios of MCF-10A cells stably expressing Peredox-NLS maintained in the DMEM/F12 media with 10,000 cells per well (left), with 2,000 wells per well (middle), or in the RPMI media with 2,000 cells per well (right).

Contributions from various NADH-related metabolic pathways

In general, it may not be straightforward to infer from the cytosolic NADH-NAD$^+$ redox state the status of metabolic pathways such as glycolysis. Cytosolic NADH-NAD$^+$ redox status is determined by a balance between, on one hand, NADH production by glycolysis and lactate oxidation and, on the other hand, NADH consumption by lactate generation and redox shuttling to mitochondria (via the malate-aspartate and the glycerol-3-phosphate shuttles). Still, this simplification ignores other NAD(H)-dependent dehydrogenases that may contribute to the regulation of the cytosolic NADH-NAD$^+$ redox state.

By varying the supply of lactate and pyruvate and using pharmacological means, we attempted to dissect the contributions of various pathways in determining the cytosolic NADH-NAD$^+$ redox state (Figure 4.5).

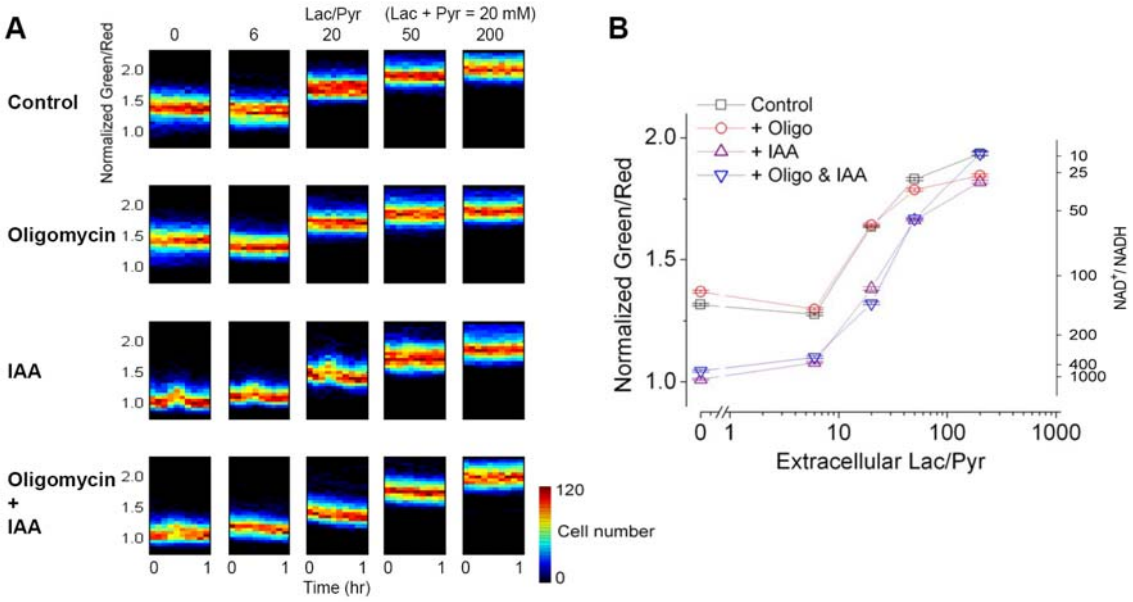

Figure 4.5. Cytosolic NADH-NAD$^+$ redox state of MCF-10A cells in various extracellular lactate:pyruvate ratios upon metabolic inhibition

(A) Heat maps of normalized fluorescence ratios of MCF-10A cells stably expressing Peredox-NLS maintained in various extracellular lactate:pyruvate ratios (with a total lactate and pyruvate concentration of 20 mM), with or without mitochondrial inhibitor oligomycin (1 μM) and/or glycolytic inhibitor iodoacetate (IAA; 100 μM). (B) Normalized fluorescence ratios of Peredox plotted against extracellular lactate:pyruvate ratios with or without metabolic inhibition. The steady state fluorescence response in the presence of glycolytic inhibition was used to calculate the predicted NAD$^+$:NADH ratios in the alternate y-axis, by assuming that the LDH reaction was at equilibrium and a pH of 7.4.

Similar to the data from Neuro-2a cells in Figure 3 in Chapter II, the cytosolic NADH-NAD$^+$ redox states of MCF-10A cells could be poised to different levels by altering the amounts of lactate and pyruvate supplied to the cells. The cytosolic NADH:NAD$^+$ ratio increased with the extracellular lactate:pyruvate ratio, demonstrating a prominent role of redox regulation by the levels of extracellular lactate and pyruvate and by the lactate

dehydrogenase (LDH) enzyme. However, in the presence of glycolytic inhibition with iodoacetate (IAA; 100 μM), the response curves were shifted downward. Consistent with Figure 2.4 in Chapter II, this data indicated that glucose metabolism via glycolysis led to a net NADH generation, shifting the response curve upward. Notably, this shift took place over a wide range of extracellular lactate:pyruvate ratios (and the baseline cytosolic NADH-NAD^+ redox states). Furthermore, unlike glycolytic inhibition, mitochondrial inhibition using oligomycin (1μM) had no effects on the cytosolic NADH-NAD^+ redox state. As the cytosolic-mitochondrial redox shuttling of NADH depends on mitochondrial metabolism and the proton gradient (McKenna et al., 2006), the lack of effects with oligomycin indicated that this redox shuttling may play a minor role in determining the cytosolic NADH-NAD^+ redox state in these cells.

Relationship between cytosolic NADH-NAD^+ redox state and glycolysis

Thus, the cytosolic NADH:NAD^+ ratio depends on both the extracellular lactate:pyruvate ratio and glycolysis. A key question is how the cytosolic NADH-NAD^+ redox state relates to the state of glycolysis in cells. Cytosolic NADH:NAD^+ ratio reflects the balance between NADH production by glycolysis and NADH consumption by LDH (presumably the key dehydrogenase for NAD^+ regeneration). If the glycolytic flux through GAPDH and the LDH flux were identical, one might expect minimal changes in the cytosolic NADH:NAD^+ ratios, despite large changes in the glycolytic flux with compensatory changes in the LDH flux. Nevertheless, in a wide range of extracellular lactate:pyruvate ratios, we observed that glycolysis led to a more reduced cytosolic

NADH-NAD^+ redox state than was poised by the lactate:pyruvate ratios in the absence of glucose. These results led to the following conclusions:

First, more NADH was generated by glycolysis than could be consumed by LDH, indicating that the net forward flux through glycolysis and the net LDH flux for lactate production were not equivalent. In this case, the cytosolic NADH-NAD^+ ratios could be used to report on the state of glycolysis in cells. Future experiments combining cytosolic NADH:NAD^+ ratio imaging with metabolic flux measurements (Neves et al., 2002) may clarify the relationship between the glycolytic flux and the cytosolic NADH-NAD^+ redox state in cells.

Second, in the presence of glucose and glycolytic metabolism, the LDH reaction appeared not to be at equilibrium. Thus, conventional methods to determine cytosolic NADH:NAD^+ ratios by assuming LDH equilibrium and measuring lactate:pyruvate ratios would not be valid, as suggested before (Lowry and Passonneau, 1964; Bücher et al., 1972; Achs and Garfinkel, 1977). Future efforts to create biosensors for lactate and pyruvate and use them in conjunction with Peredox may elucidate the regulation of LDH in live cells, as well as the relationship between the intracellular lactate:pyruvate ratio and the cytosolic NADH:NAD^+ ratio.

CONCLUSION

Biosensor engineering

In conclusion, this dissertation presents several optical tools to study the spatiotemporal dynamics of metabolism in individual live cells. In Chapter 1, we have reviewed the design and the application of various existing genetically encoded fluorescent biosensors of metabolism. In Chapter 2 and Appendix I, we have elaborated on designing Peredox, a biosensor of the cytosolic NADH-NAD^+ redox state. In Appendix II, we have described engineering Perceval, a biosensor of the cellular ATP:ADP ratio. In each of these cases, we created the biosensor by linking a metabolite-binding protein to a fluorescent protein. While the plan appeared to be conceptually simple, these sensor design projects taught us the following lessons:

First, many of the existing biosensors are sensitive to pH changes; as metabolic perturbations often alter intracellular pH (Llopis et al., 1998), pH interference remains a major challenge in using these biosensors. To solve this problem of pH interference, we have engineered a red biosensor of pH that can be used in conjunction with other biosensors to correct for their pH sensitivity, as in Appendix III. Furthermore, we have shown that a pH-resistant GFP can be used to create a pH-resistant biosensor, in this case for the cytosolic NADH-NAD^+ redox state in Chapter II. By minimizing pH interference on the sensor, this rendered the subsequent high-content imaging experiments more robust and reliable.

Second, the original protein scaffolds, from which our biosensors are derived, naturally report on complex metabolic parameters: The Glnk1 protein detects the ATP:ADP ratio (Berg et al., 2009), whereas the Rex protein senses the parameter

[NADH]×[H^+]/[NAD^+] (Hung et al., 2011). Only after we understood their sensing behaviors could these protein domains be utilized effectively for biosensor design.

Finally, given the vastness of the metabolome, our biosensors are merely a beginning. Even though the ATP:ADP ratio and the cytosolic NADH:NAD^+ ratio are key metabolic parameters, we would need more than these two readouts to tackle the complexity of cell metabolism. It will be critical to optimize large-scale production and screening of biosensors; this may be best achieved by efficient protein screening (Zhao et al., 2011) or sensor design using RNA aptamers (Paige et al., 2011; Paige et al., 2012).

Application of metabolic biosensors in neurobiology

Our initial motivation to create fluorescent biosensors was to apply these optical tools in neurobiology. Brain metabolism is dynamically regulated; the relationship between neural activity and metabolism provides the basis for functional neuroimaging (Phelps et al., 1981) and underlies various neurological diseases (Abou-Sleiman et al., 2006; Pan et al., 2008). While glucose is the primary fuel for the whole brain (Sokoloff et al., 1977), it remains unclear whether particular neural cell types preferentially metabolize glucose. According to the lactate shuttle hypothesis, astrocytes predominantly carry out glycolysis to produce lactate, which is supplied to neighboring neurons for mitochondrial oxidation during neural activity (Pellerin and Magistretti, 1994). Lines of evidence for and against this hypothesis have been put forth, but a consensus is lacking (Chih et al., 2003; Schurr, 2006; Pellerin et al., 2007; Nehlig and Coles, 2007), as evaluation of glycolysis at the single cell level in the brain had been unattainable. In Chapter 2, we have shown that primary cultured neurons and astrocytes differed in their

cytosolic NADH-NAD^+ redox states despite being given the same condition. Currently, we are combining our fluorescent biosensors with two-photon fluorescence lifetime imaging (Lee et al., 2009; Tantama et al., 2011) to examine how glycolysis may differ between neurons and astrocytes in the brain slice preparations – and eventually *in vivo*. Future experiments will also focus on how neurons and astrocytes may alter their glucose metabolism depending on their fuel supply and neural activity. Through these upcoming studies, we hope to unravel the connection between brain metabolism and excitability, as well as the mechanistic basis of how dietary therapy can provide dramatic anticonvulsant effects in the treatment of epilepsy (Yellen, 2008).

Application of metabolic biosensors in cancer biology

Cancer cells often exhibit hallmarks of anaerobic glucose metabolism: Despite the presence of oxygen, glucose is metabolized into lactate (Warburg, 1956; Koppenol et al., 2011). Known as the Warburg effect, this metabolic process generates glycolytic intermediates for biosynthesis of macromolecules that are essential to cell proliferation (Vander Heiden et al., 2009). In this case, excess production of lactate from glycolytic pyruvate is presumably driven by elevated cytosolic NADH:NAD^+ ratios. In Chapter 2, we have measured in cultured cancer cell lines a surprisingly reduced cytosolic NADH-NAD^+ redox state. Depending on the supply of glucose, lactate, and pyruvate, their cytosolic NADH:NAD^+ ratios could approach ~0.1, about 10-fold greater than values estimated from hepatocytes in a gluconeogenic state *in vivo* (Williamson et al., 1967; Sistare and Haynes, 1985). With such elevated cytosolic NADH:NAD^+ ratios, it was unclear how the glyceraldehyde-3-phosphate dehydrogenase (GAPDH) reaction could

proceed in the net forward direction, maintaining a net forward glycolytic flux to generate more NADH. We speculate that cancer cells maintain a net forward glycolytic flux irrespective of a high cytosolic NADH:NAD^+ ratio by the following mechanisms: First, cancer cells may modulate the expression of LDH and monocarboxylate transporter (MCT) isoforms (Shim et al., 1997; Fantin et al., 2006; Le Floch et al., 2011) to maximize the secretion of lactate and pyruvate into the extracellular space (Grassian et al., 2011), maintaining a low intracellular pyruvate pool and driving glycolysis forward. Second, upon sulfenylation of the active site cysteine in GAPDH by oxidative stress (Parker and Allison, 1969; Leonard et al., 2009), the 3-phosphoglycerate kinase (PGK) reaction may be bypassed, thus uncoupling glycolysis from ATP synthesis and rendering NADH production far more favorable thermodynamically (Veech et al., 1979). Future experiments using Peredox in conjunction with other biosensors and chemical modifiers may explore these possibilities and elucidate how cancer cells regulate their NADH-NAD^+ redox state and glycolysis.

Understanding metabolism at the single cell level

Beyond applications in neurobiology and cancer biology, optical probes for metabolic signals are poised to address fundamental questions on glycolysis and metabolic regulation. While glycolysis comprises merely ten biochemical reactions, all of which have been characterized extensively, it remains uncertain how these reactions operate as a whole and are regulated in the context of a live cell. We anticipate that single cell imaging of metabolism using fluorescent biosensors will complement measurements from biochemical studies, provide information for computational models, and yield an

integrated understanding on glycolysis and the regulation of metabolism in health and disease.

REFERENCES

Abou-Sleiman, P. M., Muqit, M. M. K. and Wood, N. W. (2006). Expanding insights of mitochondrial dysfunction in Parkinson's disease. Nat Rev Neurosci *7*, 207–219.

Achs, M. J. and Garfinkel, D. (1977). Computer simulation of rat heart metabolism after adding glucose to the perfusate. Am J Physiol *232*, R175–R184.

Bücher, T., Brauser, B., Conze, A., Klein, F., Langguth, O. and Sies, H. (1972). State of oxidation-reduction and state of binding in the cytosolic NADH-system as disclosed by equilibration with extracellular lactate-pyruvate in hemoglobin-free perfused rat liver. Eur J Biochem *27*, 301–317.

Berg, J., Hung, Y. P. and Yellen, G. (2009). A genetically encoded fluorescent reporter of ATP:ADP ratio. Nat Methods *6*, 161–166.

Chih, C. P., Lipton, P. and Roberts, E. L. (2001). Do active cerebral neurons really use lactate rather than glucose? Trends Neurosci *24*, 573–578.

Durkacz, B. W., Omidiji, O., Gray, D. A. and Shall, S. (1980). (ADP-ribose)n participates in DNA excision repair. Nature *283*, 593–596.

Fantin, V. R., St-Pierre, J. and Leder, P. (2006). Attenuation of LDH-A expression uncovers a link between glycolysis, mitochondrial physiology, and tumor maintenance. Cancer Cell *9*, 425–434.

Floch, R. L., Chiche, J., Marchiq, I., Naïken, T., Ilk, K., Murray, C. M., Critchlow, S. E., Roux, D., Simon, M.-P. and Pouysségur, J. (2011). CD147 subunit of lactate/H^+ symporters MCT1 and hypoxia-inducible MCT4 is critical for energetics and growth of glycolytic tumors. Proc Natl Acad Sci U S A *108*, 16663–16668.

Grassian, A. R., Metallo, C. M., Coloff, J. L., Stephanopoulos, G. and Brugge, J. S. (2011). Erk regulation of pyruvate dehydrogenase flux through PDK4 modulates cell proliferation. Genes Dev *25*, 1716–1733.

Hedeskov, C. J., Capito, K. and Thams, P. (1987). Cytosolic ratios of free [NADPH]/[$NADP^+$] and [NADH]/[NAD^+] in mouse pancreatic islets, and nutrient-induced insulin secretion. Biochem J *241*, 161–167.

Hung, Y. P., Albeck, J. G., Tantama, M. and Yellen, G. (2011). Imaging cytosolic NADH-NAD^+ redox state with a genetically encoded fluorescent biosensor. Cell Metab *14*, 545–554.

Imai, S., Armstrong, C. M., Kaeberlein, M. and Guarente, L. (2000). Transcriptional silencing and longevity protein Sir2 is an NAD-dependent histone deacetylase. Nature *403*, 795–800.

Koppenol, W. H., Bounds, P. L. and Dang, C. V. (2011). Otto Warburg's contributions to current concepts of cancer metabolism. Nat Rev Cancer *11*, 325–337.

Lee, S.-J. R., Escobedo-Lozoya, Y., Szatmari, E. M. and Yasuda, R. (2009). Activation of CaMKII in single dendritic spines during long-term potentiation. Nature *458*, 299–304.

Leonard, S. E., Reddie, K. G. and Carroll, K. S. (2009). Mining the thiol proteome for sulfenic acid modifications reveals new targets for oxidation in cells. ACS Chem Biol *4*, 783–799.

Llopis, J., McCaffery, J. M., Miyawaki, A., Farquhar, M. G. and Tsien, R. Y. (1998). Measurement of cytosolic, mitochondrial, and Golgi pH in single living cells with green fluorescent proteins. Proc Natl Acad Sci U S A *95*, 6803–6808.

Lowry, O. H. and Passonneau, J. V. (1964). The relationships between substrates and enzymes of glycolysis in brain. J Biol Chem *239*, 31–42.

McKenna, M. C., Waagepetersen, H. S., Schousboe, A. and Sonnewald, U. (2006). Neuronal and astrocytic shuttle mechanisms for cytosolic-mitochondrial transfer of reducing equivalents: current evidence and pharmacological tools. Biochem Pharmacol *71*, 399–407.

Mishina, N. M., Tyurin-Kuzmin, P. A., Markvicheva, K. N., Vorotnikov, A. V., Tkachuk, V. A., Laketa, V., Schultz, C., Lukyanov, S. and Belousov, V. V. (2011). Does cellular hydrogen peroxide diffuse or act locally? Antioxid Redox Signal *14*, 1–7.

Nakahata, Y., Sahar, S., Astarita, G., Kaluzova, M. and Sassone-Corsi, P. (2009). Circadian control of the NAD^+ salvage pathway by CLOCK-SIRT1. Science *324*, 654–657.

Nehlig, A. and Coles, J. A. (2007). Cellular pathways of energy metabolism in the brain: is glucose used by neurons or astrocytes? Glia *55*, 1238–1250.

Neves, A. R., Ventura, R., Mansour, N., Shearman, C., Gasson, M. J., Maycock, C., Ramos, A. and Santos, H. (2002). Is the glycolytic flux in *Lactococcus lactis* primarily controlled by the redox charge? Kinetics of NAD^+ and NADH pools determined in vivo by 13C NMR. J Biol Chem *277*, 28088–28098.

Nicholls, D. G. and Ferguson, S. J. (2002). Bioenergetics, Third Edition. 3 edition, Academic Press.

Paige, J. S., Nguyen-Duc, T., Song, W. and Jaffrey, S. R. (2012). Fluorescence imaging of cellular metabolites with RNA. Science *335*, 1194.

Paige, J. S., Wu, K. Y. and Jaffrey, S. R. (2011). RNA mimics of green fluorescent protein. Science *333*, 642–646.

Pan, J. W., Williamson, A., Cavus, I., Hetherington, H. P., Zaveri, H., Petroff, O. A. C. and Spencer, D. D. (2008). Neurometabolism in human epilepsy. Epilepsia *49 Suppl 3*, 31–41.

Parker, D. J. and Allison, W. S. (1969). The mechanism of inactivation of glyceraldehyde 3-phosphate dehydrogenase by tetrathionate, o-iodosobenzoate, and iodine monochloride. J Biol Chem *244*, 180–189.

Pellerin, L., Bouzier-Sore, A.-K., Aubert, A., Serres, S., Merle, M., Costalat, R. and Magistretti, P. J. (2007). Activity-dependent regulation of energy metabolism by astrocytes: an update. Glia *55*, 1251–1262.

Pellerin, L. and Magistretti, P. J. (1994). Glutamate uptake into astrocytes stimulates aerobic glycolysis: a mechanism coupling neuronal activity to glucose utilization. Proc Natl Acad Sci U S A *91*, 10625–10629.

Phelps, M. E., Kuhl, D. E. and Mazziota, J. C. (1981). Metabolic mapping of the brain's response to visual stimulation: studies in humans. Science *211*, 1445–1448.

Pollak, N., Dölle, C. and Ziegler, M. (2007). The power to reduce: pyridine nucleotides–small molecules with a multitude of functions. Biochem J *402*, 205–218.

Ramsey, K. M., Yoshino, J., Brace, C. S., Abrassart, D., Kobayashi, Y., Marcheva, B., Hong, H.-K., Chong, J. L., Buhr, E. D., Lee, C., Takahashi, J. S., Imai, S.-I. and Bass, J. (2009). Circadian clock feedback cycle through NAMPT-mediated NAD^+ biosynthesis. Science *324*, 651–654.

Schurr, A. (2006). Lactate: the ultimate cerebral oxidative energy substrate? J Cereb Blood Flow Metab *26*, 142–152.

Shim, H., Dolde, C., Lewis, B. C., Wu, C. S., Dang, G., Jungmann, R. A., Dalla-Favera, R. and Dang, C. V. (1997). c-Myc transactivation of LDH-A: implications for tumor metabolism and growth. Proc Natl Acad Sci U S A *94*, 6658–6663.

Sickmier, E. A., Brekasis, D., Paranawithana, S., Bonanno, J. B., Paget, M. S. B., Burley, S. K. and Kielkopf, C. L. (2005). X-ray structure of a Rex-family repressor/NADH complex insights into the mechanism of redox sensing. Structure *13*, 43–54.

Sistare, F. D. and Haynes, R. C. (1985). The interaction between the cytosolic pyridine nucleotide redox potential and gluconeogenesis from lactate/pyruvate in isolated rat hepatocytes. Implications for investigations of hormone action. J Biol Chem *260*, 12748–12753.

Sokoloff, L., Reivich, M., Kennedy, C., Des Rosiers, M. H., Patlak, C. S., Pettigrew, K. D., Sakurada, O. and Shinohara, M. (1977). The [14C]deoxyglucose method for the measurement of local cerebral glucose utilization: theory, procedure, and normal values in the conscious and anesthetized albino rat. J Neurochem *28*, 897–916.

Tantama, M., Hung, Y. P. and Yellen, G. (2011). Imaging intracellular pH in live cells with a genetically encoded red fluorescent protein sensor. J Am Chem Soc *133*, 10034–10037.

Vander Heiden, M. G., Cantley, L. C. and Thompson, C. B. (2009). Understanding the Warburg effect: the metabolic requirements of cell proliferation. Science *324*, 1029–1033.

Veech, R. L., Eggleston, L. V. and Krebs, H. A. (1969). The redox state of free nicotinamide-adenine dinucleotide phosphate in the cytoplasm of rat liver. Biochem J *115*, 609–619.

Veech, R. L., Lawson, J. W., Cornell, N. W. and Krebs, H. A. (1979). Cytosolic phosphorylation potential. J Biol Chem *254*, 6538–6547.

Wang, W., Fang, H., Groom, L., Cheng, A., Zhang, W., Liu, J., Wang, X., Li, K., Han, P., Zheng, M., Yin, J., Wang, W., Mattson, M. P., Kao, J. P. Y., Lakatta, E. G., Sheu, S.-S., Ouyang, K., Chen, J., Dirksen, R. T. and Cheng, H. (2008). Superoxide flashes in single mitochondria. Cell *134*, 279–290.

Warburg, O. (1956). On the origin of cancer cells. Science *123*, 309–314.

Williamson, D. H., Lund, P. and Krebs, H. A. (1967). The redox state of free nicotinamide-adenine dinucleotide in the cytoplasm and mitochondria of rat liver. Biochem J *103*, 514–527.

Yellen, G. (2008). Ketone bodies, glycolysis, and KATP channels in the mechanism of the ketogenic diet. Epilepsia *49 Suppl 8*, 80–82.

Zapata-Hommer, O. and Griesbeck, O. (2003). Efficiently folding and circularly permuted variants of the Sapphire mutant of GFP. BMC Biotechnol *3*, 5.

Zhao, Y., Araki, S., Wu, J., Teramoto, T., Chang, Y.-F., Nakano, M., Abdelfattah, A. S., Fujiwara, M., Ishihara, T., Nagai, T. and Campbell, R. E. (2011). An expanded palette of genetically encoded Ca^{2+} indicators. Science *333*, 1888–1891.

Appendix I

Supplemental information: Imaging cytosolic NADH-NAD^+ redox state with a genetically encoded fluorescent biosensor

Yin Pun Hung [1], John G. Albeck [2], Mathew Tantama [1], and Gary Yellen [1]

[1] Department of Neurobiology and [2] Department of Cell Biology, Harvard Medical School, 220 Longwood Avenue, Boston, Massachusetts 02115, USA

Reprinted from Hung YP, Albeck JG, Tantama M, Yellen G. (2011). Imaging cytosolic NADH-NAD^+ redox state with a genetically encoded fluorescent biosensor. *Cell Metabolism*. 14(4):545-554.

Yin Pun Hung contributed all figures in this chapter.

Inventory of Supplemental Information

Figure S1 relates to Figure 2.1A.

Figure S2 relates to Figure 2.1, describing further properties of the P0 sensor.

Figure S3 relates to Figure 2.2, showing spectral properties, pH sensitivity, and ligand specificity of the Peredox sensor.

Figure S4 relates to Figure 2.3, showing the cumulative histograms of non-transfected and transfected cells.

Figure S5 relates to Figure 2.4, showing individual and average cell responses to manipulations of glucose levels or metabolic challenge.

Figure S6 relates to Figure 2.4, showing NADH:NAD^+ redox in rat glioma C6 cells.

Table S1 relates to Figure 2.2, showing the photophysical properties of the Peredox sensor.

Supplemental experimental procedures relates to Chapter 2.

A

T-Rex 1st subunit mutations: S30A, R46D, K58D, E116G, K117M, K204T

L-linker: PTW$_{205}$–SAAGGHG–F$_{145}$TAHNV

cpmTS mutations: N146T S147A A206K

Linker for circular permutation within cpmTS: DELYK$_{238}$–GGTGGS–M$_1$VSKG

R-linker: HKLEYN$_{144}$–T–K$_2$VPE

T-Rex 2nd subunit mutations: S30A, R46D, K47E, K58D, E116G, K117M

mC-linker: PKWREEMMG$_{211}$–SGTGGNASDGGGSGG–M$_1$VSKG

B

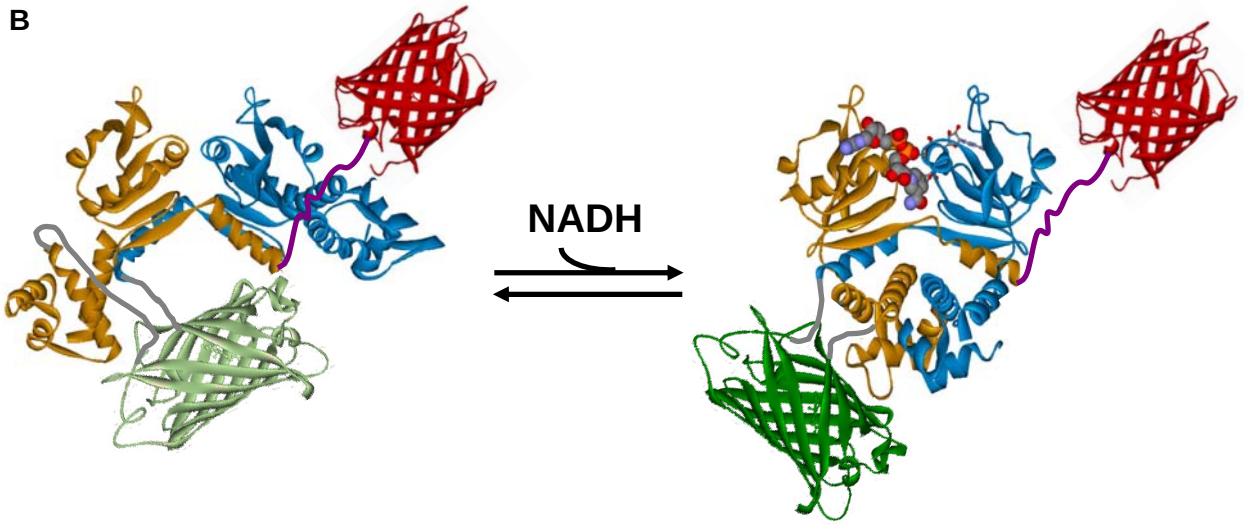

Figure S1. Design of a fluorescent NADH reporter

(A) Schematic representation of P0, encoding a cpFP variant of T-Sapphire (cpmTS) inserted into a tandem dimer of Rex from *Thermus aquaticus* (T-Rex). The first subunit of T-Rex contained residues Met1 to Trp205 (wild type T-Rex numbering), and the second subunit contained residues Lys2 to Gly211. To minimize potential interactions with DNA or NADPH, both subunits contained the mutations S30A, R46D, K58D, E116G and K117M. T-Sapphire was circularly permuted, beginning at Phe145 (standard GFP numbering) and ending at Asn144; the mutation A206K was introduced to minimize potential aggregation to yield cpmTS. To normalize for sensor concentration, mCherry was attached with a linker to the C-terminus of the Rex-cpmTS chimera. Three additional mutations (Y98W and F189I in the first Rex subunit and Y98W in the second Rex subunit) were introduced in P0 to create Peredox. (B) In this model, the green cpFP (PDB: 3evp) interposed between the two Rex subunits (blue and orange) changed its fluorescence upon NADH binding (balls and sticks). The open (left) and closed (right) conformations of Rex were from the crystal structures of B-Rex (PDB: 2vt2) and T-Rex (PDB: 1xcb), respectively. The green cpFP signal was normalized by the red fluorescence of mCherry (PDB: 2h5q).

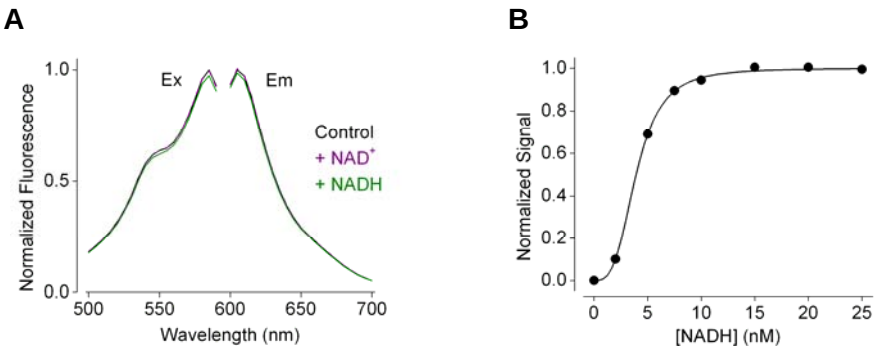

Figure S2. Additional characterization of purified P0

(A) Excitation and emission spectra of the mCherry tandemly attached to Rex-cpmTS in the control condition (solid black), after addition of 100 μM NAD^+ (dash purple), or 100 μM NAD^+ and 0.2 μM NADH (solid green), normalized to the peak intensity in the control condition. For excitation spectra, emission was measured at 610 ± 5 nm; for emission spectra, excitation was at 580 ± 2.5 nm. (B) NADH affinity. Fluorescence response to NADH at 25°C, normalized to initial and final values. The affinity of P0 for NADH was under 5 nM.

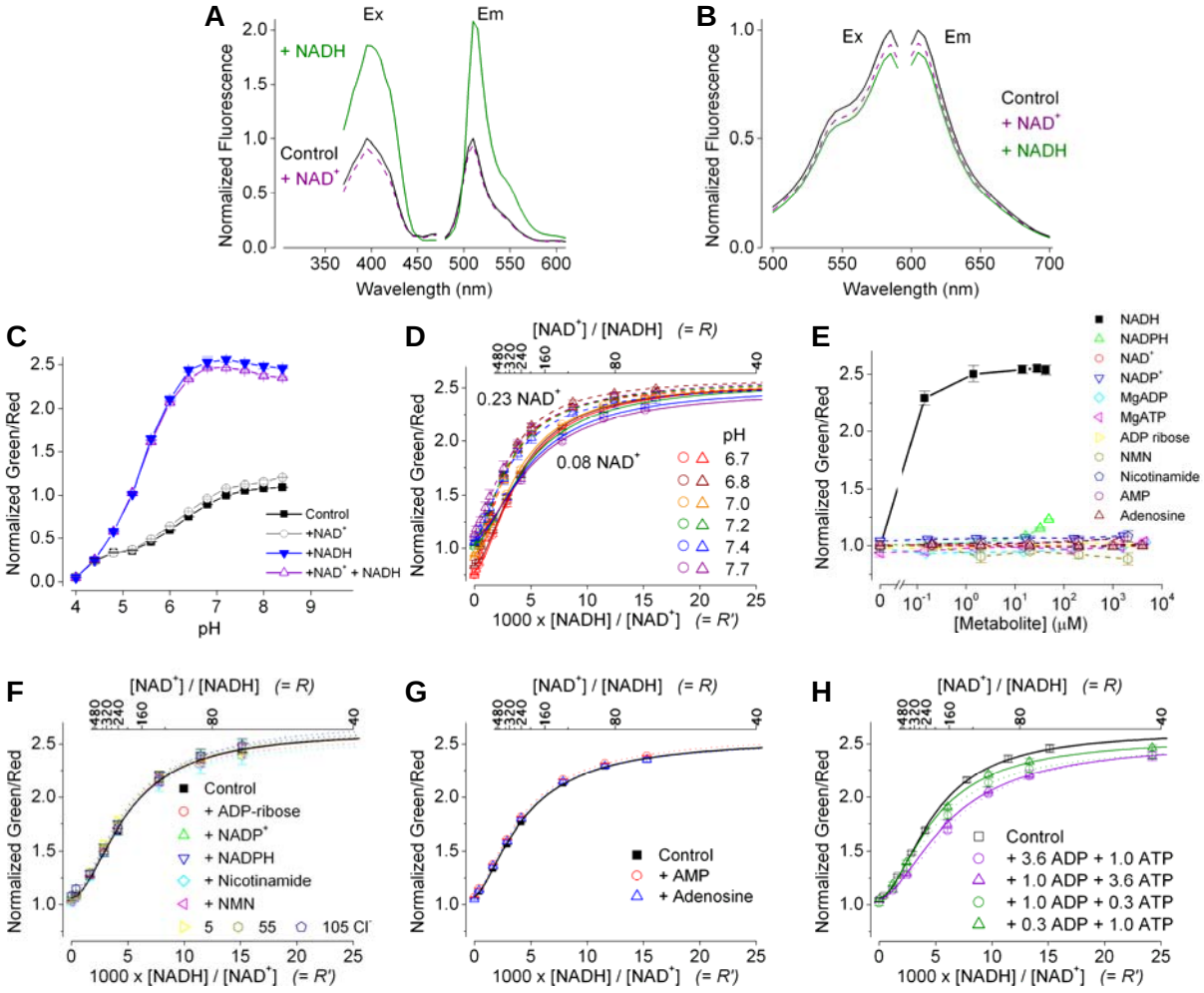

Figure S3. Additional characterization of purified Peredox

(A) and (B) Excitation and emission spectra of Peredox in the control condition (solid black), after addition of 100 μM NAD^+ (dash purple), or 100 μM NAD^+ and 1.5 μM NADH (solid green), normalized to the peak intensity in the control condition. In (A), for excitation spectra, emission was measured at 510 ± 5 nm; for emission spectra, excitation was at 400 ± 2.5 nm. In (B), for excitation spectra, emission was measured at 610 ± 5 nm; for emission spectra, excitation was at 580 ± 2.5 nm. (C) Fluorescence ratios in the control condition, after addition of 170 μM NAD^+, 4 μM NADH, or 170 μM NAD^+ and 4 μM NADH in the pH range between 4.0 and 8.4. (D) Fluorescence ratios at indicated pH plotted against *R′* or *R*, with NAD^+ of 0.08 mM or 0.23 mM. (E) Fluorescence ratios plotted against concentrations of metabolite applied to the sensor alone. (F) Fluorescence ratios in the presence of ADP ribose (10 μM), $NADP^+$ (4 μM), NADPH (4 μM), nicotinamide (400 μM), β-nicotinamide mononucleotide NMN (400 μM), or chloride (5 mM, 55 mM, and 105 mM) plotted against *R′* or *R*, with 0.08 mM NAD^+. (G) Fluorescence ratios in the presence of AMP (200 μM) or adenosine (1 mM) plotted against *R′* or *R*, with 0.08 mM NAD^+. (H) Fluorescence ratios in the presence of indicated ADP and ATP plotted against *R′* or *R*, with 0.08 mM NAD^+ at 25°C. Fluorescence ratios (mean ± SEM, *n* = 3) were normalized to the control condition in the absence of pyridine nucleotides at pH 7.2 at 25°C.

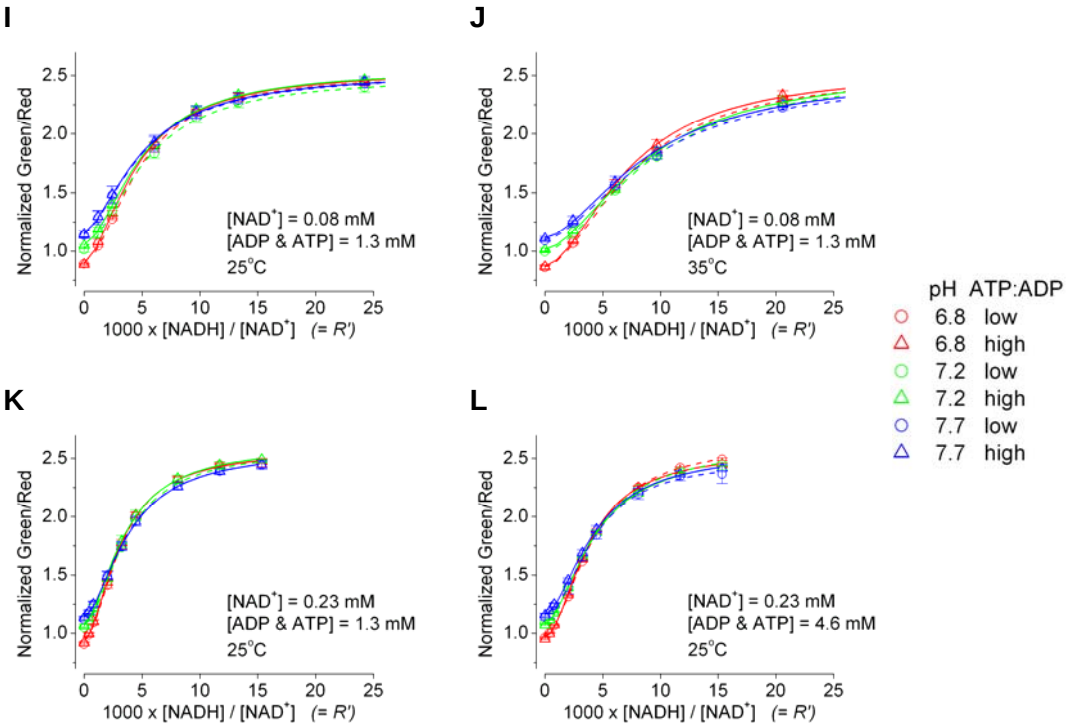

Figure S3 (continued). Additional characterization of purified Peredox

(I-L) Fluorescence ratios at the indicated ATP:ADP ratios (low, 0.3; high, 3.6), NAD^+ and total adenine nucleotide concentrations, pH, and temperature plotted against *R′*. Fluorescence ratios (mean ± SEM, *n* = 3) were normalized to the control condition in the absence of pyridine nucleotides at pH 7.2.

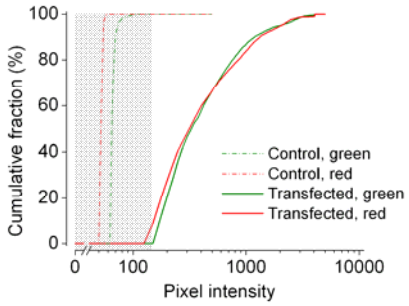

Figure S4. Comparison of fluorescence intensity between transfected and control cells

Cumulative fraction plotted against green and red fluorescence pixel intensity for Neuro-2a cells transfected with Peredox (solid) or non-transfected control (dotted). For each set, multiple images were collected, and 5,000 of the brightest pixels were plotted. Data had not been background subtracted, with the region below the threshold for ratio analysis highlighted in grey. Compared to autofluorescence in the control, both green and red fluorescence signals in transfected cells were far higher.

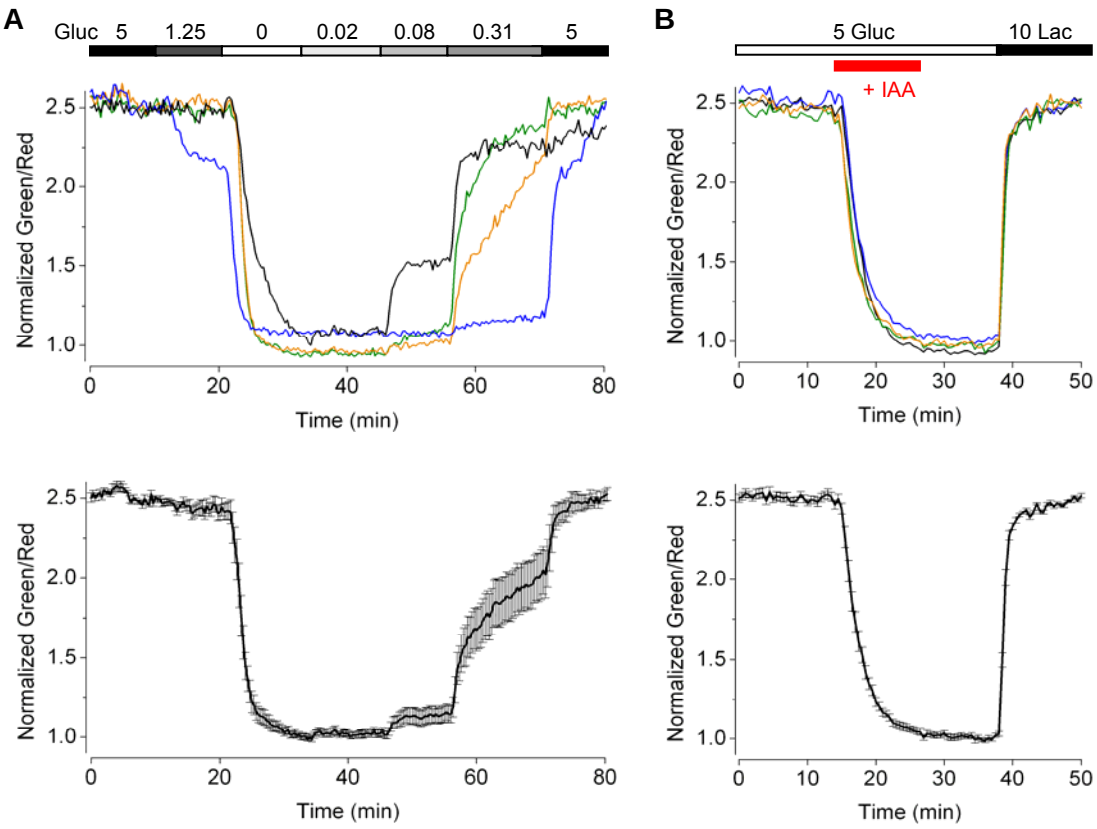

Figure S5. Imaging cytosolic NADH-NAD$^+$ redox dynamics by varying glucose supply or during metabolic challenge

(A) Time course of fluorescence responses of four Neuro-2a cells (top) or average response (bottom; mean ± SEM, *n* = 9) perfused with glucose concentration as indicated. (B) Time course of fluorescence responses of four Neuro-2a cells (top) or average response (bottom; mean ± SEM, *n* = 9) challenged with 0.5 mM iodoacetate (IAA) as indicated.

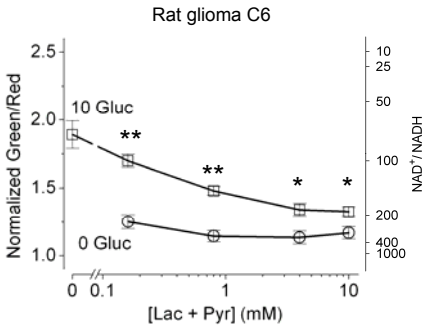

Figure S6. Cultured rat glioma C6 cells supplied with glucose showed a more reduced cytosolic NADH-NAD^+ redox state

Steady state fluorescence responses of cultured rat glioma C6 cells, plotted against total concentrations of extracellular lactate and pyruvate, with a constant lactate:pyruvate ratio of 10, and glucose of 10 mM or 0 mM (mean ± SEM, n = 5 cells from four independent experiments). For the alternate y axis, the predicted NAD^+:NADH ratio was calculated from purified protein measurements. * $p < 0.05$ and ** $p < 0.01$ (paired t-test) vs. corresponding condition with 0 mM glucose.

	Ex (nm)	Em (nm)	EC (M^{-1} cm^{-1})	QY	Brightness (%)
Peredox	400	510	36,000	0.21	23
Peredox + NADH	400	510	39,000	0.39	45
NAD(P)H	340	460	6,200	0.02	0.4

Table S1. Summary of the photophysical properties of Peredox as compared to the NAD(P)H autofluorescence

Excitation wavelength maximum (Ex), emission wavelength maximum (Em), extinction coefficient (EC), quantum yield (QY), and brightness (percentage as compared to EGFP) for Peredox in the apo state, or saturated with NADH, as well as for free NAD(P)H autofluorescence (Scott et al., 1970). In this case, mCherry was not attached to the NADH biosensor to minimize the interference of RFP on the measurements of the green signal.

SUPPLEMENTAL EXPERIMENTAL PROCEDURES

Materials

Custom gene synthesis was performed by GenScript. Standard oligonucleotides were from Integrated DNA Technologies. Custom doped oligonucleotides were from Alpha DNA. Error prone PCR was performed using GeneMorph II Random Mutagenesis Kit from Stratagene. Chemicals and reagents were from Sigma unless otherwise noted. Lactate dehydrogenase (EC 1.1.1.27, rabbit-muscle, NAD^+-dependent) was from Worthington.

Gene Construction

A synthetic gene encoding two tandem subunits of Rex from *Thermus aquaticus* (T-Rex) was designed with mammalian codon bias and selected restriction sites. The first subunit was from Met1 to Trp205 (wild type T-Rex numbering), and the second subunit was from Lys2 to Gly211. To minimize potential interactions with DNA or NADPH, both subunits contained the mutations S30A, R46D, K58D, E116G, and K117M. A synthetic gene encoding T-Sapphire was designed with restriction sites to facilitate circular permutation. Circularly permuted monomeric T-Sapphire (cpmTS) had its N terminus at Phe145 (standard GFP numbering); the mutation A206K; and a linker Gly-Gly-Thr-Gly-Gly-Ser between the original N and C termini. Using nested PCR, cpmTS was inserted between the two Rex subunits. The P0 construct contained the mutation K204T in the first Rex subunit; a linker Ser-Ala-Ala-Gly-Gly-His-Gly between the first Rex subunit and the N terminus of cpmTS; mutations N146T S147A in T-Sapphire; an amino acid Thr inserted between the C terminus of cpmTS and the second Rex subunit;

and the mutation K47E in the second Rex subunit. A linker Ser-Gly-Thr-Gly-Gly-Asn-Ala-Ser-Asp-Gly-Gly-Gly-Ser-Gly-Gly connected the Rex-cpmTS chimera to mCherry (Figure S1A). To create Peredox, three additional mutations (Y98W and F189I in the first Rex subunit and Y98W in the second Rex subunit) were introduced. The complete protein and DNA coding sequence of Peredox has been submitted to Addgene. For purified protein measurements, Peredox was subcloned with an N-terminal 7His tag into the bacterial expression vector pRSET B (Invitrogen). For cell imaging experiments, Peredox was subcloned into the mammalian expression vector GW1 (British Biotechnology). Peredox-NLS was created by adding the nuclear localization signal Pro-Lys-Lys-Lys-Arg-Lys-Val-Glu-Asp-Ala to the sensor C terminus (Nagai et al., 2001).

Protein Purification and Characterization

Standard DH5α bacteria expressing the constructs were grown in YT media in 96-well deep well plates at 37°C for 24 hr, then at room temperature for 1–4 days. Bacteria were then centrifuged, lyzed with CelLytic B, and incubated in 96-well HIS-Select high capacity nickel-coated plates at room temperature overnight. Wells were washed with Tris buffered saline with Tween 20 at pH 8.0, and with the MOPS buffer containing (in mM): 100 MOPS, 50 KCl, 5 NaCl, and 0.5 $MgCl_2$, pH 7.3 (KOH). For spectroscopic and kinetic measurements, proteins were eluted using the MOPS buffer supplemented with 20 mM EGTA. Fluorescence was measured with a Fluorolog-3 spectrofluorometer (Horiba Jobin Yvon). Rapid mixing was done with a stopped-flow unit RX.2000 (Applied Photophysics). For microplate experiments, 0.1% bovine serum albumin (BSA) was added to the elution buffer. Eluted samples were transferred to 96-well microplates pre-

blocked with the BSA-containing elution buffer. Fluorescence was measured with a Synergy 4 microplate reader (BioTek) using the following excitation and emission filters (BioTek): 400/30 nm and 528/20 nm for green; 575/15 nm and 635/32 nm for red. After background subtraction, all green to red fluorescence ratios were normalized by a common factor to yield a signal of 1 in the absence of pyridine nucleotides at pH 7.2. Solutions of ATP and ADP were added with Mg^{2+} to maintain a concentration of free Mg^{2+} of 0.5 mM at pH 7.3. For experiments where the chloride concentration was modified (Fig. S3F), potassium gluconate was added to balance the osmolarity. For determination of extinction coefficient and quantum yield, proteins were purified using Ni-NTA spin columns (QIAGEN) and dialyzed into the MOPS buffer with three buffer changes at 4°C. Protein concentrations were determined independently with both the BCA assay (Pierce) and the alkali denaturation method, using the absorbance of alkali denatured *Aequorea* chromophores (44,100 M^{-1} cm^{-1} at 447 nm; Ward, 1981). Extinction coefficients were estimated using absorbance measurements and the Beer's law. Quantum yields were determined using as the reference standards both fluorescein in 0.1 M NaOH (Lakowicz, 1999) and 9-aminoacridine in water (Weber and Teale, 1957). For comparison, the photophysical properties of NAD(P)H autofluorescence was taken from published values (Scott et al., 1970). To determine Peredox specificity against compounds structurally related to NADH, before NADH-NAD^+ titration other metabolites were applied at concentrations at or above the published estimates of physiological concentrations listed below: adenosine, 200 μM (Smolenski et al., 1991); ADP-ribose, 10 μM (Perraud et al., 2005); AMP, 200 μM (Ballard, 1970); free $NADP^+$

and NADPH, <1 μM (Zhang et al., 2002); nicotinamide mononucleotide, 100 μM

(Revollo et al., 2007); and nicotinamide, 400 μM (Bitterman et al., 2002).

Supplemental References

Ballard, F. J. (1970). Adenine nucleotides and the adenylate kinase equilibrium in livers of foetal and newborn rats. Biochem J *117*, 231–235.

Bitterman, K. J., Anderson, R. M., Cohen, H. Y., Latorre-Esteves, M. and Sinclair, D. A. (2002). Inhibition of silencing and accelerated aging by nicotinamide, a putative negative regulator of yeast sir2 and human SIRT1. J Biol Chem *277*, 45099–45107.

Lakowicz, J. R. (1999). Principles of fluorescence spectroscopy. 2nd ed. (New York: Kluwer Academic / Plenum Publishers).

Nagai, T., Sawano, A., Park, E. S. and Miyawaki, A. (2001). Circularly permuted green fluorescent proteins engineered to sense Ca^{2+}. Proc Natl Acad Sci U S A *98*, 3197–3202.

Perraud, A. L., Takanishi, C. L., Shen, B., Kang S., Smith, M. K., Schmitz, C., Knowles, H. M., Ferraris, D., Li, W., Zhang, J., Stoddard, B. L. and Scharenberg, A. M. (2005). Accumulation of free ADP-ribose from mitochondria mediates oxidative stress-induced gating of TRPM2 cation channels. J Biol Chem *280*, 6138–6148.

Revollo, J. R., Körner, A., Mills, K. F., Satoh, A., Wang, T., Garten, A., Dasgupta, B., Sasaki, Y., Wolberger, C., Townsend, R. R., Milbrandt, J., Kiess, W. and Imai, S. (2007). Nampt/PBEF/Visfatin regulates insulin secretion in beta cells as a systemic NAD biosynthetic enzyme. Cell Metab *6*, 363–375.

Scott, T. G., Spencer, R. D., Leonard, N. J. and Weber, G. (1970). Emission properties of NADH. Studies of fluorescence lifetime and quantum efficiencies of NADH, AcPyNADH, and simplified synthetic models. J Am Chem Soc *92*, 687–695.

Smolenski, R. T., Schrader, J., de Groot, H. and Deussen, A. (1991). Oxygen partial pressure and free intracellular adenosine of isolated cardiomyocytes. Am J Physiol *260*, C708–714.

Ward, W. W. (1981). Properties of the coelenterate green-fluorescent proteins. In Bioluminescence and Chemiluminescence: Basic Chemistry and Analytical Applications, De Luca, M. and McElroy, D. W. (New York: Academic), pp. 235–242.

Weber, G. and Teale, F. W. J. (1957). Determination of the absolute quantum yield of fluorescent solutions. Trans Faraday Soc *53*, 646–655.

Zhang, Q., Piston, D. W. and Goodman, R. H. (2002). Regulation of corepressor function by nuclear NADH. Science *295*, 1895–1897.

Appendix II

A genetically encoded fluorescent reporter of ATP:ADP ratio

Jim Berg [1], Yin Pun Hung [1], and Gary Yellen [1]

[1] *Department of Neurobiology, Harvard Medical School, 220 Longwood Avenue, Boston, Massachusetts 02115, USA*

This research was published in *Nature Methods*. Berg J, Hung YP, Yellen G. (2009) A genetically encoded fluorescent reporter of ATP:ADP ratio. *Nat Methods*. 6(2):161-166.

Yin Pun Hung contributed Supplementary Figures 4, 6, and 9.

A genetically encoded fluorescent reporter of ATP:ADP ratio

Jim Berg[1,2], Yin Pun Hung[1] & Gary Yellen[1]

We constructed a fluorescent sensor of adenylate nucleotides by combining a circularly permuted variant of GFP with a bacterial regulatory protein, GlnK1, from *Methanococcus jannaschii*. The sensor's affinity for Mg-ATP was < 100 nM, as seen for other members of the bacterial PII regulator family, a surprisingly high affinity given that normal intracellular ATP concentration is in the millimolar range. ADP bound the same site of the sensor as Mg-ATP, competing with it, but produced a smaller change in fluorescence. At physiological ATP and ADP concentrations, the binding site is saturated, but competition between the two substrates causes the sensor to behave as a nearly ideal reporter of the ATP:ADP concentration ratio. This principle for sensing the ratio of two analytes by competition at a high-affinity site probably underlies the normal functioning of PII regulatory proteins. The engineered sensor, Perceval, can be used to monitor the ATP:ADP ratio during live-cell imaging.

ATP is the primary energy currency in living cells. It also acts as a signaling molecule to coordinate responses to energy status, in part by modulating ion channels[1] and activating signaling cascades[2]. The production and consumption of ATP have been suggested in some cases to be spatially restricted (or 'compartmentalized') in cells[3,4]. To understand fully how such compartmentation of ATP may influence cellular physiology, a visible reporter for cellular ATP is needed. Luciferase, an ATP-consuming enzyme that produces a luminescent product[5], has been used for this purpose: it is genetically expressed in cells, the substrate luciferin is applied, and the resultant ATP-dependent luminescence can be imaged with a photon-counting charge coupled device (CCD) camera[6,7], but general use of this approach is limited by very low signal levels. A fluorescent sensor of ATP would in principle allow better temporal and spatial detection of physiological changes.

Genetically encoded fluorescent biosensors have been created from GFP and its variants using various strategies. Some of these use circularly permuted fluorescent proteins (cpFPs), in which the original N and C termini are connected via a peptide linker, and new N and C termini are created in close proximity to the chromophore[8]. The calcium sensor pericam[9] and hydrogen peroxide sensor HyPer[10] have been created by fusing the N and C termini of a cpFP to specific detector proteins for calcium or hydrogen peroxide, respectively. Conformational changes in the fusion proteins caused by the binding of the analyte to the detector protein domain lead to changes in sensor fluorescence.

We sought a suitable ATP-binding protein with which to use this cpFP approach. The ATP-binding bacterial protein GlnK1, a member of the PII family, is a trimeric intracellular protein that regulates ammonia transport associated with the synthesis of glutamine. In its apo (unliganded) form, it binds to a bacterial ammonia transporter and blocks ammonia import. Only when the GlnK1 protein has bound both Mg-ATP and 2-ketoglutarate, indicating a healthy metabolism and glutamine synthesis precursor availability, does it dissociate from the transporter and permit ammonia transport into the bacterium[11–13]. Binding of Mg-ATP to GlnK1 results in a dramatic conformational change[13] in which the 'T loop' (Gly37–Val53) changes from a very loose disordered structure to a compact ordered loop (**Fig. 1a**). Because of this localized structural change upon ATP binding, we used GlnK1 as a backbone for a fluorescent ATP sensor.

We used the cpFP approach to create an improved cellular ATP biosensor based on GlnK1. Integration of a yellow cpFP, circularly permuted monomeric Venus (cpmVenus), into the T loop of GlnK1 yielded a fluorescent sensor of ATP. We found that this sensor (and likely the native GlnK1 protein) reported the ratio of ATP/ADP levels. An optimized version of this probe expressed in mammalian cells responded to inhibition of cellular metabolism with real-time changes in fluorescence.

RESULTS

A cpFP inserted into GlnK1 reports ATP with high affinity

To engineer an ATP sensor, we inserted cpmVenus into each of six sequential positions (residues Gly48 to Asp54) within the T loop of GlnK1. We expressed these fusion proteins in bacteria and assayed the purified proteins for a fluorescence response to ATP application. Most constructs were fluorescent but did not change fluorescence upon application of ATP. But in the fusion with cpmVenus inserted between Tyr51 and Ile52, a construct named QV5, there was a substantial change in the excitation spectrum upon ATP application (**Fig. 1b**). The basal excitation spectrum of this construct was similar to that of YFP, with a prominent peak around 490 nm and an additional, smaller peak at 405 nm. As ATP was

[1]Department of Neurobiology, Harvard Medical School, 220 Longwood Ave., Boston, Massachusetts 02115, USA. [2]Present address: Department of Physiology, University of California, 1550 4th Street, San Francisco, California 94158, USA. Correspondence should be addressed to G.Y. (gary_yellen@hms.harvard.edu).

RECEIVED 12 JULY 2008; ACCEPTED 17 NOVEMBER 2008; PUBLISHED ONLINE 4 JANUARY 2009; CORRECTED ONLINE 11 JANUARY 2009 (DETAILS ONLINE); DOI:10.1038/NMETH.1288

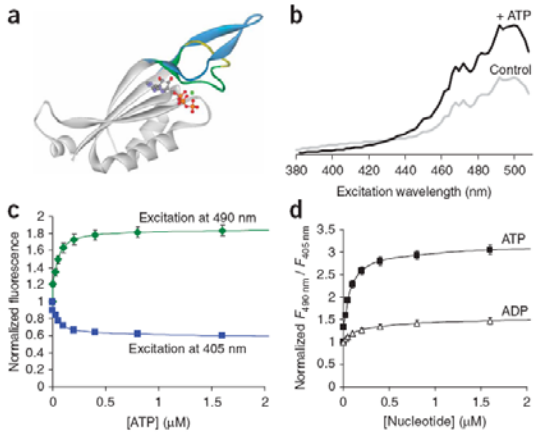

Figure 1 | Properties of the GlnK1-cpmVenus QV5 construct. (**a**) Ribbon representation of one subunit of the GlnK1 protein without a ligand (gray and blue) or with Mg^{2+}-ATP (gray, green and yellow, with the ligand in ball-and-stick form) based on Protein Data Bank files 2j9e and 2j9d (ref. 13). The blue structure is just one of the many alternative and disordered structures observed for the unliganded T loop. The yellow region indicates the insertion points used for the cpFP. (**b**) Excitation spectra of purified QV5 construct under control conditions and after addition of 50 μM Mg-ATP (emission at 530 nm). (**c**) Fluorescence intensities when exciting at 490 nm or 405 nm, normalized to the initial value; emission at 530 nm. (**d**) The ratio of fluorescence intensities when exciting at 490 nm divided by 405 nm ($F_{490\ nm}/F_{405\ nm}$) with application of ATP (affinity = ~0.04 μM) or ADP (affinity = ~0.2 μM). Error bars, ± s.e.m. ($n = 3$).

added, the 405 nm excitation peak diminished and the 490 nm peak was enhanced; thus ATP addition led to a ratiometric change in the excitation spectrum of the QV5 construct. This property, also seen for ratiometric pericam[9] and for HyPer[10], is ideal for a cellular sensor as it permits normalization of the signal irrespective of variation in the concentration of the sensor protein. As seen for the other cpFP-based probes, the shape of the emission spectrum did not change with ligand binding. Relative to cellular levels of ATP, reported to be in the millimolar range[14], the QV5 construct has a surprisingly high affinity of approximately 0.04 μM for ATP (**Fig. 1c**).

In addition to binding ATP, GlnK1 can also bind ADP, although ADP binding does not produce secure T loop closure[13]. ADP application does change the excitation spectrum of the QV5 fusion protein, although at saturating [ADP] there is only an ~1.4-fold change in the ratio of fluorescence emitted at 495 nm to that at 405 nm, compared with a roughly threefold increase with saturating [ATP] (**Fig. 1d**). The [ADP] required for a half-maximal fluorescence response was ~0.2 μM; thus, the QV5 protein has about fivefold higher affinity for ATP than for ADP.

Competition allows the sensor to report the ATP:ADP ratio

The extremely high affinity for ATP as well as the imperfect selectivity over ADP would seem to disqualify this version of the sensor for use in cellular ATP sensing, but in fact the combination of these properties leads to interesting behavior when both nucleotides are present. ATP and ADP compete for binding to the site, but only ATP causes closure of the T loop and a maximal change in fluorescence. Competition by ADP will effectively lower the affinity of the sensor for ATP. This competitive mechanism would predict that the steady-state fluorescence response of the QV5 fusion protein will depend on the ATP:ADP ratio (**Supplementary Results** online), and it will be insensitive to the absolute concentrations of the two nucleotides so long as they exceed the submicromolar affinity constants. The sensitivity should be determined by the relative affinity of the receptor for ATP and ADP. The QV5 construct has about fivefold higher affinity for ATP than for ADP, so that the sensor should be half-active when the [ATP]/[ADP] is ~0.2. We called this ratio at which the sensor response is half maximal the 'K_R' of the sensor, in analogy to the dissociation constant (K_d) of a receptor.

We tested this predicted dependence on the ATP:ADP ratio by measuring the fluorescence response to ATP application in the constant presence of different concentrations of ADP. As predicted, the response depended not on the absolute concentration of ATP alone, but rather on [ATP]/[ADP] (**Fig. 2**). When we added ATP in the presence of 5 μM ADP, the half-maximal fluorescence response occurred when [ATP] was ~1 μM (compared to ~0.04 μM when ADP was absent). This half-maximal response corresponds to an ATP:ADP ratio of ~0.2, which agrees with our expected K_R based on the ratio of ATP and ADP affinities. To test the robustness of the response, we repeated the assay with increasing concentrations of ADP (**Fig. 2**). In each case, the fluorescence response accurately reported the ATP:ADP ratio.

As for other fluorescent protein based sensors, the absolute fluorescence of the QV5 construct is sensitive to pH, but the dose-response for ATP is remarkably insensitive to pH values in the physiological range (**Supplementary Fig. 1** online). In addition, at an excitation wavelength of 435 nm the fluorescence response is isosbestic for nucleotide concentration, regardless of the pH.

The distinctive fluorescence response to ATP and ADP required Mg^{2+} (**Supplementary Results** and **Supplementary Fig. 2** online) and showed minimal interference from other ligands. Other purine nucleotides, such as AMP, NAD^+ or GTP, had little or no effect on the sensor when ADP and ATP were present (**Supplementary Fig. 3** online). We also found that application of 2-ketoglutarate, a

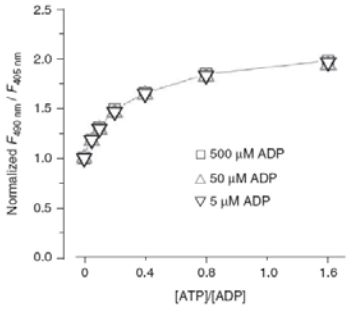

Figure 2 | The QV5 construct reports the ATP:ADP ratio. The QV5 construct fluorescence response to ATP application in the presence of 5 μM, 50 μM and 500 μM ADP showed a half-maximal response at 1 μM, 10 μM and 100 μM ATP, respectively, corresponding to a half-maximal response when [ATP]/[ADP] = ~0.2.

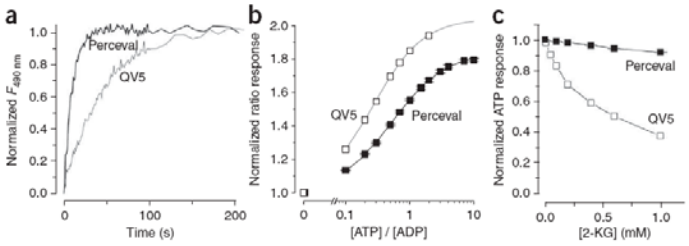

Figure 3 | Perceval is an improved version of the QV5 construct. (**a**) Kinetics of fluorescence response upon addition of a half-maximal dose of ATP to each sensor pre-equilibrated with ADP; responses were normalized to initial and final values. (**b**) Fluorescence response (495 nm/405 nm) to increasing [ATP]/[ADP], normalized to a value of 1 in the presence of saturating ADP. (**c**) Fluorescence response (495 nm/405 nm) to a saturating ATP concentration normalized to that in the absence of 2-ketoglutarate (2-KG). Error bars (± s.e.m., $n = 3$) for Perceval data are smaller than the symbols.

coactivator of the GlnK1 protein, had little effect on the basal fluorescence of the sensor. However, 2-ketoglutarate application did reduce the ATP-dependent fluorescence response in a dose-dependent manner, with an apparent affinity ($K_{apparent}$) of ~0.3 mM (**Fig. 3**).

Optimization of the ATP:ADP ratio sensor

Although the QV5 fusion protein provided a fluorescent readout of ATP:ADP ratio, it required improvement in several of its properties before we could use it as a cellular sensor. Owing to the very high affinity for both ATP and ADP, the kinetics of the response to a change in ATP:ADP ratio were quite slow, with a time constant of around a minute (**Fig. 3a**). Also, the K_R for the initial sensor, ~0.2, was likely still too low to measure interesting changes in the ATP:ADP ratio in cells, as the normal ratio in a 'fully-charged' cell[14] is in the range of 3 to 10. Lastly, the modulation by submillimolar concentrations of the intermediate metabolite 2-ketoglutarate might compromise the use of the sensor in cells.

To optimize the sensor for use in cells, we designed a semirandom mutagenesis screen on the GlnK1 portion of the sensor, targeting residues involved in the ATP binding and T loop conformational rearrangement (**Supplementary Methods** online). Using a high-throughput assay of the fluorescence response to ATP and ADP, we screened approximately 300 variants of the sensor. The best product of this screen was a sensor with improved ATP:ADP binding characteristics. This sensor contained the mutations Ala6Ser and Arg36Thr; the latter mutation affects a residue at the base of the T loop and likely alters the T loop conformational change. Then, using the product of the screen, we created a tandem trimer consisting of the modified QV5 construct linked to two modified GlnK1 protomers. The second and third protomers of this trimer have no fluorescent protein insertion and also have the T loop deleted (**Supplementary Fig. 4** online); this makes the trimer much more compact and also eliminates the opportunity for negative cooperativity reported in some native PII proteins[11]. The tandem trimer showed excellent functional expression in mammalian cells. This permuted sensor of cellular energy value, which we named Perceval, retained the spectral properties and pH and magnesium sensitivity of the original construct (**Supplementary Figs. 5** and **6** online) but had an improved K_R of ~0.5, faster kinetics and lower 2-ketoglutarate sensitivity (**Fig. 3**).

Perceval reports changes in cellular energy

To test the ability of Perceval to report changes in cellular metabolism, we expressed it in cultured HEK293 cells. The fluorescence was nearly uniform throughout the cell, and the spectral properties were very similar to those observed in the cuvette: excitation at 490 nm gave a very strong signal, whereas 430-nm excitation produced considerably lower intensities.

We used the glycolytic inhibitor 2-deoxyglucose to induce a decrease in the intracellular ATP:ADP ratio of the HEK293 cells. This inhibitor is phosphorylated by hexokinase, but it is not metabolized and acts as a competitive inhibitor of the glycolytic enzyme phosphoglucoisomerase, thus reducing cellular ATP production. Within minutes of application of 5 mM 2-deoxyglucose, we observed a sharp decrease in the fluorescence signal with 490 nm excitation. As expected from the cuvette experiments, 2-deoxyglucose induced little change in the signal when exciting at 430 nm, the isosbestic point for the ATP:ADP ratio response. The pixel-by-pixel ratio of the image taken at 490 nm divided by the 430 nm image was fairly consistent throughout the cell and this ratio decreased by ~20% upon 2-deoxyglucose application (**Fig. 4**). During this experiment, there was no change in intracellular pH, as assessed by concurrent measurements using the red pH-indicator dye SNARF-5F (Molecular Probes/Invitrogen).

Some cells showed variations in pH in response to metabolic inhibition. Because Perceval, like most other fluorescent

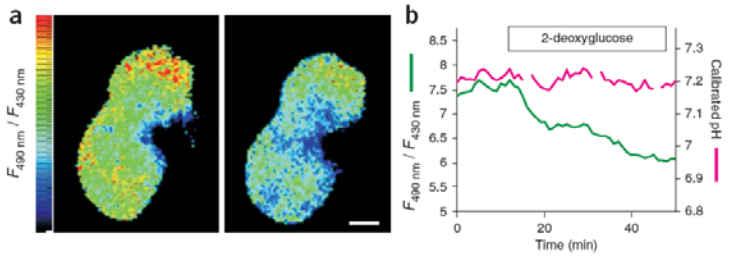

Figure 4 | Metabolic inhibition leads to a change in the Perceval signal. (**a**) A pixel-by-pixel ratio of the 490 nm excitation image by the 430 nm excitation image from two cultured HEK293 cells expressing Perceval during control conditions (left) and after 40 min of metabolic inhibition with 5 mM 2-deoxyglucose (right). Images are pseudocolored with scale of a minimum ratio of 5 (blue) and maximum of 9 (red). Scale bar, 3 μm. (**b**) Plot of $F_{490\ nm}/F_{430\ nm}$ for the bottom cell in **a** shows an ~20% decrease in the ratio after application of 5 mM 2-deoxyglucose (continuously perfused during the period indicated by the bar). Concurrent measurement of intracellular pH of the same cell with the red pH indicator dye SNARF-5F showed no change in pH.

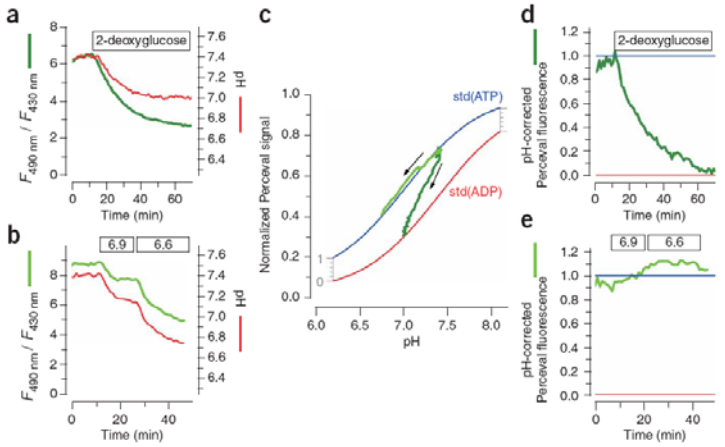

Figure 5 | Concurrent Perceval and pH monitoring, with pH correction of the Perceval signal. (**a**) Results from a cell subjected to a 2-deoxyglucose (5 mM) challenge (continuously perfused during the period indicated by the bar). pH signal was calibrated after the experiment (**Supplementary Methods**). (**b**) Results from a cell with no metabolic challenge, where the pH of the bathing solution was changed to 6.9 and then to 6.6 (as indicated by the bars). (**c**) Plot of the normalized Perceval ratio versus pH (from **a** and **b**). The two standard curves, labeled std (ATP) and std (ADP) are from cuvette assays of the ATP-loaded and ADP-loaded sensor at various pH. The initial signal was scaled to the cuvette data by assuming a starting ATP:ADP ratio of ~4. For each experiment (data from **a** are in dark green and from **b** in bright green), the arrows indicate the progression of time. Notice that pH manipulation (**b**) tracks along the pH dependence of the ATP-loaded sensor. (**d**,**e**) pH-corrected Perceval fluorescence signals from the experiments shown in **a** and **b**. The correction is done for each data point by plotting the fractional occupancy at the actual pH, as indicated by the gray scale in **c**. Blue and red lines indicated the fully ATP-and ADP-loaded states, respectively.

protein–derived sensors, is sensitive to changes in pH, we devised a strategy to isolate any fluorescence changes owing to changes in the ATP:ADP ratio from any pH-induced changes in fluorescence. By concurrently measuring intracellular pH with the pH indicator dye SNARF-5F, we could correct for any changes in the Perceval fluorescence owing to pH. We calibrated the pH measurements at the end of each experiment using various buffered solutions containing high $[K^+]$ and nigericin to equilibrate pH across the plasma membrane (**Supplementary Fig. 7** online). The calibrated pH measurement at each time point could be used to correct the Perceval signal according to its pH dependence in the cuvette experiments. We plotted Perceval signal from a full 2-deoxyglucose experiment (**Fig. 5**) either as a function of time (**Fig. 5a**) or as a function of the pH at each time point (**Fig. 5c**). As the experiment progressed, the pH changes and the plotted points 'moved away' from the ATP-saturated curve toward the ADP-saturated curve, indicating a decline in [ATP]/[ADP]. In contrast, during a control experiment in which we exposed a cell to a low-pH bath solution (but did not metabolically challenge the cell), the intracellular pH and the raw Perceval signal changed substantially (**Fig. 5b**), but the Perceval signal data points remained superimposed on the ATP-saturated curve (**Fig. 5c**). The pH-corrected and normalized Perceval signal (**Fig. 5d**,**e**) indicated a clear change in the ATP:ADP ratio upon metabolic inhibition, but little change during a pure pH challenge. The pH correction appeared to be quite robust during several experiments with different pH challenges (**Supplementary Fig. 8** online).

We next tested the reversibility of the metabolic effect on the Perceval signal by transiently removing glucose from the extracellular solution. This metabolic manipulation led to a slight intracellular alkalinization and to a gradual decrease in the pH-corrected ATP:ADP ratio signal (**Fig. 6**). Upon glucose readministration, the ATP:ADP ratio signal quickly recovered to control levels.

DISCUSSION

Though we originally conceived Perceval as a sensor for ATP concentration alone, in the presence of a mixture of nucleotides, its fluorescence response was directly related not to the absolute amount of ATP, but to the ratio of ATP to ADP. This is consistent with two recent studies[15,16] that reported strong interactions between ADP and ATP on PII proteins (the class of proteins that includes GlnK1). The authors of these reports hypothesized that the competition between ATP and ADP leads these proteins to sense the 'energy charge' of the bacteria. The concept of adenylate energy charge, originally proposed in reference 17, is based on the hypothesis that although

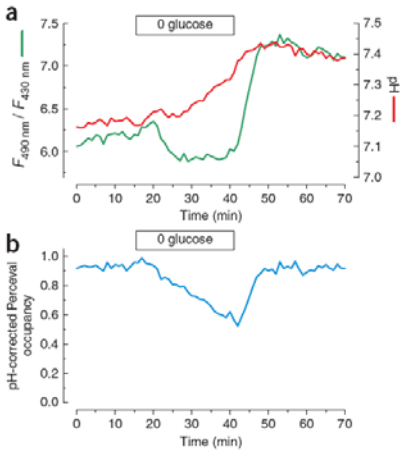

Figure 6 | Transient glucose removal leads to a reversible change in the ATP:ADP ratio signal. (**a**) A cultured HEK293 cell expressing Perceval and loaded with the pH sensitive dye SNARF-5F displayed an alkalinization when glucose was removed from the extracellular solution (10 mM glucose was replaced by equimolar sucrose). The Perceval signal showed a slight decrease upon glucose removal and a prominent rebound upon glucose addition. (**b**) The pH-corrected Perceval fluorescence signal revealed a gradual decrease in cellular energy that reversed rapidly upon glucose reapplication. Perceval occupancy of 0 corresponds to [ADP] ≫ [ATP]; occupancy of 1 corresponds to [ATP] ≫ [ADP].

the absolute individual amounts of ATP, ADP and AMP might vary widely, the ratios of ATP:ADP and ATP:AMP are more reliable indicators of metabolism from cell to cell. Detection of the cellular ATP:ADP ratio is particularly valuable because this ratio determines (along with free inorganic phosphate concentration) the actual free energy of ATP hydrolysis available for cellular reactions. Through the adenylate kinase (AdK) reaction, the ATP:ADP ratio (R) is also closely related to the free concentration of AMP, which is a critical regulator of downstream signaling mechanisms. The kinase AMPK is thought to detect the AMP:ATP ratio[18], which is approximately equal to K_{AdK}/R^2 (where K_{AdK} is the equilibrium constant for the AdK reaction).

Measurements made using tissue homogenates have demonstrated the potential for large changes in cellular ATP:ADP ratio. In mouse pancreatic beta cells, the tissue ATP:ADP ratio rises from ~2–3 to ~8–9 upon glucose stimulation[19]. The ATP:ADP ratio in rat brain tissue has been reported[14,20] as 3–8, and it has been demonstrated to fall from ~8 to ~0.4 after 2 min of ischemia[21]. Most estimates of ATP:ADP ratio are based on measurements of total nucleotide content, but the ratio of free [ATP]/[ADP] (which is detected by Perceval) is suspected to be even higher[22–24] (estimates range from twofold to 20-fold), resulting from sequestration by cellular proteins that is greater for ADP than for ATP. The effect of such ADP-binding may be substantial for cells in a high energy state, but energy depletion (below a total ATP:ADP of ~7 to 30) should rapidly saturate the ADP-binding sites (whose cellular concentration is estimated to be ~0.14 mM[23]) and produce much lower free ATP:ADP ratios, closer to the estimates for total ATP:ADP ratio.

Although the K_R of Perceval, ~0.5, is lower than most of these global measurements, the ATP:ADP ratio of single cells within tissues, and even within a single cell, is likely to vary widely because of localized energy production and consumption. The prompt depletion of energy levels we observed in HEK293 cells (with similar results in COS-7 cells; **Supplementary Fig. 9** online) indicated that Perceval can sense energy deficits, as expected in ischemia, anoxia or high energy consumption states. The present version of Perceval is better tuned for detection of energy deficits, but additional mutagenesis and selection should produce Perceval variants capable of sensing a wider range of ATP:ADP ratios.

In comparison with the existing method for measuring cellular ATP by expression of the firefly luciferase enzyme, Perceval offers many advantages. First, the light-emitting luciferase reaction depends not just on [ATP] but also on the exogenous delivery of luciferin and the presence of molecular O_2. Second, the fluorescence signal from Perceval was much stronger, so measurements can be made with brief, subsecond exposures using a traditional epifluorescence microscope and a standard CCD camera rather than the several-minute exposure using photon-counting CCDs required for luciferase detection. It should be possible to use Perceval to detect subcellular ATP localization, either by using subcellular targeting strategies as used for luciferase[7] or by optical localization using confocal, two-photon or total internal reflection fluorescence (TIRF) microscopy. Lastly, Perceval reports the energy level of the cell by competitive binding of ATP and ADP, whereas luciferase uses an ATP hydrolysis reaction that may perturb the cellular energy balance.

Approaches using nucleic acid aptamers[25,26] have recently produced sensors that distinguish ATP and ADP. This approach is promising, though the current versions have very slow kinetics and require chemical synthesis to conjugate a fluorescent dye. Also, an alternative fluorescence resonance energy transfer (FRET)–based approach to constructing a fluorescent sensor for ATP was recently described[27]. Millimolar ATP alters the FRET ratio of a tandem CFP-YFP construct, but notably, no specific ATP-binding domain is necessary for this effect. As the authors pointed out, this sounds a cautionary note for ATP interference with all FRET-based sensors. The physical basis of the effect is unclear, but it might be exploited for producing a nonratiometric measurement of ATP concentration.

One limitation of Perceval, along with all cpFP-based probes, is that its signal is sensitive to intracellular pH. Unfortunately, many metabolic perturbations also modify intracellular pH, so this sensitivity cannot easily be ignored. Glycolytic inhibition via 2-deoxyglucose has been shown to acidify the cell by ~0.2 pH units in cultured A-431 cells[28] and isolated epithelial cells[29]. We also measured acidification or alkalinization depending on the extent of metabolic inhibition of HEK 293 cells. To correct for pH effects on the Perceval signal, we measured changes in intracellular pH using the pH indicator dye SNARF-5F. Because SNARF-5F fluoresces in the red area of the spectrum, this dye can potentially also be used to correct for any pH influence on the cpFP-based probes pericam or HyPer. Conjugation of these fluorescent sensors to a pH-sensitive red protein, so that both probes are genetically encoded and targetable, may be an even better approach to pH correction.

As a tool for measuring cellular energetics, Perceval should open the door to a more complete understanding of cellular and subcellular variation in metabolism that may occur during normal cellular growth and signaling, during electrical signaling in excitable cells, and in many pathological situations such as cancer cell growth, ischemia and epileptic seizures.

METHODS

GlnK1 synthetic gene construction. A synthetic gene encoding the wild-type GlnK1 of *M. jannaschii* was designed with mammalian codon bias and with selected restriction sites to facilitate construction of the chimeric sensors. A *Kpn*I site at codons 45–47 and a *Bgl*II site at codons 53–55, flanking the T loop, were designed for insertion of the cpFP. An N-terminal 7His tag was added to facilitate purification.

Circularly permuted fluorescent protein. A circularly permuted and monomeric version of the GFP derivative Venus[30] was prepared. Standard PCR methods were used for mutagenesis and chimera construction. The final construct had its N terminus at Venus Tyr145 (numbering corresponds to standard GFP numbering); mutations H148D, Y203F and A206K; and a protein linker Gly-Gly-Ser-Gly-Gly between the original C terminus and N terminus.

Chimera construction. The circularly permuted monomeric Venus was inserted at the desired positions in the T loop using flanking PCR primers. The 5′ end of each primer consisted of 4 bases followed by the flanking restriction site (*Kpn*I or *Bgl*II) and then the desired sequence for the fusion protein; the 3′ end primed on the sequence encoding the N- or C-terminal end of the circularly permuted monomeric Venus coding sequence. After PCR with such a primer pair using the circularly permuted monomeric Venus coding sequence as template, the full-length

product was gel-purified, digested with *Kpn*I and *Bgl*II, gel-purified again, and ligated into the *Kpn*I and *Bgl*II sites of the synthetic gene encoding GlnK1.

Tandem trimer construction. The tandem trimer was constructed (using standard PCR methods) by linking a complete sensor monomer (the first protomer) to two GlnK1 monomers whose T loops were deleted (the second and third protomers; see **Supplementary Fig. 4**). The first linker inserted 13 residues (ASGGGSGGGGASG) between Gly108 of the first-protomer and Met1 of the B protomer. The second linker inserted 13 residues (ASGGGGGSGGASG) between Gly108 of the second protomer and Met1 of the third protomer. The T loop deletion in the second and third protomers eliminated GlnK1 residues 37–53 and replaced them with the linker Gly-Ala-Gly-Gly-Gly. The complete DNA and protein sequence of Perceval is given in **Supplementary Figure 10** online.

Additional methods. Details of random library construction, protein expression and purification, fluorometry, cellular imaging and pH control and calibration are available in **Supplementary Methods**.

Note: Supplementary information is available on the Nature Methods website.

ACKNOWLEDGMENTS

We thank T. Abramson for expert technical assistance with the molecular biology, A. Miyawaki (RIKEN Brain Science Institute) for sending the original plasmid encoding Venus, O. Yildiz and W. Kühlbrandt (Max Planck Institute of Biophysics, Frankfurt am Main) for sending the original plasmid encoding GlnK1, M. Merrick (John Innes Centre) for sending bacterial strains and members of the Yellen lab for their comments and discussion. This work was supported by research grants from the US National Institutes of Health –National Institute of Neurological Disorders and Stroke (NS029693 and NS055031) to G.Y.

AUTHOR CONTRIBUTIONS

G.Y. and J.B. designed the research; G.Y., J.B. and Y.P.H. conducted experiments and wrote the paper.

Published online at http://www.nature.com/naturemethods/
Reprints and permissions information is available online at http://npg.nature.com/reprintsandpermissions/

1. Ashcroft, F.M. & Gribble, F.M. ATP-sensitive K^+ channels and insulin secretion: their role in health and disease. *Diabetologia* **42**, 903–919 (1999).
2. Dennis, P.B. *et al.* Mammalian TOR: a homeostatic ATP sensor. *Science* **294**, 1102–1105 (2001).
3. Weiss, J.N. & Lamp, S.T. Cardiac ATP-sensitive K^+ channels. Evidence for preferential regulation by glycolysis. *J. Gen. Physiol.* **94**, 911–935 (1989).
4. Hoffman, J.F. ATP compartmentation in human erythrocytes. *Curr. Opin. Hematol.* **4**, 112–115 (1997).
5. Wilson, T. & Hastings, J.W. Bioluminescence. *Annu. Rev. Cell Dev. Biol.* **14**, 197–230 (1998).
6. Kennedy, H.J. *et al.* Glucose generates sub-plasma membrane ATP microdomains in single islet beta-cells. Potential role for strategically located mitochondria. *J. Biol. Chem.* **274**, 13281–13291 (1999).
7. Bell, C.J., Manfredi, G., Griffiths, E.J. & Rutter, G.A. Luciferase expression for ATP imaging: application to cardiac myocytes. *Methods Cell Biol.* **80**, 341–352 (2007).
8. Baird, G.S., Zacharias, D.A. & Tsien, R.Y. Circular permutation and receptor insertion within green fluorescent proteins. *Proc. Natl. Acad. Sci. USA* **96**, 11241–11246 (1999).
9. Nagai, T., Sawano, A., Park, E.S. & Miyawaki, A. Circularly permuted green fluorescent proteins engineered to sense Ca^{2+}. *Proc. Natl. Acad. Sci. USA* **98**, 3197–3202 (2001).
10. Belousov, V.V. *et al.* Genetically encoded fluorescent indicator for intracellular hydrogen peroxide. *Nat. Methods* **3**, 281–286 (2006).
11. Ninfa, A.J. & Jiang, P. PII signal transduction proteins: sensors of alpha-ketoglutarate that regulate nitrogen metabolism. *Curr. Opin. Microbiol.* **8**, 168–173 (2005).
12. Durand, A. & Merrick, M. In vitro analysis of the *Escherichia coli* AmtB-GlnK complex reveals a stoichiometric interaction and sensitivity to ATP and 2-oxoglutarate. *J. Biol. Chem.* **281**, 29558–29567 (2006).
13. Yildiz, O., Kalthoff, C., Raunser, S. & Kühlbrandt, W. Structure of GlnK1 with bound effectors indicates regulatory mechanism for ammonia uptake. *EMBO J.* **26**, 589–599 (2007).
14. Erecińska, M. & Silver, I.A. Ions and energy in mammalian brain. *Prog. Neurobiol.* **43**, 37–71 (1994).
15. Wolfe, D.M., Zhang, Y. & Roberts, G.P. Specificity and regulation of interaction between the PII and AmtB1 proteins in Rhodospirillum rubrum. *J. Bacteriol.* **189**, 6861–6869 (2007).
16. Jiang, P. & Ninfa, A.J. *Escherichia coli* PII signal transduction protein controlling nitrogen assimilation acts as a sensor of adenylate energy charge *in vitro*. *Biochemistry* **46**, 12979–12996 (2007).
17. Atkinson, D.E. The energy charge of the adenylate pool as a regulatory parameter. Interaction with feedback modifiers. *Biochemistry* **7**, 4030–4034 (1968).
18. Hardie, D.G., Salt, I.P., Hawley, S.A. & Davies, S.P. AMP-activated protein kinase: an ultrasensitive system for monitoring cellular energy charge. *Biochem. J.* **338**, 717–722 (1999).
19. Nilsson, T., Schultz, V., Berggren, P.O., Corkey, B.E. & Tornheim, K. Temporal patterns of changes in ATP/ADP ratio, glucose 6-phosphate and cytoplasmic free Ca^{2+} in glucose-stimulated pancreatic beta-cells. *Biochem. J.* **314**, 91–94 (1996).
20. DeVivo, D.C., Leckie, M.P., Ferrendelli, J.S. & McDougal, D.B. Chronic ketosis and cerebral metabolism. *Ann. Neurol.* **3**, 331–337 (1978).
21. Folbergrová, J., Minamisawa, H., Ekholm, A. & Siesjö, B.K. Phosphorylase alpha and labile metabolites during anoxia: correlation to membrane fluxes of K^+ and Ca^{2+}. *J. Neurochem.* **55**, 1690–1696 (1990).
22. Veech, R.L., Lawson, J.W., Cornell, N.W. & Krebs, H.A. Cytosolic phosphorylation potential. *J. Biol. Chem.* **254**, 6538–6547 (1979).
23. Mörikofer-Zwez, S. & Walter, P. Binding of ADP to rat liver cytosolic proteins and its influence on the ratio of free ATP/free ADP. *Biochem. J.* **259**, 117–124 (1989).
24. Koretsky, A.P., Brosnan, M.J., Chen, L.H., Chen, J.D. & Dyke, T.V. NMR detection of creatine kinase expressed in liver of transgenic mice: determination of free ADP levels. *Proc. Natl. Acad. Sci. USA* **87**, 3112–3116 (1990).
25. Chiuman, W. & Li, Y. Simple fluorescent sensors engineered with catalytic DNA 'MgZ' based on a non-classic allosteric design. *PLoS ONE* **2**, e1224 (2007).
26. Huizenga, D.E. & Szostak, J.W.A. DNA aptamer that binds adenosine and ATP. *Biochemistry* **34**, 656–665 (1995).
27. Willemse, M., Janssen, E., de Lange, F., Wieringa, B. & Fransen, J. ATP and FRET–a cautionary note. *Nat. Biotechnol.* **25**, 170–172 (2007).
28. Kiang, J.G., McKinney, L.C. & Gallin, E.K. Heat induces intracellular acidification in human A-431 cells: role of Na(+)-H+ exchange and metabolism. *Am. J. Physiol.* **259**, C727–C737 (1990).
29. Brown, S.E., Heming, T.A., Benedict, C.R. & Bidani, A. ATP-sensitive Na(+)-H+ antiport in type II alveolar epithelial cells. *Am. J. Physiol.* **261**, C954–C963 (1991).
30. Nagai, T. *et al.* A variant of yellow fluorescent protein with fast and efficient maturation for cell-biological applications. *Nat. Biotechnol.* **20**, 87–90 (2002).

nature | **methods**

A genetically encoded fluorescent reporter of ATP:ADP ratio

Jim Berg, Yin Pun Hung & Gary Yellen

Supplementary figures and text:

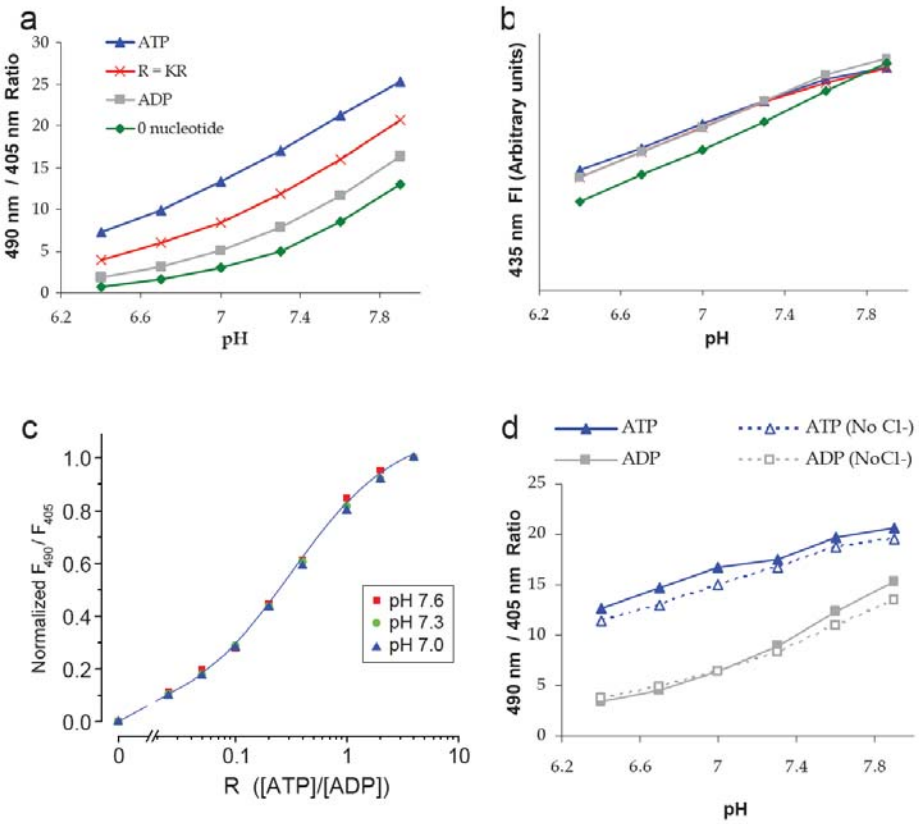

Supplementary Figure 1 | pH and chloride sensitivity of the QV5 construct. (**a**,**b**) pH titrations of purified QV5 construct when maximally activated (*blue*), half maximal (*red*), ADP (*gray*), and nucleotide free (*green*) solutions. The 490 / 405 ratio signal (**a**) exhibits a pH sensitivity that is somewhat parallel between the four signals, indicating that pH is not affecting the ATP response, but is clearly affecting the underlying fluorescence of the sensor. The 435 nm signal (**b**) is isosbestic with respect to ATP:ADP ratio across pH values. (**c**) The dose-response to ATP is relatively unaffected by changes in pH. (**d**) Across a range of pH values, the presence (100 mM KCl) or absence (0 KCl) of chloride does not lead to a substantial change in the QV5 construct ratio.

Nature Methods: doi: 10.1038/nmeth.1288

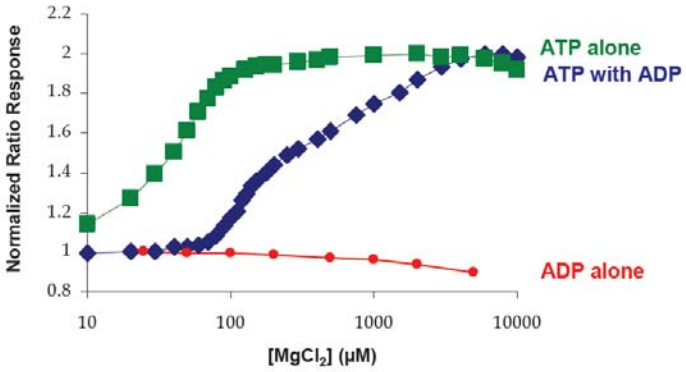

Supplementary Figure 2 | Magnesium Sensitivity of the QV5 construct. The magnesium sensitivity of purified QV5 construct assayed by starting in a magnesium-free solution (with 50 μM EDTA to chelate any contaminating magnesium), then adding $MgCl_2$ to a solution that contains ATP alone (sodium salt, 10 μM, green symbols), ADP alone (potassium salt, 10 μM, red symbols), or a mixture of ATP and ADP (10 μM and 50 μM respectively, blue symbols). As ATP alone binds magnesium (green), the ratio response (490 nm / 405 nm) increases to a maximal value, indicating the requirement of magnesium for the ATP response. As magnesium binds ADP (red), the signal does not increase, indicating magnesium in the binding site, when bound to ADP, does not lead to a maximal fluorescence response. As magnesium is added to the ATP and ADP mixture (blue), low levels of magnesium lead to a half maximal response (as magnesium binds to ATP); we conclude that higher magnesium levels chelate ADP, which then leaves the binding site resulting in a maximal fluorescence response.

Nature Methods: doi: 10.1038/nmeth.1288

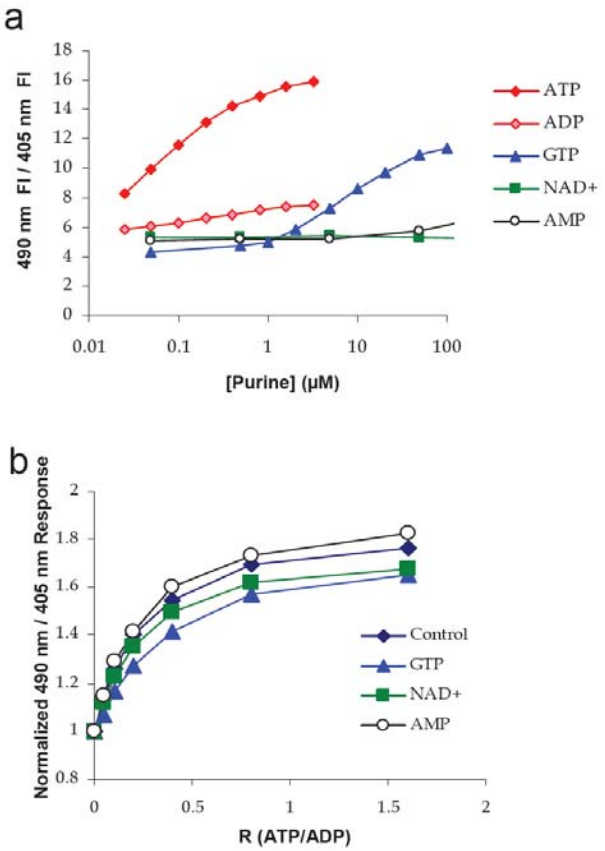

Supplementary Figure 3 | Sensitivity of the QV5 construct to other purine nucleotides. (**a**) Application of NAD^+ or AMP alone gave no increase in the signal from purified QV5 construct. Application of GTP shows a sub-maximal increase with an affinity of ~10 μM, indicating the response is 250 times more selective for ATP than for GTP. (**b**) The ATP:ADP ratio response is unaffected by the constant presence of 1 mM NAD^+ or AMP (with [ADP] = 0.5 mM). Competition with 1 mM GTP may cause a slight reduction in the ATP:ADP affinity.

Nature Methods: doi: 10.1038/nmeth.1288

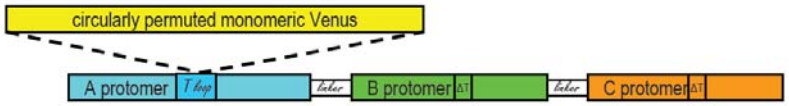

cpmVenus insertion:	$RYRGREY_{51}$ – SAG – *YNSD … KLEYN* – GT – $I_{52}VD$
A-B linker:	$TKEEG_{108}$ – ASGGGSGGGGASG – M_1KKVE
ΔT loop (B & C protomers):	$SEVKGR_{36}$ – GAGGG – $D_{54}LIPK$
B-C linker:	$TKEEG_{108}$ – ASGGGGGSGGASG – M_1KKVE

Supplementary Figure 4 | Construction of a tandem trimer version of the sensor. A single gene was constructed, encoding a tandem trimeric GlnK1 with a circularly permuted monomeric Venus inserted only in the first protomer. The first protomer is full length, with cpmVenus inserted between positions 51 and 52. In the sequence diagram, numbered subscripts indicate positions in monomeric wildtype GlnK1; black residues indicate linker sequences. The second and third protomers (labeled B and C) have a deletion of the T-loop region, as shown. When expressed in bacteria, the sensor has an N-terminal his-tag (sequence is MKHHHHHHHGAS) preceding the normal N-terminal methionine). The full-length sensor, without the his-tag, is 579 amino acids in length.

Nature Methods: doi: 10.1038/nmeth.1288

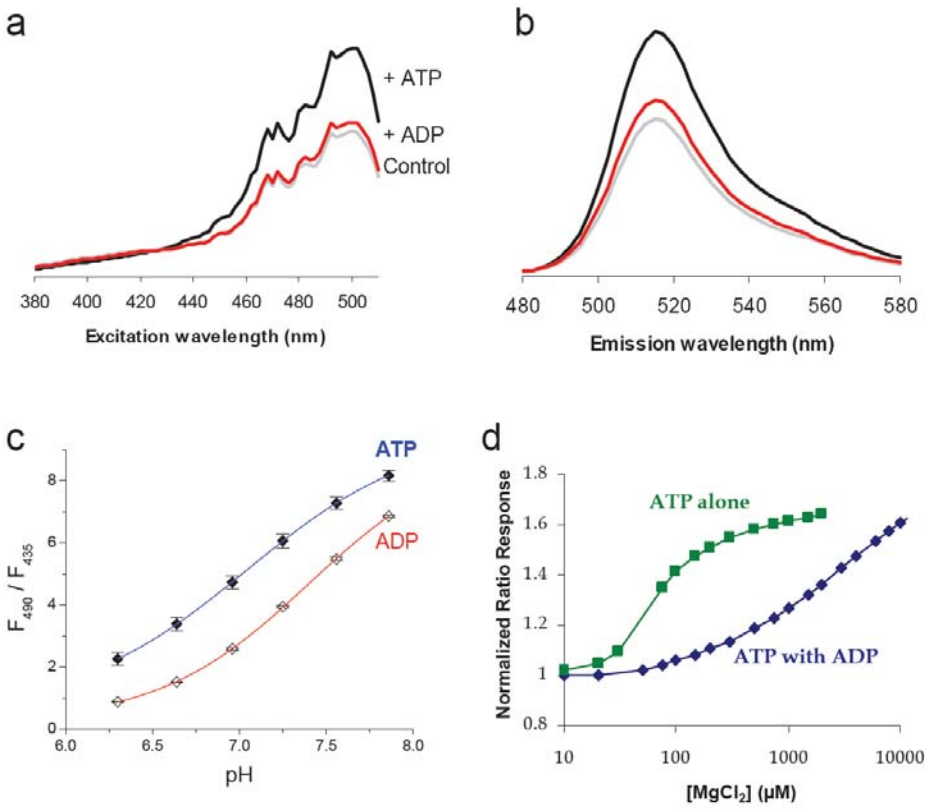

Supplementary Figure 5 | Spectral properties of Perceval. (**a**) Excitation spectra of purified Perceval during control conditions (gray) and following addition of 10 μM ADP (red) or 50 μM Mg-ATP (black), emission at 530 nm. ATP addition leads to an increase in the 490 nm peak and a decrease in the 405 nm peak. (**b**) The shape of the emission spectra, from control (gray) to ADP bound (red) or ATP bound (black) does not change, excitation wavelength 460 nm. (**c**) Perceval exhibits similar pH sensitivity (compare with **Suppl. Fig. 1**) to the original QV5 construct. Blue and red lines represent fits to data that are used for cellular pH calibration (**Fig. 5**). (**d**) Magnesium sensitivity of Perceval (compare with **Suppl. Fig. 2**) is also comparable to the original QV5 construct. $MgCl_2$ was added to a solution that contains ATP alone (sodium salt, 10 μM, Green symbols) or a mixture of ATP and ADP (10 μM and 50 μM respectively, Blue symbols).

Nature Methods: doi: 10.1038/nmeth.1288

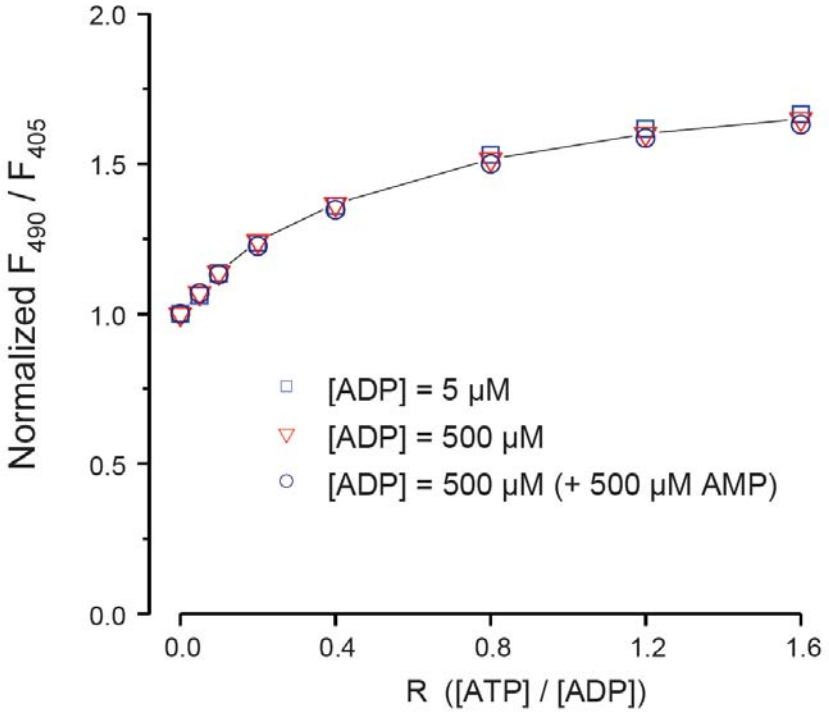

Supplementary Figure 6 | Response properties of Perceval. As seen for QV5 in **Figure 2** of the main paper, Perceval responds to the ATP:ADP ratio over a wide range of absolute concentration (shown here for [ADP] = 5 µM and 500 µM). The presence of 500 µM AMP has no effect on the response.

Nature Methods: doi: 10.1038/nmeth.1288

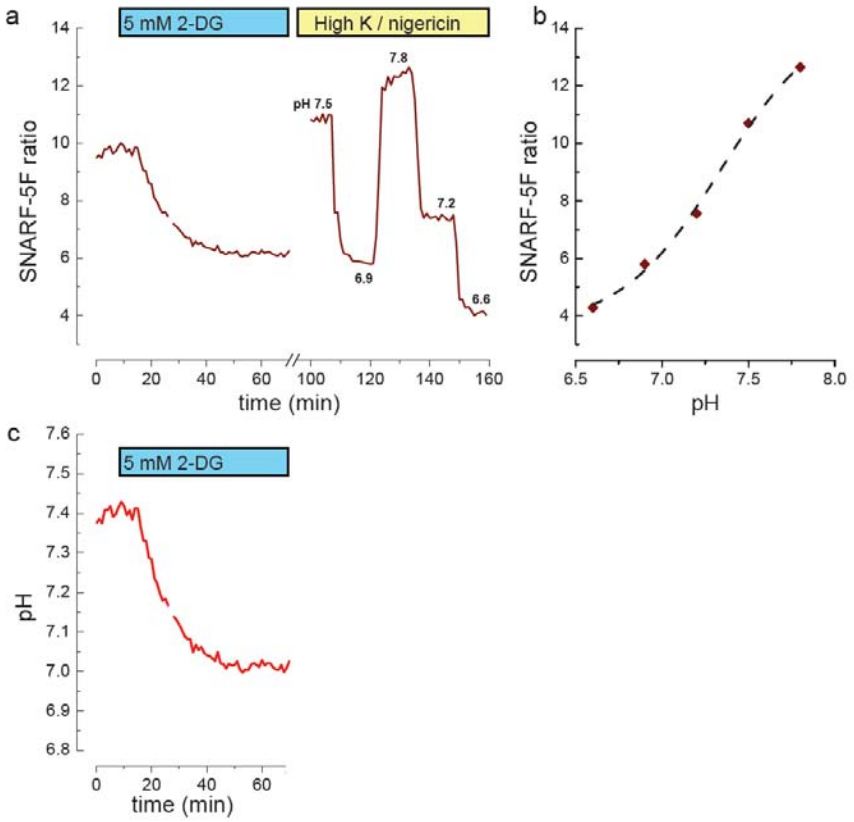

Supplementary Figure 7 | pH calibration using nigericin (a) Raw SNARF-5F signal for the experiment described in **Fig. 5a**. Application of 5 mM 2-DG leads to a decrease in SNARF-5F signal (indicating an intracellular acidification). Following a 30 minute incubation in a high potassium solution containing the ionophore nigericin (pH 7.5), the SNARF-5F signal is calibrated by washing in high K solutions of varying pH (in the constant presence of nigericin). **(b)** The standard SNARF-5F values are plotted against pH, and the data are fit with a sigmoid function which is used to calibrate the experimental SNARF-5F values to pH values in panel **(c)**.

Nature Methods: doi: 10.1038/nmeth.1288

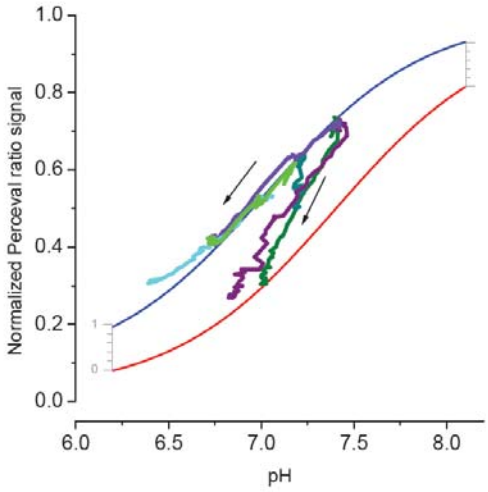

Supplementary Figure 8 | pH correction of 2DG and pH-control experiments As in Figure 5, experiments were performed either with wash-in of 5 mM 2-DG (dark green, blue and purple) or with exchange of extracellular solution to lower pH (light green, blue and purple). As in **Figure 5c**, the normalized Perceval signals from each experiment are plotted against calibrated pH values determined from concurrent SNARF-5F measurements.

Nature Methods: doi: 10.1038/nmeth.1288

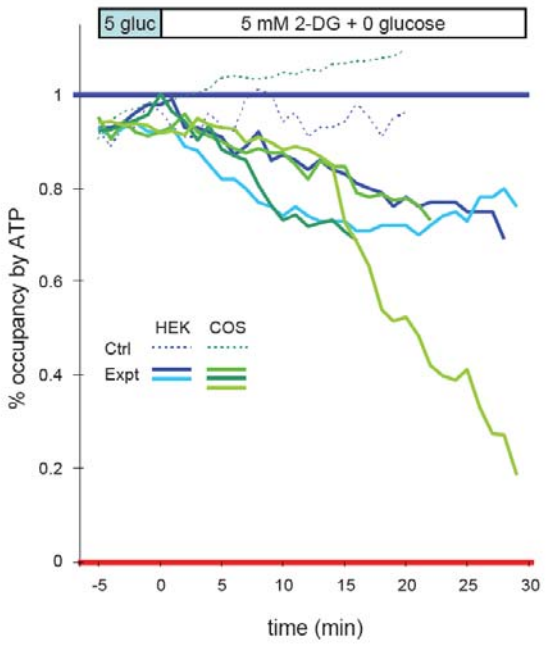

Supplementary Figure 9 | Comparable response of sensor in HEK293 and COS7 cells.

The pH-corrected Perceval occupancy is shown for control experiments in 5 mM glucose (dotted lines), and for experiments in which 2-deoxyglucose was substituted for glucose. Experiments on individual HEK293 cells are shown in blue colors and COS7 cells in green colors.

Nature Methods: doi: 10.1038/nmeth.1288

Supplementary Figure 10 | Perceval DNA and protein sequences.
The complete DNA coding sequence and protein sequence of Perceval.

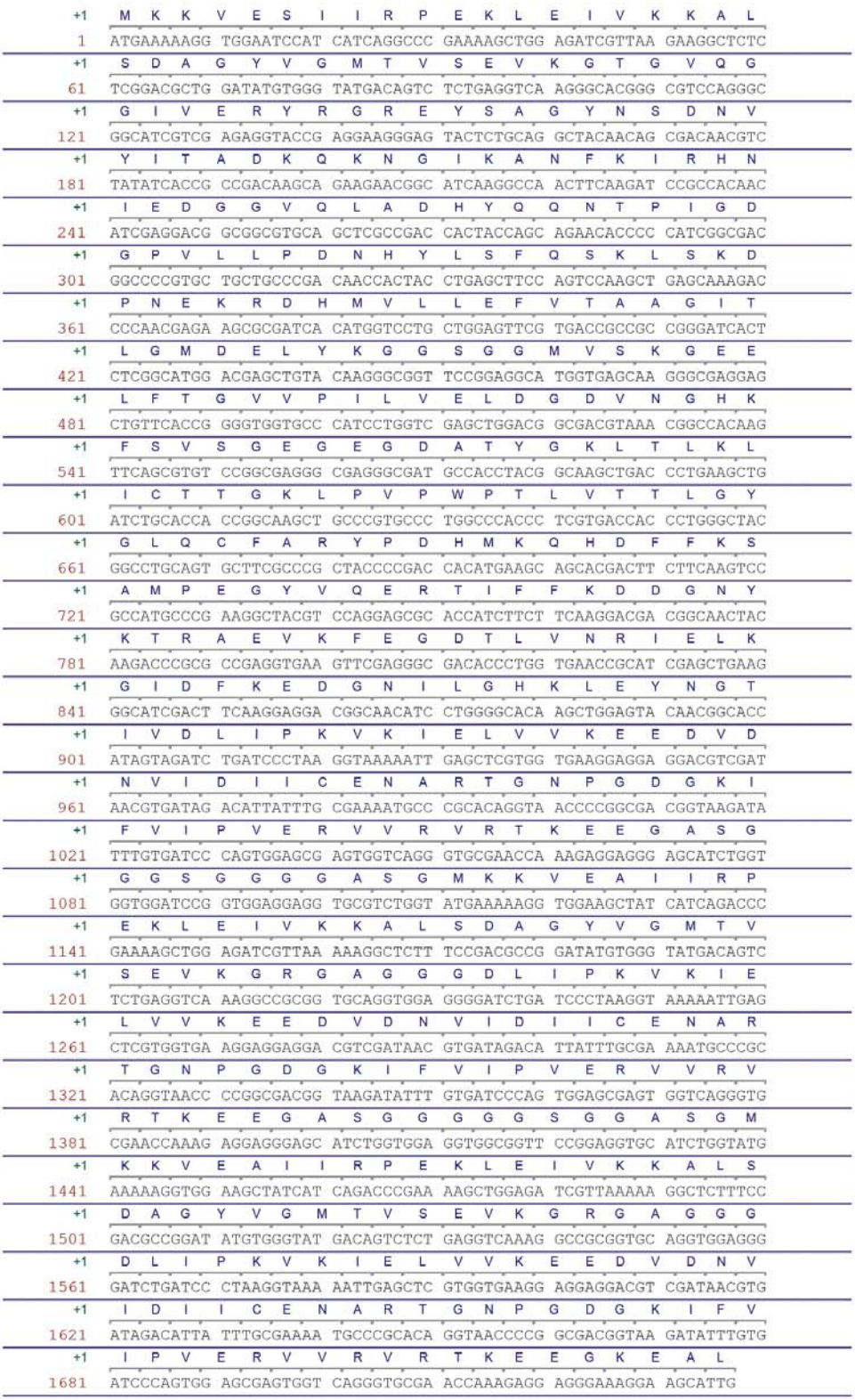

Nature Methods: doi: 10.1038/nmeth.1288

SUPPLEMENTARY RESULTS

A detailed explanation of the ratio-sensing behavior of the sensor

The GlnK1 – cpmVenus construct QV5 has two key properties: 1) It binds both ATP and ADP with extremely high affinity, with its affinity for ATP about 5-fold higher than that of ADP; and 2) ATP, but not ADP, binding produces a maximal fluorescence response. A general model to describe ATP and ADP binding to the sensor is

$$S{\cdot}ADP \underset{ADP}{\rightleftharpoons} S \overset{ATP}{\rightleftharpoons} S^*{\cdot}ATP$$

where S indicates the sensor, bound to either ADP or ATP (with the asterisk identifying the ATP-bound state as maximally fluorescent). Because of its high affinity, at physiologic nucleotide levels the population of sensor in the unoccupied state (S) is vanishingly small. With this approximation, we can calculate the relative occupancy of just the two remaining states: the occupancy of S·ADP is proportional to [ADP] / K_{ADP} and the occupancy of S*·ATP is proportional to [ATP] / K_{ATP}. The fraction of sensor in the ATP-bound (high fluorescence) state is then:

$$f_{ATP\text{-}bound} = \frac{\frac{[ATP]}{K_{ATP}}}{\frac{[ATP]}{K_{ATP}} + \frac{[ADP]}{K_{ADP}}}$$

Multiplying the numerator and the denominator by (K_{ATP}/[ADP]) gives the simplified equation:

$$f_{ATP\text{-}bound} = \frac{\frac{[ATP]}{[ADP]}}{\frac{[ATP]}{[ADP]} + \frac{K_{ATP}}{K_{ADP}}} = \frac{R}{R + K_R}$$

where $\frac{[ATP]}{[ADP]} = R$ and $\frac{K_{ATP}}{K_{ADP}} = K_R$

For simplicity, we have defined the ratio of nucleotide concentrations as R, and the ratio of the affinity of the probe for ATP and ADP as K_R. We expect K_R to be an intrinsic feature of the sensor, so the fluorescent response is determined by the R, or ratio of ATP to ADP. The dependence takes the form of a familiar binding equation, where K_R is the value of the [ATP] / [ADP] ratio that produces a half-

Nature Methods: doi: 10.1038/nmeth.1288

maximal fluorescence response. The QV5 construct is five-fold more sensitive to ATP than ADP, so we predict $K_R \approx 0.2$. This corresponds well to the actual behavior (**Figure 2** in the main paper).

pH and chloride sensitivity of the ATP sensor

We found that, as for the other probes based on circularly permuted fluorescent proteins[1, 2], the fluorescence intensity of the QV5 construct was sensitive to changes in pH. Cuvette experiments on purified QV5 construct showed that when excited at 490 nm, the fluorescence intensity for each form of the sensor (nucleotide free, ADP-bound, half maximal ATP, and full ATP) had greatest intensity at alkaline pH, and then diminished as the solution was acidified (**Supplementary Figure 1**). This translates to a 490 nm / 405 nm ratio signal that also is highest at alkaline pH values. The fluorescence with 435 nm excitation also diminished with acidification, but at all pH's measured this signal was invariant with ATP and ADP occupancy (although there was some change in fluorescence when the binding site was vacant, in the absence of any nucleotide).

The fact that alkaline pH leads to increased fluorescence is seen for most GFP-based fluorescent proteins, as protonation of the fluorescent protein's chromophore leads to a quenching of the fluorescence[3, 4]. With the QV5 construct, although the absolute intensity of the fluorescence is altered by pH, the response to ATP is relatively insensitive to changes in pH. This is evident from the fact that the curves for the different states of the sensor (**Supplementary Fig. 1b,c**) are approximately parallel in the range of cellular pH, indicating that the response to ATP does not change significantly across varying pH values. This does not indicate that pH should be of no concern (the fluorescence and ratio are still very much pH sensitive); it does mean, however, that changes in ATP:ADP can still be measured, even at different pH levels. Additionally, if the changes in pH are identified, then the sensor signal can be corrected for such changes.

We next assayed for any effect that changes in chloride might have on the responsiveness of the QV5 construct, as other FP's can exhibit chloride sensitivity[5]. We found that although a change in chloride concentration from 0 to 100 mM quenched the overall fluorescence signal of the QV5 construct by about 20% (**Supplementary Fig. 1d**), the ratio and responsiveness to ATP remained unchanged.

Correcting for changes in intracellular pH

Glycolytic inhibition can lead to a change in intracellular pH as well as energy charge (see the pH change in **Fig. 5a** of the main paper). By measuring the pH simultaneously with the Perceval signal

Nature Methods: doi: 10.1038/nmeth.1288

(using the pH indicator SNARF-5F), we were able to use the known pH dependence from the cuvette measurements to isolate the ATP:ADP signal from any pH-induced changes in fluorescence.

To correct the Perceval signal for pH, the Perceval signal was plotted against pH (**Fig. 5** and **Supplementary Fig. 8**). The pH sensitivity curves of the ATP-bound and ADP-bound sensor from the cuvette experiments were scaled using a single factor and we made the assumption that the sensor is near the fully ATP bound state at the beginning (fully-fed portion) of an experiment (in this case we assumed ATP:ADP = ~4, which corresponds to an occupancy of ~0.93). For each point in time, the Perceval signal can then be adjusted to where it falls between the maximum [ATP-bound] curve (set to a value of 1) and the minimum [ADP-bound] curve (set to 0).

To validate this method of pH correction, we also performed a pure pH challenge to HEK cells expressing Perceval and loaded with SNARF-5F. By lowering the extracellular pH, we were able to induce an intracellular acidification similar in magnitude to the pH change seen during metabolic inhibition. When the Perceval signal was pH-corrected, it remained around the maximally activated state (1.0) for the duration of the challenge.

Sensitivity of the GlnK1 – cpmVenus construct to Mg^{2+} ions

One of the primary differences in the crystal structure of the GlnK1 protein bound to ADP compared to that bound to ATP is the fact that the ATP is complexed with a Mg^{2+} ion whereas the ADP is not[6]. We therefore determined the effect of [Mg^{2+}] on the properties of the GlnK1 – cpmVenus QV5 construct (**Supplementary Figure 2**).

ATP We first determined whether magnesium is required for the full agonist effect of ATP. Addition of sodium ATP and chelation of any contaminating magnesium by addition of EDTA leads to the same submaximal fluorescence response seen with ADP (**Supplementary Fig. 2**, *green squares*). This leads us to conclude that free ATP likely acts as an incomplete agonist, in a similar manner to ADP. Subsequent addition of magnesium to the ATP solution led to a maximal response, so we conclude that the full fluorescence response is due to Mg-ATP binding. These results are compatible with the conclusion of Yildiz et al.[6] that the Mg^{2+} ion bound together with ATP is essential for stabilizing the closed state of the T-loop.

Nature Methods: doi: 10.1038/nmeth.1288

ADP The affinity of ADP for Mg^{2+} is much weaker than that of ATP, and it seemed possible that the sensor might be simply a Mg^{2+} sensor whose affinity depended on which nucleotide was bound. To investigate the possibility that a maximal fluorescence effect could be produced by Mg^{2+} in the binding site – regardless of whether ATP or ADP is bound -- we added potassium ADP to the sensor in the absence of any free Mg^{2+}. This gave a response identical to the Mg-ADP response seen in control experiments. To investigate the effect of Mg^{2+} on the ADP-bound sensor, we then added $MgCl_2$ to the solution (**Supplementary Fig. 2**, *red circles*). If Mg^{2+} bound to the ADP-bound sensor could produce a maximal response, then we would expect a curve with a response similar to what we saw with the Mg^{2+} addition to ATP (but with higher Mg^{2+} concentrations required due to the lower Mg^{2+} affinity of ADP). We observed the opposite result: upon $MgCl_2$ addition, there was a slight decrease in the fluorescent signal. We conclude that Mg^{2+} plus ADP does not produce the same maximal response as Mg-ATP.

Finally, we investigated whether Mg-ADP competes with free ADP, free ATP and Mg-ATP for GlnK1 binding. To do this, we took advantage of the different relative affinities of ATP and ADP for Mg^{2+}. By adding $MgCl_2$ to a mixture of ATP and ADP, we were able to predict significantly different outcomes for whether Mg-ADP is competing for the site or not. In each case, as we add $MgCl_2$ we should see a fast increase in fluorescence as Mg^{2+} binds to the high affinity ATP and produces a response proportional to the ATP:ADP ratio. If Mg-ADP binds in the pocket and acts identically to free ADP, then we should see no further effect on the fluorescence as Mg^{2+} binds to ADP (at higher concentrations of $MgCl_2$ due to its lower affinity). If, however, Mg-ADP does not bind to the site, as we increase the $[Mg^{2+}]$, we should see an increase in the signal as the free [ADP] is lowered by the Mg^{2+}. This second scenario is what the data show (**Supplementary Fig. 2,** *blue diamonds*): as Mg^{2+} was added to the solution, the response appeared more and more like ATP alone rather than as a mixture of ATP and ADP.

In summary, it appears that only Mg-ATP is capable of producing the conformational change that leads to the maximal fluorescence change in our sensor. The non-Mg^{2+}-bound ATP and ADP species compete with Mg-ATP and produce only a small change in fluorescence, while Mg-ADP does not change fluorescence or compete for binding sites.

Nature Methods: doi: 10.1038/nmeth.1288

SUPPLEMENTARY METHODS

Random library construction. A pair of long oligonucleotides with complementary 3′ ends was used to synthesize the N-terminal (pre-*Kpn*I site) or C-terminal (post-*Bgl*II site) coding sequence of GlnK1. Selected sites in each oligonucleotide were synthesized using a doped mixture of nucleotides, corresponding to 97% of the wild-type nucleotide and 1% each of the other nucleotides. For each section of the coding sequence, the two oligonucleotides (each one constituting a pool of mutant sequences) were combined, annealed, and subjected to a single primer extension reaction with Taq polymerase. The full-length product was cut with appropriate restriction enzymes and ligated into a previously prepared sensor construct. Each individual transformant colony was streaked onto a sector of a selective bacterial plate and allowed to grow before screening. Two libraries were prepared, one with mutations in the N-terminal half and the other with mutations in the C-terminal half. Each library pool had approximately 30 base sites with potential mutations, so that the average nominal mutation rate was approximately one mutation per colony.

Materials. Oligonucleotides were purchased from Integrated DNA Technologies (Coralville, IA), and custom gene synthesis was performed by Genscript (Piscataway, NJ; web:www.genscript.com).

Protein expression and purification. Cuvette experiments: To eliminate coassembly with native GlnK and GlnB subunits, his$_7$-tagged proteins were expressed in the *ΔglnB*, *ΔglnK* strain UNF3435 (ref. 8) generously provided by Mike Merrick, John Innes Centre, Norwich, UK. Bacteria were grown in aerated liquid culture for 24 hours at 37°C, and then transferred to room temperature for an additional 24 hours. Bacteria were then centrifuged and lysed with the CelLytic B reagent (Sigma). Proteins were purified using a Ni-NTA Spin Kit (QIAGEN, Valencia, CA) according to manufacturer's instructions. 96 well plate experiments: Individual colonies of bacteria were picked and streaked onto sectors of agar plates. Following 24 hours at 37°C, plates were transferred to 4°C, and incubated for 4 to 7 days to allow protein expression. Bacteria were then transferred from the sector of the agar plate to a well in a 96 well plate and resuspended in 2xYT media. The bacteria were then transferred to a 96 well iLAP plate (H9412 from Sigma, St. Louis, MO) for lysis and Ni^{2+} chelate binding and were incubated at 4°C overnight. The wells were then washed according to manufacturer's instructions and the proteins were eluted with the standard MOPS buffer (see recipe below), with the addition of 20 mM imidazole and 0.1% bovine serum albumin (BSA), pH 7.3 for 1 hour at room temperature. The proteins were then transferred to a 96 well plate (Corning Costar, Lowell, MA) that had been blocked with the BSA solution overnight.

Nature Methods: doi: 10.1038/nmeth.1288

Fluorometry. Cuvette Experiments: Aliquots of purified sensor protein were added to a cuvette containing 100 mM MOPS, 50 mM KCl, 5 mM NaCl, and 0.5 mM $MgCl_2$, pH 7.3 with KOH, unless otherwise noted. All nucleotides were added with Mg^{2+} concentration calculated to remain at 0.5 mM free Mg^{2+} (buffer calculations were based on the stability constants from ref. 9 and confirmed in several cases by fluorescence measurements with mag-fura-2). Fluorescence was measured using a Fluorolog-3, HORIBA Jobin Yvon (Edison, NJ). For all excitation experiments, slit widths were set at 2 nm for excitation wavelength and 10 nm for emission wavelength. For excitation spectra, the excitation range was 380 nm to 510 nm, with readings taken every 2 nm. Emission wavelength was 530 nm (slit width 5 nm) with an integration time of 1 s. For all other excitation data, measurements were taken at 405, 435, and 495 nm, with emission read at 520 nm. For each point, 3 scans, each with a 0.3 s integration time, were averaged. For kinetic determination, the excitation wavelength was 500 nm, emission at 525 nm, integration time 0.3 s, samples taken with a 1 s interval.

Cellular imaging. Human embryonic kidney 293 cells (HEK293) and COS-7 (American Type Culture Collection, Manassas, VA) were transiently transfected with a Perceval expression plasmid using electroporation. For experiments using SNARF-5F, 10 μM of the acetomethoxy ester form of the dye (Invitrogen, Carlsbad, CA) was loaded into the cells for 30 minutes prior to imaging in a dye-free solution. During imaging, the solution supply was constantly bubbled with 95% air and 5% CO_2 (calculated to give a pH of 7.3) and delivered through a flow-through heater (Warner Instruments, Hamden, CT) at a temperature of 31–33°C. Unless otherwise specified, the extracellular solution was composed of (in mM): 129.5 NaCl, 25 $NaHCO_3$, 10 D-glucose, 2.5 KCl, 1.25 NaH_2PO_4, 2 $CaCl_2$, and 1 $MgCl_2$. In experiments with 2-deoxyglucose, 5 mM 2-deoxyglucose was substituted for 10 mM glucose.

Imaging was performed with a pco (Kelheim, Germany) Sensicam QE CCD camera mounted on an Olympus Optical (Tokyo, Japan) BX51 upright microscope equipped with a 60x, 0.9 numerical aperture (NA) objective. A rapid wavelength switching monochromator (Polychrome IV; T.I.L.L. Photonics, Gräfelfing, Germany) with a 12.5 nm slit width was used for fluorescence excitation in conjunction with a 515 nm dichroic mirror (515DCXR) and a 535/25 nm band pass filter (D535/25) for collecting Perceval fluorescence emission. The SNARF-5F signal was obtained by exciting at 540 nm and alternating between a cube containing a Q565LP dichroic mirror + D585/20 nm band pass filter and Q595LP dichroic mirror + HQ645/75 nm band pass filter. The ratio of these two emission wavelengths

Nature Methods: doi: 10.1038/nmeth.1288

reports the intracellular pH. All filters were purchased from Chroma Technology (Rockingham, VT). Backgrounds were subtracted from each image by taking the average of a cell-free region of the image and subtracting that value from each image prior to analysis.

pH control and calibration

For experiments where extracellular pH was modified, $NaHCO_3$ was lowered to 10 mM [pH 6.9] or 5 mM [pH 6.6] (sodium balanced with NaCl). For experiments in which SNARF-5F was used to determine intracellular pH, the SNARF-5F signal was calibrated by using the high K^+/nigericin method[7]; for an example of this calibration method, see **Supplementary Figure 7**. Calibration solution contained 5 µg/ml nigericin in a high [K^+] bathing solution: (in mM) 130 KCl, 10 NaCl, 2 $CaCl_2$, 1 $MgCl_2$, 10 MOPS, pH 7.8 with KOH. Additional pH solutions (pH 7.5, 7.2, 6.9 and 6.6) were made by adding MOPS in the acid form to the pH 7.8 solution.

REFERENCES

1. Nagai, T., Sawano, A., Park, E. S., & Miyawaki, A. Circularly permuted green fluorescent proteins engineered to sense Ca2+. *Proc Natl Acad Sci U S A* **98**, 3197–3202 (2001).
2. Belousov, V. V., Fradkov, A. F., Lukyanov, K. A., Staroverov, D. B., Shakhbazov, K. S., Terskikh, A. V., & Lukyanov, S. Genetically encoded fluorescent indicator for intracellular hydrogen peroxide. *Nat Methods* **3**, 281–286 (2006).
3. Brejc, K., Sixma, T. K., Kitts, P. A., Kain, S. R., Tsien, R. Y., Ormö, M., & Remington, S. J. Structural basis for dual excitation and photoisomerization of the Aequorea victoria green fluorescent protein. *Proc Natl Acad Sci U S A* **94**, 2306–2311 (1997).
4. Kneen, M., Farinas, J., Li, Y., & Verkman, A. S. Green fluorescent protein as a noninvasive intracellular pH indicator. *Biophys J* **74**, 1591–1599 (1998).
5. Nagai, T., Ibata, K., Park, E. S., Kubota, M., Mikoshiba, K., & Miyawaki, A. A variant of yellow fluorescent protein with fast and efficient maturation for cell-biological applications. *Nat Biotechnol* **20**, 87–90 (2002).
6. Yildiz, O., Kalthoff, C., Raunser, S., & Kühlbrandt, W. Structure of GlnK1 with bound effectors indicates regulatory mechanism for ammonia uptake. *EMBO J* **26**, 589–599 (2007).
7. Thomas, J. A., Buchsbaum, R. N., Zimniak, A., & Racker, E. Intracellular pH measurements in Ehrlich ascites tumor cells utilizing spectroscopic probes generated in situ. *Biochemistry* **18**, 2210–2218 (1979).

Nature Methods: doi: 10.1038/nmeth.1288

8. Arcondeguy, T., van Heeswijk, W.C, & Merrick, M. Studies on the roles of GlnK and GlnB in regulating *Klebsiella pneumoniae* NifL-dependent nitrogen control. *FEMS Microbiology Lett.* **180**, 263-270 (1999).
9. Martell, A.E., & Smith, R.M. NIST Standard Reference Database 46 Version 8.0; NIST critically selected stability constants of metal complexes. National Institute of Standards and Technology (2004).

Nature Methods: doi: 10.1038/nmeth.1288

Appendix III

Imaging intracellular pH in live cells with a genetically encoded red fluorescent protein sensor

Mathew Tantama [1], Yin Pun Hung [1], and Gary Yellen [1]

[1] *Department of Neurobiology, Harvard Medical School, 220 Longwood Avenue, Boston, Massachusetts 02115, USA*

Reproduced with permission from: Tantama M, Hung YP, Yellen G. (2011) Imaging intracellular pH in live cells with a genetically encoded red fluorescent protein sensor. *J Am Chem Soc*. 133(26):10034-10037.

Yin Pun Hung constructed the sensor, provided support designing experiments, and contributed preliminary data for Figures 1a, 1f, and 4.

JACS
JOURNAL OF THE AMERICAN CHEMICAL SOCIETY

COMMUNICATION

pubs.acs.org/JACS

Imaging Intracellular pH in Live Cells with a Genetically Encoded Red Fluorescent Protein Sensor

Mathew Tantama, Yin Pun Hung, and Gary Yellen*

Department of Neurobiology, Harvard Medical School, Boston, Massachusetts 02115, United States

Supporting Information

ABSTRACT: Intracellular pH affects protein structure and function, and proton gradients underlie the function of organelles such as lysosomes and mitochondria. We engineered a genetically encoded pH sensor by mutagenesis of the red fluorescent protein mKeima, providing a new tool to image intracellular pH in live cells. This sensor, named pHRed, is the first ratiometric, single-protein red fluorescent sensor of pH. Fluorescence emission of pHRed peaks at 610 nm while exhibiting dual excitation peaks at 440 and 585 nm that can be used for ratiometric imaging. The intensity ratio responds with an apparent pK_a of 6.6 and a >10-fold dynamic range. Furthermore, pHRed has a pH-responsive fluorescence lifetime that changes by ~0.4 ns over physiological pH values and can be monitored with single-wavelength two-photon excitation. After characterizing the sensor, we tested pHRed's ability to monitor intracellular pH by imaging energy-dependent changes in cytosolic and mitochondrial pH.

Intracellular pH plays a vital role in cell biology. pH modulates protein structure and function, and organelles such as lysosomes and mitochondria require proton gradients to function properly. Intracellular pH is also coupled to processes such as the cell cycle and apoptosis.[1,2] Currently, there are several small-molecule sensors of pH, but these indicators can suffer from leakage from cells and poor control over subcellular targeting.[3] There are also several genetically encoded pH sensors based on green fluorescent protein (GFP) variants or fluorescence resonance energy transfer between two proteins.[4] However, for multicolor imaging these GFP-based pH sensors have limited compatibility with GFP-based sensors of other analytes because of overlapping excitation or emission bands.[5] For example, we are interested in imaging neuronal energy metabolism with GFP-based genetically encoded ATP sensors.[6,7] Changes in energy metabolism often correlate with pH changes, and it would be useful to monitor both ATP and pH simultaneously. Critically, the ATP sensors, like many GFP-based probes,[8−10] are also pH sensitive. Thus, monitoring pH dynamics is also necessary to correct for pH artifacts. Unfortunately, there are no GFP-based pH sensors with wavelength requirements that are compatible with those of the ATP sensors. Although the development of red fluorescent proteins (RFPs) has greatly improved prospects for multicolor imaging,[5,11,12] until now there were no ratiometric RFP-based pH sensors.[13]

To this end, we developed pHRed, a genetically encoded sensor engineered from the long Stokes shift RFP mKeima. Excited-state proton transfer (ESPT)[14,15] was recently described in mKeima,[16] suggesting it could serve as a scaffold for engineering a sensor that is excitation ratiometric.[9,17] The mKeima-A213S mutant, dubbed pHRed, has proven useful for monitoring pH, and in this report we characterize pHRed purified in solution and expressed in neuroblastoma cells (Figure 1).

We first characterized pHRed purified in solution. pHRed's peak fluorescence emission occurs at 610 nm, and there are excitation peaks at 440 (protonated neutral chromophore) and 585 nm (anionic chromophore) (Figure 1a).[4,14] Acidification from pH 9 to 6 causes a 7-fold increase in the 585 nm peak intensity (F_{585}) and a 4-fold decrease in the 440 nm peak intensity (F_{440}); both peaks respond with a pK_a of 7.8 (Figure 1b). The intensity ratio (F_{585}/F_{440}) increases >10-fold with acidification and responds with a lower pK_a of 6.6 because the 585 nm peak has a greater absolute intensity change (Figure 1c, Supplemental Figure S1). The ratio response is also insensitive to differences in buffer ion composition (K^+, Na^+, Cl^-, Mg^{2+}, Ca^{2+}, HCO_3^-), oxidative stress (H_2O_2, dithiothreitol), and temperature (21−37 °C) (Supplemental Figure S1). Hence, pHRed is a specific sensor for monitoring pH.

To compare its brightness to mKeima with excitation at 440 and 585 nm, we measured the extinction coefficients (ε) and quantum yields (QY) of pHRed (Supplemental Figures S2 and S3 and Table S1). At pH 7.5, pHRed's ε_{440} is 1.7-fold lower and ε_{585} is 3.4-fold larger compared to mKeima. Likewise, pHRed's QY_{440} is 1.8-fold lower and the QY_{585} is 1.3-fold larger. As a result, at pH 7.5 the brightness ($\varepsilon \cdot QY$) of pHRed is 3-fold lower than mKeima at 440 nm but 4-fold higher at 585 nm.

The pH dependence of ε_{440} and ε_{585} correlates well with the differing pK_a's of the fluorescence intensity responses of pHRed (p$K_a \approx 7.8$) and mKeima (p$K_a \approx 6.6$) (Figure 1d). Interestingly, pHRed's QY_{585} is not strongly pH dependent, but the QY_{440} increases 3-fold between pH 6 and 9 (Figure 1e). The QY_{440} of mKeima is also pH dependent, increasing 1.4-fold from pH 6 to 9. pHRed generally has a lower QY_{440} than mKeima, but the difference decreases as pH increases. This might suggest that mKeima, with a lower pK_a, is closer to saturation in its QY_{440} pH response, but it may also be that the A213S mutation simply increases the rate of nonradiative decay of the 440 nm absorbing neutral chromophore in pHRed. The pH dependence of the QY_{440} itself is not likely due to a pH-dependent change in ESPT efficiency because we do not observe any green emission, as would be expected if pH-dependent ESPT were a mechanism (Supplemental Figure S4).[18]

Received: April 8, 2011
Published: June 01, 2011

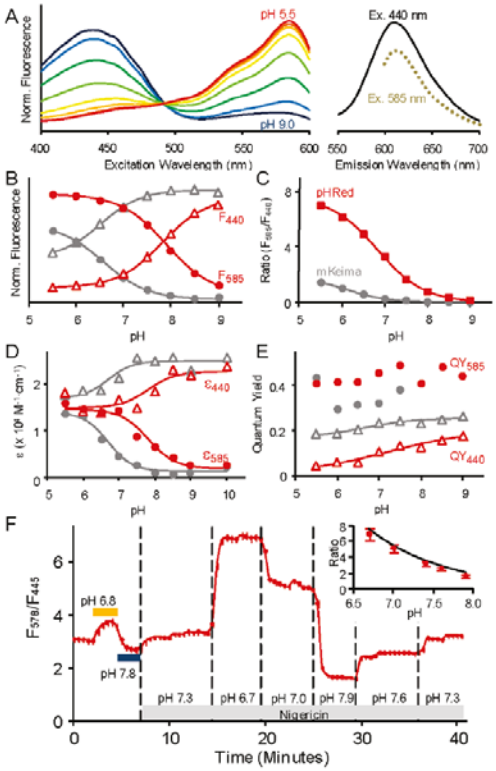

Figure 1. (a) Fluorescence excitation and emission spectra of purified pHRed in solution. pH response of the (b) 440 and 585 nm excitation peak intensities with 620 nm emission, (c) the F_{585}/F_{440} ratio, (d) extinction coefficients, and (e) quantum yields. (a,b) Fluorescence intensity is normalized to total integrated intensity. (b—e) mKeima data are shown in gray for comparison. (f) pHRed reports intracellular pH in live Neuro2A cells. Changes in extracellular pH without permeabilization caused minor changes to intracellular pH (horizontal bars). The protonophore nigericin was used to manipulate intracellular pH. $n = 43$ cells; bars indicate standard error. Inset: pH calibration in cells agrees well with purified protein (line).

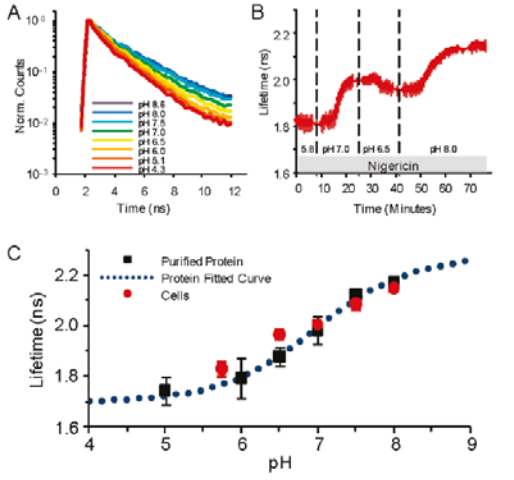

Figure 2. pH response of pHRed fluorescence lifetime (630 nm emission) with 860 nm two-photon excitation. (A) pH response of peak normalized fluorescence lifetime decays of purified pHRed in solution. (B) Intracellular pH in live Neuro2A cells imaged with FLIM. The nigericin method was used to manipulate pH. (C) pH response of pHRed fluorescence lifetime in cells ($n = 6$) and protein in solution ($n = 3$) in solution agreed well with an apparent pK_a of 6.9 ± 0.2, similar to the F_{575}/F_{440} intensity ratio response.

The spectroscopic data suggest that the A213S mutation also increases the apparent pK_a of pHRed relative to mKeima. It is possible that a serine hydroxyl at position 213 could interact with the adjacent carboxylate of E211. The crystal structures of mKeima[14,15] show that E211 directly interacts with the chromophore's imidazolinone moiety, and E211 may indirectly interact with S142 and D157 via waters and R193. This might provide a network by which a hydrogen-bonding interaction between S213 and E211 could cause a pK_a shift.

The purified protein characterizations demonstrate that pHRed is better suited than mKeima for intracellular pH sensing. pHRed has two well-matched peak intensities that facilitate ratio imaging, and it has a larger ratio response dynamic range that is also better matched to the physiological pH range. Therefore, we next characterized the pH response of the intensity ratio when pHRed is expressed in live cells. Heterologously expressed in Neuro2A cells, pHRed reports intracellular pH. To manipulate the intracellular pH, live cells were permeabilized using the K^+/H^+-ionophore nigericin and incubated in buffer with high extracellular KCl.[19] The pH dependence of pHRed's intensity ratio in cells correlated well with the pH response of purified protein in solution (Figure 1f).

We also found that pHRed exhibited a pH-dependent fluorescence lifetime that could be used to image intracellular pH using fluorescence lifetime imaging microscopy (FLIM) with near-infrared two-photon excitation. Imaging thick samples such as brain slices is greatly hindered by light penetration and light scatter, but this problem can be overcome by the use of two-photon excitation at infrared wavelengths.[17,20] However, two-photon excitation profiles are generally broad, and collecting an intensity ratio for pHRed would be challenging given the long wavelength of pHRed's second excitation peak. FLIM offers an alternative solution. Purified pHRed in solution can be excited in two-photon mode at a single wavelength of 860 nm,[17] and its fluorescence lifetime decreased upon acidification (Figure 2a). To test its pH response in cells, we again used the KCl-nigericin method to manipulate the intracellular pH of live Neuro2A cells expressing pHRed (Figure 2b). We found that the pH response of the fluorescence lifetime of pHRed expressed in cells correlated well with that of purified protein in solution (Figure 2c). The fluorescence lifetime of pHRed increased upon changing from pH 5 to 8 with a half-maximal response at pH 6.9 ± 0.2 ($n = 6$), making pHRed a well-tuned fluorescence lifetime sensor for intracellular pH. Furthermore, pHRed's lifetime changed by ~0.4 ns, a substantial lifetime difference that can be well detected in FLIM.[21,22] As with intensity ratios, the fluorescence lifetime is independent of expression levels. Thus, pHRed is a versatile probe that could be used to monitor pH in both thin and thick samples.

To test the utility of pHRed for live-cell microscopy, we used pHRed in two experimental regimes related to cellular energy

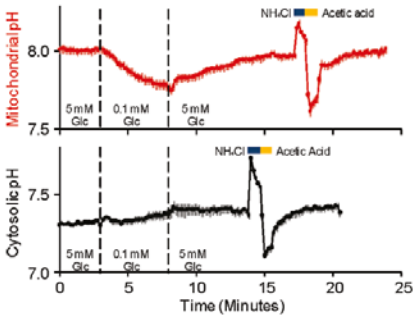

Figure 3. Decreased glucose concentration depletes mitochondrial substrates causing a loss of inner membrane potential, and COX8-pHRed reported a decrease in matrix pH (red, $n = 17$). Cytosolic pH reported by pHRed did not acidify when glucose was lowered (black, $n = 3$). At the end of each experiment, consecutive 10 mM NH_4Cl and 10 mM acetic acid pulses were used to verify that pHRed correctly reported an induced intracellular alkalinization and acidification, respectively. Mitochondrial matrix (pH 8.0) rested alkaline relative to cytosol (pH 7.3).

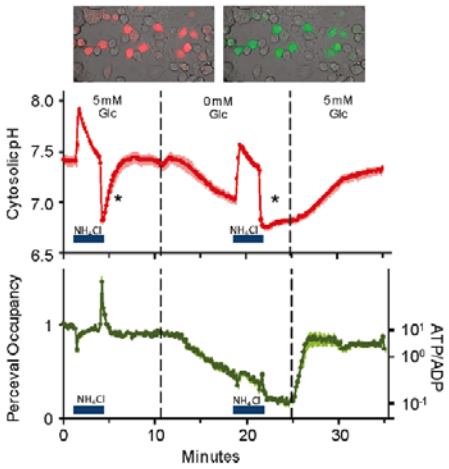

Figure 4. Coexpression of pHRed and Perceval for simultaneous imaging of the intracellular pH and the ATP:ADP ratio in live Neuro2A cells. Top: pHRed 629 nm (left) and Perceval 525 nm (right) emission in the same cells. Middle: In high glucose, cells rested at pH 7.4 and showed rapid recovery from an acid load induced by a 10 mM NH_4Cl prepulse (first asterisk). Complete glucose withdrawal caused acidification, and recovery from an acid load was attenuated (second asterisk). Bottom: Glucose withdrawal caused a decrease in ATP that was promptly reversed with refeeding. The Perceval signal was pH corrected using pHRed. Small errors in the correction remain at the start and end of the NH_4Cl pulses. $n = 14$.

metabolism: first, pHRed was targeted to the mitochondrial matrix and used to probe mitochondrial function; second, pHRed was used in conjunction with the sensor Perceval[6] to simultaneously monitor intracellular ATP and pH, demonstrating energy-dependent changes in cytosolic pH.

The cytochrome *c* oxidase subunit VIII (COX8) signal sequence was used to target pHRed to the mitochondrial matrix,[23,24] and glucose-dependent mitochondrial function was reported by COX8-pHRed. COX8-pHRed reported that the matrix was alkaline, resting at pH 8.0 in the presence of 5 mM extracellular glucose. When the extracellular glucose concentration was decreased from 5 to 0.1 mM, the matrix acidified, and this acidification could be reversed by increasing the extracellular glucose concentration (Figure 3). Without an appended signal sequence, pHRed expressed throughout the cell and reported that the cytosol did not acidify when extracellular glucose concentration was lowered, resting near pH 7.3 (Figure 3). The mitochondrial uncoupler *p*-trifluoromethoxy carbonyl cyanide phenyl hydrazone similarly caused an acidification of the mitochondrial matrix but not the cytosol (Supplemental Figure S5). Acidification of the mitochondrial matrix is consistent with a decrease in mitochondrial metabolism when glucose levels are decreased. Lowered glucose causes a decrease in substrates available to enter the tricarboxylic acid cycle and fuel the electron transport chain, causing a collapse of the inner membrane potential and mitochondrial pH gradient.[23,25] These data illustrate that targeted expression of pHRed can be used to monitor the pH of different organelles and their pH-dependent function.

We also demonstrated that pHRed can be used in multicolor experiments to simultaneously image intracellular ATP and pH and to facilitate correction for pH sensitivity of the ATP sensor. pHRed was co-expressed with Perceval, a sensor of the intracellular ATP:ADP ratio,[6] and the effect of acute glucose starvation on intracellular pH and ATP was monitored. As described above, lowering the extracellular glucose concentration to 0.1 mM causes mitochondrial acidification but not cytosolic acidification. These observations suggest that 0.1 mM extracellular glucose provides sufficient energy to maintain cytosolic pH despite attenuated mitochondrial function, at least for short periods of time in Neuro2A cells. In contrast, complete glucose starvation causes a cellular energy crisis that leads to oxidative stress, apoptosis, and loss of pH regulation.[2,26] Whereas increasing extracellular glucose can alkalinize the cytosol, complete glucose withdrawal can acidify the cytosol because ATP depletion attenuates the function of Na^+/H^+ exchangers, the Na^+/K^+-ATPase, H^+-ATPases, and other transporters that act together in H^+ homeostasis.[27,28,29−31] By co-expressing pHRed and Perceval, ATP depletion and its effect on intracellular pH could be simultaneously imaged. With 5 mM extracellular glucose ATP was high in Neuro2A cells, but ATP was quickly depleted with complete glucose starvation (Figure 4). The onset of ATP depletion correlated with the onset of intracellular acidification as the cells entered energy crisis (Figure 4). Additionally, recovery from acidification induced by a 10 mM NH_4Cl prepulse differed in high glucose/high ATP versus no glucose/low ATP conditions. In the NH_4Cl prepulse method, extracellular NH_4Cl causes intracellular alkalinization followed by a transient acidification when it is removed. This method is commonly used to assay the function of membrane transporters involved in H^+ homeostasis.[28] High ATP supported a rapid recovery from acidification, but low ATP prevented a rapid recovery phase (Figure 4). Furthermore, glucose re-feeding promptly raised intracellular ATP, but recovery from acidification was delayed until ATP reached near original levels reported by Perceval (Figure 4). These data are consistent with other studies showing that acid/base transporters and pH homeostasis require ATP for energy or as an allosteric modulator for transporter function.[28,30,31]

This multicolor imaging experiment also illustrates the utility of pHRed in providing a simultaneous pH signal that can be used

to correct the pH sensitivity of a green sensor. Sensitivity to pH is a critical problem for GFP-based sensors, particular circularly permuted GFP sensors, that can cause severe artifacts if not taken into account.[6,8,10] Perceval is pH-sensitive, and changes in intracellular metabolism and ATP:ADP ratio often occur concurrently with pH changes. Rather than requiring parallel experiments, simultaneous imaging of pHRed with Perceval allowed pH artifacts to be corrected on a cell-by-cell basis (Supplemental Figure S6). In this experiment, an empirical correlation between the green Perceval signal and the red pHRed signal was measured when cells were exposed to a mild pH manipulation not associated with a change in intracellular ATP. The empirical linear correlation was used to normalize Perceval for the pH changes reported by pHRed. This empirical method works well to remove the large pH artifacts observed with the uncorrected Perceval signal (Supplemental Figure S6). The ATP dynamics that were on the time scale of the metabolic changes monitored here were well corrected, despite small transient errors that remain in the corrected Perceval signal at the start and end of the ammonium pulse (Figure 4). Hence, pHRed facilitates imaging of multiple cellular parameters and can be valuable for providing a pH signal to correct for the pH-sensitivity of other sensors.

In conclusion, we engineered a new sensor called pHRed, a mutant of mKeima, that we used to image intracellular pH in live-cell microscopy. A pH sensor also using an RFP has been previously published, but this sensor provides intensity-based measurements that require corrections for expected photobleaching.[13] To our knowledge, this is the first sensor based on a single RFP that is excitation ratiometric. We demonstrated that pHRed uniquely allows us to image intracellular ATP and pH simultaneously because of its spectral compatibility with the GFP-based ATP sensor Perceval. We also demonstrated that in principle pHRed can be used in two-photon FLIM, potentially providing a new tool for imaging pH in thick samples or possibly even *in vivo*. With the great progress made in engineering RFPs and ESPT in RFPs,[17,32] this ratiometric sensing strategy could potentially be applied to create a variety of new sensor color variants and greatly enhance multicolor live-cell microscopy.

■ ASSOCIATED CONTENT

Supporting Information. Materials and methods, supplemental figures, tables, and discussion. This material is available free of charge via the Internet at http://pubs.acs.org.

■ AUTHOR INFORMATION

Corresponding Author
gary_yellen@hms.harvard.edu

■ ACKNOWLEDGMENT

We thank Tanya Abramson for technical assistance. We also thank Bernardo Sabatini, his group, and Rebecca Mongeon for providing instrumentation and assistance with two-photon FLIM and Ryohei Yasuda for providing FLIM software. We thank the Harvard NeuroDiscovery Center Optical Imaging Program for providing instrumentation for FLIM. M.T. is supported by a Postdoctoral Fellowship from the NIH (F32NS066613), and this work was supported by a research grant from the NIH (R01NS055031) to G.Y.

■ REFERENCES

(1) Casey, J. R.; Grinstein, S.; Orlowski, J. *Nat. Rev. Mol. Cell Biol.* **2010**, *11*, 50–61.
(2) Lagadic-Gossmann, D.; Huc, L.; Lecureur, V. *Cell Death Differ.* **2004**, *11*, 953–961.
(3) Han, J.; Burgess, K. *Chem. Rev.* **2010**, *110*, 2709–2728.
(4) Bizzarri, R.; Serresi, M.; Luin, S.; Beltram, F. *Anal. Bioanal. Chem.* **2009**, *393*, 1107–1122.
(5) Palmer, A. E.; Qin, Y.; Park, J. G.; McCombs, J. E. *Trends Biotechnol.* **2011**, *29*, 144–152.
(6) Berg, J.; Hung, Y. P.; Yellen, G. *Nat. Methods* **2009**, *6*, 161–166.
(7) Imamura, H.; Nhat, K. P.; Togawa, H.; Saito, K.; Iino, R.; Kato-Yamada, Y.; Nagai, T.; Noji, H. *Proc. Natl. Acad. Sci. U.S.A.* **2009**, *106*, 15651–15656.
(8) Belousov, V. V.; Fradkov, A. F.; Lukyanov, K. A.; Staroverov, D. B.; Shakhbazov, K. S.; Terskikh, A. V.; Lukyanov, S. *Nat. Methods* **2006**, *3*, 281–286.
(9) Miesenbock, G.; De Angelis, D. A.; Rothman, J. E. *Nature* **1998**, *394*, 192–195.
(10) Nagai, T.; Sawano, A.; Park, E. S.; Miyawaki, A. *Proc. Natl. Acad. Sci. U.S.A.* **2001**, *98*, 3197–3202.
(11) Shaner, N. C.; Steinbach, P. A.; Tsien, R. Y. *Nat. Methods* **2005**, *2*, 905–909.
(12) Verkhusha, V. V.; Lukyanov, K. A. *Nat. Biotechnol.* **2004**, *22*, 289–296.
(13) Johnson, D. E.; Ai, H. W.; Wong, P.; Young, J. D.; Campbell, R. E.; Casey, J. R. *J. Biol. Chem.* **2009**, *284*, 20499–20511.
(14) Violot, S.; Carpentier, P.; Blanchoin, L.; Bourgeois, D. *J. Am. Chem. Soc.* **2009**, *131*, 10356–10357.
(15) Henderson, J. N.; Osborn, M. F.; Koon, N.; Gepshtein, R.; Huppert, D.; Remington, S. J. *J. Am. Chem. Soc.* **2009**, *131*, 13212–13213.
(16) Kogure, T.; Karasawa, S.; Araki, T.; Saito, K.; Kinjo, M.; Miyawaki, A. *Nat. Biotechnol.* **2006**, *24*, 577–581.
(17) Piatkevich, K. D.; Hulit, J.; Subach, O. M.; Wu, B.; Abdulla, A.; Segall, J. E.; Verkhusha, V. V. *Proc. Natl. Acad. Sci. U.S.A.* **2010**, *107*, 5369–5374.
(18) Hanson, G. T.; McAnaney, T. B.; Park, E. S.; Rendell, M. E.; Yarbrough, D. K.; Chu, S.; Xi, L.; Boxer, S. G.; Montrose, M. H.; Remington, S. J. *Biochemistry* **2002**, *41*, 15477–15488.
(19) Thomas, J. A.; Buchsbaum, R. N.; Zimniak, A.; Racker, E. *Biochemistry* **1979**, *18*, 2210–2218.
(20) Kogure, T.; Kawano, H.; Abe, Y.; Miyawaki, A. *Methods* **2008**, *45*, 223–226.
(21) Esposito, A.; Gralle, M.; Dani, M. A.; Lange, D.; Wouters, F. S. *Biochemistry* **2008**, *47*, 13115–13126.
(22) Harvey, C. D.; Ehrhardt, A. G.; Cellurale, C.; Zhong, H.; Yasuda, R.; Davis, R. J.; Svoboda, K. *Proc. Natl. Acad. Sci. U.S.A.* **2008**, *105*, 19264–19269.
(23) Llopis, J.; McCaffery, J. M.; Miyawaki, A.; Farquhar, M. G.; Tsien, R. Y. *Proc. Natl. Acad. Sci. U.S.A.* **1998**, *95*, 6803–6808.
(24) Filippin, L.; Abad, M. C.; Gastaldello, S.; Magalhaes, P. J.; Sandona, D.; Pozzan, T. *Cell Calcium* **2005**, *37*, 129–136.
(25) Abad, M. F.; Di Benedetto, G.; Magalhaes, P. J.; Filippin, L.; Pozzan, T. *J. Biol. Chem.* **2004**, *279*, 11521–11529.
(26) Jelluma, N.; Yang, X.; Stokoe, D.; Evan, G. I.; Dansen, T. B.; Haas-Kogan, D. A. *Mol. Cancer Res.* **2006**, *4*, 319–330.
(27) Demaurex, N.; Romanek, R. R.; Orlowski, J.; Grinstein, S. *J. Gen. Physiol.* **1997**, *109*, 117–128.
(28) Demaurex, N.; Grinstein, S. *J. Exp. Biol.* **1994**, *196*, 389–404.
(29) Shepherd, R. M.; Henquin, J. C. *J. Biol. Chem.* **1995**, *270*, 7915–7921.
(30) Dechant, R.; Binda, M.; Lee, S. S.; Pelet, S.; Winderickx, J.; Peter, M. *EMBO J.* **2010**, *29*, 2515–2526.
(31) Nakamura, S. *Am. J. Physiol. Cell. Physiol.* **2004**, *287*, C97–C105.
(32) Piatkevich, K. D.; Malashkevich, V. N.; Almo, S. C.; Verkhusha, V. V. *J. Am. Chem. Soc.* **2010**, *132*, 10762–10770.

Imaging Intracellular pH in Live Cells with a Genetically-Encoded Red Fluorescent Protein Sensor

Mathew Tantama, Yin Pun Hung, Gary Yellen

Department of Neurobiology, Harvard Medical School, Boston, Massachusetts, 02115.

*gary_yellen@hms.harvard.edu.

Available Supporting Information Contains:

Methods

Supplemental Figure S1-S6 and Discussion

Supplemental Table S1

Supplemental References

Materials and Methods. Chemicals were purchased from Sigma-Aldrich unless otherwise noted. Cell culture media and supplements were purchased from Invitrogen unless otherwise noted. Error bars are standard errors.

Development of pHRed.

In the development of mKeima, an early-stage precursor exhibited two pH-dependent fluorescence excitation peaks at 452 and 580 nm, and the 452 nm peak was attenuated with four mutations: S61F, I92T, F158Y and S213A.[1] Of these mutations, the side chains of residues 92 and 158 are exterior facing, and residues 61 and 92 were further mutagenized in subsequent stages of development. Residue 158 is adjacent to D157, a residue important for ESPT;[2,3] however, the F158Y mutation is sterically conservative. In contrast, the side chain of residue 213 projects towards the chromophore,[2,3] and therefore we rationalized that reversing the S213A mutation would be a good starting point for recovering the 452 nm peak. Indeed, the mKeima-A213S mutant exhibits dual excitation peaks that respond ratiometrically to pH (Figure 1a). Because of proximity to the chromophore, we also conducted random mutagenesis of residues 60 and 61, but no improved variants were identified.

As for mKeima, the "reverse" pH dependence[3] of pHRed's fluorescence response is reminiscent of the behavior of the GFP-derived pHluorins,[4] and it is opposite the trend observed for *av*GFP.[5] In mKeima the reverse pH dependence is a result of chromophore interactions with S142 and D157.[3] The carboxylate of D157 stabilizes the protonated chromophore in a *trans* conformation, but under acidic conditions in which D157 is protonated, hydrogen bonding with S142 stabilizes the anionic chromophore in a *cis* conformation.[3] However, at alkaline pH D157 may also stabilize the *cis*-protonated chromophore, and the role of the isomerization is not clear.[2] Furthermore, residues S142 and D157 also provide a proton transfer network for ESPT following excitation of the protonated chromophore, and excitation of either ionization state results in red fluorescence emission.

A synthetic gene encoding mKeima (Genscript) was subcloned into the pRSetB (Invitrogen) bacterial expression vector, appending a 7xHis tag. Mutations were introduced by site-directed mutagenesis or by degenerate oligonucleotides and overlap PCR. Mutants were transformed into DH5α *E. coli* and grown in 96-well deep-well plates in 1.5 mL of YT media overnight at 37°C with shaking followed by room temperature shaking for 1 to 3 days. Bacterial pellets were collected by centrifugation, triturated in lysis buffer (1X CellLyticB, 100 mM MOPS, 50 mM KCl, 5 mM NaCl, 0.5 mM $MgCl_2$, pH 7.4 KOH), transferred to HisSelect Nickel-Affinity 96-well plates (Sigma), and incubated overnight at room temperature with shaking to capture protein. Capture plates were then washed three times with tris-buffered saline with 0.1% Triton-X100 and three times with MOPS wash buffer (Lysis buffer excluding CellLyticB). Plates were then incubated at room temperature with shaking for 4 to 6 hours in elution buffer (wash buffer plus 20 mM imidazole and 0.1% BSA). Clear bottom black 96-well plates (Nunc) were pre-blocked with elution buffer. Fluorescence of mutant proteins was screened using a Synergy 4 fluorescence plate reader (BioTek).

Initial Expression and Purification. pHRed containing an N-terminal 7xHis tag was expressed in DH5α cells as described above except scaled to a 10 to 30 mL culture volume. Protein was purified using the Qiagen NiNTA Quick Spin Columns according to manufacturer instructions. Eluate was dialyzed into storage buffer (10 mM HEPES, 120 mM KCl, 10 mM NaCl, 0.5 mM $MgCl_2$, 20% glycerol, pH 7.4 KOH) with two buffer changes at 4°C, stored at -20°C to 4°C for use within 5 days or stored at -80°C for later use.

Initial Characterization of Purified pHRed in Solution. For pH titrations buffer contained 10 mM of acetate, MES, MOPS, Bicine, and CHES and 100 mM of NaCl (pH with NaOH) or KCl (pH with KOH) or K·Gluconate (pH with KOH). Protein samples were diluted 20 to 40 fold to ~2 μM, and fluorescence was measured in a fluorescence plate reader or in a cuvette spectrofluorometer for more detailed spectra (Fluoromax, Horiba Jobin Yvon). To test for interferences, consecutive additions of $MgCl_2$, $CaCl_2$, H_2O_2, and DTT were made to samples diluted into NaCl, KCl, or K·gluconate buffers. For temperature dependence, samples were measured in sealed plates to prevent evaporation. Fluorescence was measured at room temperature (21°C) first. Temperature was then consecutively increased to 25°C, 31°C, and 37°C, and the samples and instrument were allowed to equilibrate before measuring fluorescence. For sensitivity to bicarbonate, solutions were titrated with $NaHCO_3$ from pH 4.9 to 8.2. Protein was diluted into bicarbonate buffers and fluorescence measured within 5 minutes of pH measurement to minimized pH variations in the absence of a controlled CO_2 atmosphere. For filter based plate reader measurements, 440/20 nm and 575/15 nm excitation and a 635/32 nm emission filters were used.

Expression in Neuro2A Cells. pHRed was subcloned into the GW1 (British Biotech) mammalian expression vector. DNA was prepared from DH5α cells using Qiagen High Speed MaxiPrep

kits. Neuro2A (ATCC CCL-131) cells were cultured at 37°C in 5% CO_2 humidified air atmosphere in MEM media containing 10% bovine calf serum (Invitrogen) and passed every 3 to 4 days. For expression, cells were plated onto protamine coated 18 mm diameter, #1.5 glass coverslips (Thermo). Four to six hours later, cells were transfected using Effectene (Qiagen) according to manufacturer's instructions. The following day media was changed to low glucose DMEM containing 1% bovine calf serum and 10 μM all *trans*-retinoic acid to induced neurite extension. Cells were imaged 24 to 72 hours after media change.

Cell Treatments and Nigericin pH Calibrations. Cells were imaged in continuously flowing (2 mL/min) artificial cerebrospinal fluid (ACSF in mM: 130 NaCl, 4 KCl, 2 $CaCl_2$, 1 $MgCl_2$, 20 sucrose) buffered with 25 mM HEPES, pH 7.4 (NaOH) except for Figure 3 where ACSF was buffered with 25 mM $NaHCO_3$ bubbled with 5% CO_2/95% air. ACSF was warmed to 34±1°C with an inline heater placed just before the perfusion chamber except for FLIM experiments conducted at room temperature. Glucose was added to concentrations indicated in the text and osmotic balance was maintained with sucrose (~325 mOsmol to match complete DMEM culture media). For nigericin experiments, NaCl was replaced with KCl, and 2-5 μM nigericin was used.

Intensity Ratio Imaging. Cells were imaged on a Nikon Eclipse TE300 inverted microscope mounted with an Andor Revolution Differential Spinning Disk (DSD) unit for optical sectioning controlled by iQ software. Excitation light from a Prior Lumen Pro was passed through 445/20 nm, 482/18 nm, or 578/16 nm Semrock filters. The DSD unit contained a Chroma 59022bs dichroic, Semrock 492 nm short pass, Omega 490 nm short pass, and Omega 590 nm short pass filters. Excitation light was passed through Semrock 525/39 nm or 629/56 nm filters. In a typical experiment, images were taken in succession at 10 second intervals with 2x2 binning and 200 to 400 ms exposure times using a Nikon Plan Apo VC 20X/0.75NA dry objective. Background and bleed-through of Perceval fluorescence into the pHRed channel were subtracted before ratios were calculated. There is a minimal amount of bleedthrough (5%) of Perceval green fluorescence into the pHRed red channel when excited at the shared wavelength of 445 nm. Pixel-by-pixel ratios were calculated, regions or interest were drawn around cells, and average measurements were calculated with thresholding using ImageJ software.

Perceval is a dual excitation ratiometric sensor that responds to changes in the ATP:ADP ratio.[6] The F_{485}/F_{445} fluorescence intensity ratio (R) increases in response to increasing ATP:ADP with a half maximal response at ATP:ADP ~ 0.5. The occupancy of the sensor is calculated as $(R - R_{min}) / (R_{max} - R_{min})$. R_{min} and R_{max} are estimated at the end of *each* experiment in 0 or 25 mM glucose, respectively, and the ratios are pH-corrected as described below.

Two-Photon FLIM. Protein samples and cells were imaged on an upright microscope with a 10X dry objective modified for lifetime imaging built in house by G.Y. and Bernardo Sabatini. Samples were excited using a tunable Ti:Sapphire 80 MHz laser (Coherent, Chameleon Vision II), and a time-correlated single-photon counting board (Becker and Hickl SP-830) was used to measure fluorescence decays. Fluorescence emission was collected by a photomultiplier tube (Hamamatsu 47422) through a 700 nm long pass and 630/60 nm filters. Data was collected and analyzed using Matlab software provided by Ryohei Yasuda and Bernardo Sabatini and modified by G.Y. The empirical mean lifetimes were measured by averaging over a 9 ns window. The zero time offset for the averaging window was estimated to be the time of peak intensity as determined by fitting the fluorescence decays to a bi-exponential function convoluted with a Gaussian instrument response function. There was no difference in estimated zero time offsets using either a Gaussian instrument response function or an experimental response function. The fitting approach provides a robust automated method for determining the zero time offset and averaging window. The fitted lifetimes themselves were not used because the empirical mean lifetimes provide a fitting-independent measurement. These empirical mean lifetimes are plotted in Figures 2b and 2c.

Note that the pH changes in Figure 1f and Figure 2b differ in kinetics. This is an artifact of the different perfusion systems attached to the ratio imaging and FLIM instruments. Thus the difference in the rate of the pH-dependent ratio and lifetime changes reflects differences in solution exchange, not any fundamental photophysical peculiarity.

Spectroscopy for Extinction Coefficient and Quantum Yield Determinations. For spectroscopy, pHRed and mKeima proteins were expressed and purified as described above. However, proteins were dialyzed into a low buffering strength solution (5 mM MOPS, pH 7.3, 300 mM NaCl, 10% glycerol). For pH studies, the solutions contained 300 mM NaCl and 50 mM of one of the following buffers: MES, pH 5.5; MES, pH 6.0; MOPS, pH 6.5; MOPS, pH 7.0; MOPS, pH 8.0; Bicine, pH 8.5; Bicine, pH 9.0; CHES, pH 10.0.

The concentration of protein containing mature chromophore was measured in 1M NaOH. mKeima and pHRed have the same QYG-derived chromophore as DsRed. Alkaline denaturation of the protein exposes the chromophore, and hydrolysis of the chromophore acylimine produces a GFP-like chromophore. In agreement, both mKeima and pHRed exhibit 446 nm peak absorbance in 1M NaOH. The extinction coefficient of this chromophore measured for DsRed in 1M NaOH was close to that for GFP (ε_{446} = 4 x 10^4 $M^{-1} \cdot cm^{-1}$).[7] Therefore absorbance at 446 nm in 1M NaOH can be used to measure the concentration of mature chromophore.[8] Mature protein concentrations were measured at several dilution on several days, and protein concentrations were consistent. For direct comparison with literature values, total protein concentration of mKeima was determined by colorimetric bicinchoninic acid (BCA) assay. Comparison of the two methods indicate that ~60% of the mKeima protein contains mature chromophore, consistent with previously published reports.[2] Furthermore, the extinction coefficient determined using BCA-assayed total protein concentration values is ~15000 $M^{-1} \cdot cm^{-1}$ at pH 7.5, very consistent with other published reports where the extinction coefficient was also determined with respect to BCA-assayed total protein concentration.[1,9] In order to provide an accurate description of the mature mKeima and pHRed we henceforth used the protein concentration determined by the alkaline denaturation method as others have.[8,10]

For pH-dependent extinction coefficient measurements, proteins were diluted in appropriate buffers at 3 or 4 different concentrations (~5-20 μM), and the extinction coefficients were calculated according to the Beer-Lambert equation.

For pH-dependent quantum yields, proteins were diluted in appropriate buffers to absorbances of 0.001 to 0.01, and the fluorescence vs. absorbance slopes were measured through 7 to 9 data points. For 440 nm excitation, mKeima at pH 7.5 was used as the reference standard (QY = 0.24).[1] For 585 nm excitation, sulforhodamine 101 in ethanol was used as the reference standard with correction for the difference in refractive index (QY = 0.95).[11]

Supplemental Figures, Tables, and Discussions.

pHRed's Fluorescence Intensity and Intensity Ratio (Related to Figure 1a-c) The maximal fluorescence intensity change with 575 nm excitation is of a larger magnitude than the maximal fluorescence intensity change with 440 nm excitation (Supplemental Figure S1). As a result the intensity ratio pH response is acid shifted. While both F_{575} and F_{440} respond to pH with a pK_a ~ 7.8, the F_{575}/F_{440} ratio responds with a pK_a ~ 6.6.

The same is true for mKeima fluorescence intensities, but for mKeima the fluorescence intensities respond to pH with a pK_a ~ 6.6. This causes the intensity ratio of mKeima to respond to pH with a pK_a < 6, a major reason why pHRed is better suited for monitoring intracellular pH compared to mKeima.

pH Response is Insensitive to Various Factors (Related to Figure 1a-c). The pH-dependent fluorescence of pHRed was insensitive to differences in buffer ion composition (Mg^{2+}, Ca^{2+}, K^+, Na^+, Cl^-, HCO_3^-), oxidative stress (H_2O_2, dithiothreitol), and temperature (pK_a(21°C)=6.6; pK_a(25°C)=6.7; pK_a(31°C)=6.7; pK_a(37°C)=6.7), so there should be minimal artifacts due to these factors (Supplemental Figure S1).

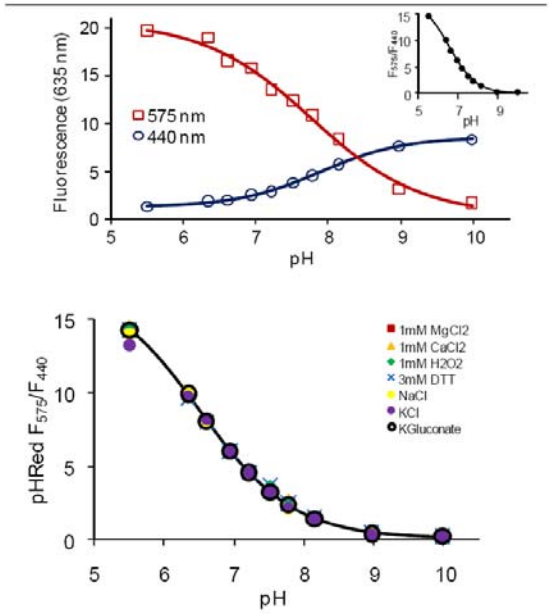

Supplemental Figure S1. Top: Scaled pH responses of pHRed fluorescence intensities. F_{575} and F_{440} both exhibit a pKa of ~7.8, but F_{575} changes nearly 2-fold more in magnitude than F_{440}, causing the ratio to reach half-maximal response at a lower pKa of 6.6 (inset). Bottom: The pH response of pHRed's F_{575}/F_{440} intensity ratio was not significantly affected by changes in buffer concentrations of Mg^{2+}, Ca^{2+}, Na^+, K^+, Cl^-, HCO_3^-, gluconate$^-$, hydrogen peroxide, or dithiothreitol (symbols overlay one another closely on the fitted solid black curve).

Photophysical properties of pHRed (Related to Figure 1a-e). Absorbance spectra were taken at 3-4 different protein concentrations at different pH to determine extinction coefficients (Supplemental Figure S2). At the end of each measurement, NaOH was added directly to the sample to a final concentration of 1M, and the 446 nm absorbance of the mature chromophore was measured. [7] This provided a direct measurement of protein concentration to minimize errors due to pipetting.

Quantum yields were measured by comparing the slopes of the fluorescence versus absorbance relationships. 7 to 9 data points were collected for each slope determination (Supplemental Figure S3).

The extinction coefficients, quantum yields, and brightness products of pHRed and mKeima measured in this study are listed in Supplemental Table S1.

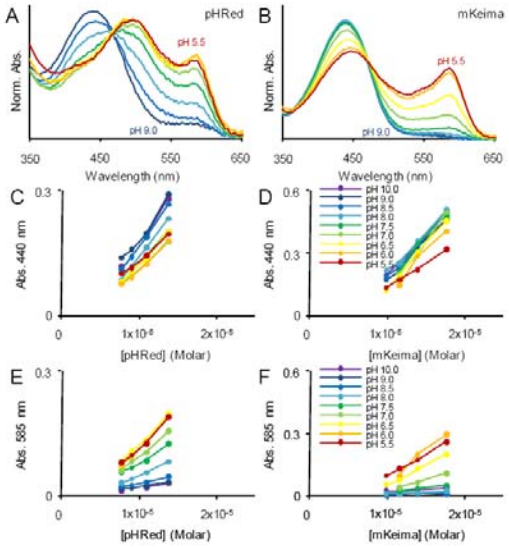

Supplemental Figure S2. pH dependence of the absorbance spectra of pHRed and mKeima. Extinction coefficients for absorbance at 440 and 585 nm were estimated by measuring absorbance spectra at 3 to 4 protein concentrations at pH 5.5 to pH 10.

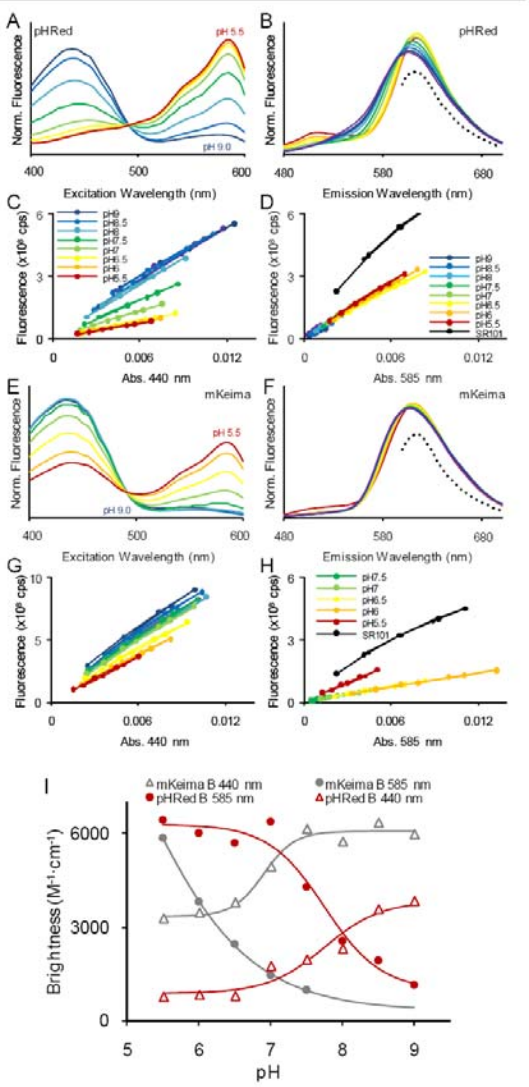

Supplemental Figure S3. pH dependence of the fluorescence excitation and emission spectra of (a-b) pHRed and (e-f) mKeima. Quantum yields with excitation at 440 nm or 585 nm were determined by collecting fluorescence versus absorbance relationships, and comparing slopes to reference standards (mKeima, pH 7.5 for QY_{440}; Sulforhodamine 101 for QY_{585}). The brightness is the product of the quantum yield and extinction coefficient. (c-d) pHRed. (g-h) mKeima.

Purity of pHRed. Nickel affinity purified pHRed and mKeima were analyzed by denaturing SDS-PAGE. Densitometry of the Coomassie stained gels indicated the 26 kDa band accounted for ~90% of the protein. 10% of the protein was attributed to bands at ~16 kDa and ~10 kDa. These bands are previously described C- and N-terminal fragments that result from hydrolysis of the acylimine in the chromophore and backbone scission.[5] No other bands were apparent.

We also looked for any green fluorescence from pHRed. The fluorescence spectra of purified pHRed showed that there is no green fluorescent component. Because maturation can be different when FPs are expressed in mammalian cells, we also looked for green fluorescence following transfection of pHRed in N2A cells. Fluorescence images were taken 1, 2, 3, and 4 days after transfection (normally cells are used 3 and 4 days after transfection). On day 1 no fluorescence was visible. On days 2 to 4, we imaged 50 to 300 cells each day, exciting at 445 nm and collecting fluorescence images at 525 nm and 629 nm. We compared pixel intensities of transfected cells versus untransfected cells. We clearly observe an increase in red fluorescence, but there is not a significant green fluorescence component that would indicate a green immature population.

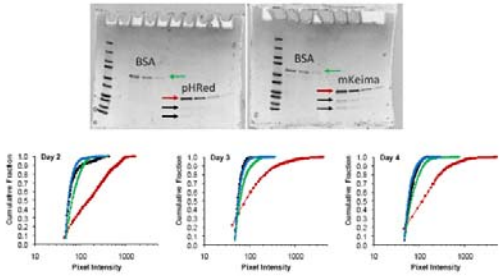

Supplemental Figure S4. Top: Densitometry following SDS-PAGE and Coomassie staining indicate both pHRed and mKeima were purified to at least 90% purity. Bottom: N2A cells were transfected with pHRed. Over time red fluorescence increased in transfected cells (red) versus autofluorescence from untransfected cells (black). There was not a significant green fluorescence in transfected cells (green) compared to autofluorescence of untransfected cells (blue).

pHRed Reported Dissipation of the Mitochondrial pH Gradient by FCCP (Related to Figure 3). COX8-pHRed reported acidification of the mitochondrial matrix induced by 1μM FCCP (Supplemental Figure S2, red trace, blue bar). This is consistent with the uncoupling action of FCCP which dissipates the mitochondrial inner membrane potential. Interestingly, oligomycin also caused a slight acidification which reached steady-state in ~1 min (yellow bar). This is contrary to the expected effect of oligomycin. Oligomycin would be expected to block the ATP synthase and proton translocation, causing an alkalinization of the mitochondrial matrix. These contrary observations could be due to non-specific effects of oligomycin or indicative that ATP synthesis is not strongly coupled to the inner membrane potential in Neuro2A cells. However, exploration of this phenomenon is beyond the scope of this paper. Neither oligomycin nor FCCP significantly affected cytosolic pH as reported by pHRed (black trace).

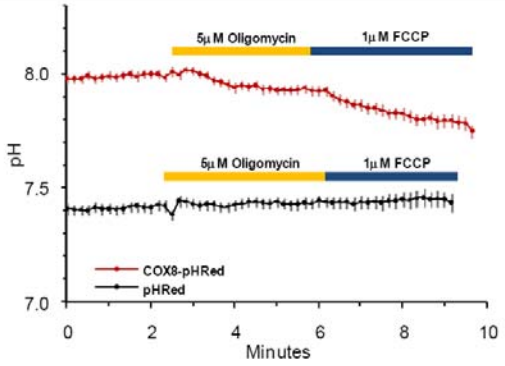

Supplemental Figure S5. pHRed expression in live Neuro2A reported on mitochondrial function. Expressed in the cytosol, pHRed indicated no change in intracellular pH in response to FCCP (blue bar). Targeted to the mitochondrial matrix, COX8-pHRed reported an acidification of the mitochondrial matrix with application of FCCP.

pH Correction of Perceval Using pHRed (Related to Figure 4). The ATP:ADP ratio reporter Perceval is pH-sensitive. Thus, changes in the Perceval ratio shows significant changes that are correlated with the pHRed signal changes. To correct for pH artifacts, an empirical linear correlation was measured between Perceval and pHRed ratios during a change in intracellular pH that does not significantly affect the intracellular ATP:ADP ratio. For example, minor changes to the extracellular pH or mild alkalinization by exposure to low concentrations of extracellular NH_4Cl are appropriate pH challenges. The linear correlation can be used in conjunction with the pHRed signal to extrapolate the expected changes in Perceval and thus normalize the Perceval ratio.

For example, Supplemental Figure S3 shows data from one cell extracted from Figure 4 of the main text. The uncorrected Perceval intensity ratio is strongly correlated to the pHRed intensity ratio, showing clear pH artifacts (Supplemental Figure S3ab). Using the NH_4Cl pulse in the presence of glucose when the intracellular ATP:ADP ratio is high and stable, data collected during this pH challenge show a strong linear correlation between Perceval and pHRed. Furthermore, data collected during the NH_4Cl pulse in the absence of glucose can be fitted with a near parallel line. These parallel fitted lines represent the extreme contours of the intracellular ATP:ADP ratio as reported by Perceval in its saturated and unsaturated states. Data points that are collinear along a contour have the same ATP:ADP ratio but differ in intracellular pH. When a time course of data points deviates between the two extreme contours, a real change in ATP:ADP occurred. In this experiment, extracellular glucose was withdrawn to deplete intracellular ATP. As a result, most points in the Perceval-pHRed space lie on the upper or lower fitted lines. Only when glucose was withdrawn did points (red) deviate from the top contour moving to the lower contour, indicating a real decrease in ATP:ADP. Likewise, when glucose was resupplied points, (blue) deviated from the bottom contour and moved back towards the top contour, indicating a real increase in ATP:ADP.

Operationally, the linear correlation from individual cells is used to normalize Perceval and minimize pH artifacts. The predicted change in Perceval due to pH is calculated using the pHRed signal and fitted parameters, and then Perceval is normalized to the predicted pH-only change. As expected, this method is not a perfect correction for pH sensitivity. An alternative method is to use the estimated pH and pre-determined pH-dependence of Perceval reporting parameters to absolutely correct the Perceval signal. However, in practice this method suffers from large propagated errors and also relies on predetermined parameters. The empirical method works very well in practice (and in simple simulations), and has the added benefit of using parameters determined from each experiment on a cell-by-cell basis.

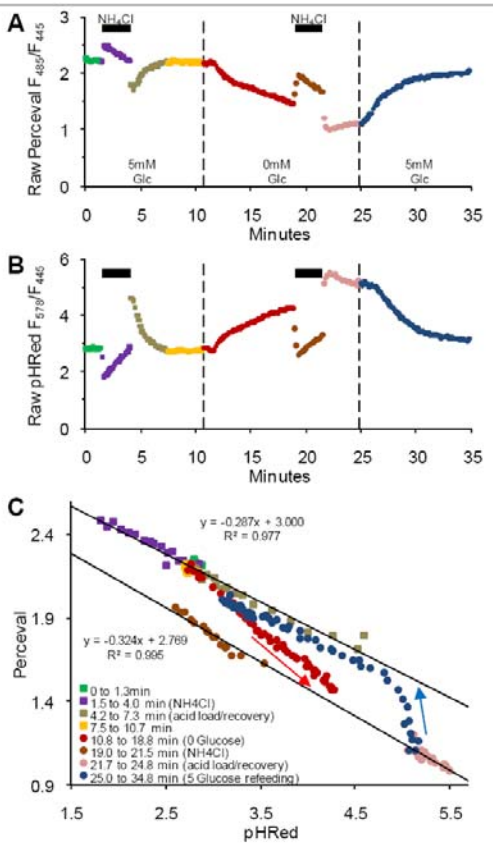

Supplemental Figure S6. Empirical correction of the pH-sensitivity of Perceval using pHRed from a live Neuro2A cell expressing both reporters. (A) Uncorrected Perceval ratio over time. 10 mM NH_4Cl pulses (black bars) were applied in the presence or absence of glucose. The fluorescence ratio trace is color coded to indicate time periods of interest throughout the figure. (B) pHRed ratio over time. (C) Data from (A) and (B) plotted as the Perceval ratio versus the pHRed ratio. Data during the NH_4Cl pulse in the presence of glucose provided a linear correlation between Perceval and pHRed (top solid black line). Data during the NH_4Cl pulse in the absence of glucose is fitted by a nearly parallel line (bottom black solid line) as expected. When glucose was withdrawn, the data points (red) deviate below the top fit, indicating a true decrease in intracellular ATP:ADP ratio (red arrow indicates progression over time). Conversely, when glucose was resupplied, the data points (blue) show a path from the lower fit to the upper fit, indicating a true increase in ATP:ADP ratio (blue arrow indicates progression over time). Cell "run down" at the end of the experiment can prevent complete recovery to the initial ATP:ADP ratio, causing the blue data points to lie close to but not on the top fitted line.

Supplemental Table S1. Photophysical properties of pHRed and mKeima measured in this study. Extinction coefficients were measured for the mature chromophore. Quantum yields for excitation at 440 nm and emission in the 550-700 nm band were measured against mKeima at pH 7.5, assumed to have a quantum yield of 0.24. Quantum yields for excitation at 585 nm and emission in the 600-700 nm band were measured against Sulforhodamine 101 in ethanol (QY = 0.95)[11] with correction for the difference in refractive indices. N.D. = Not determined.

	pHRed				mKeima			
pH	$\varepsilon_{440\ nm}$	$\varepsilon_{585\ nm}$	$QY_{440\ nm}$	$QY_{585\ nm}$	$\varepsilon_{440\ nm}$	$\varepsilon_{585\ nm}$	$QY_{440\ nm}$	$QY_{585\ nm}$
5.5	18000	15700	0.04	0.41	17700	13600	0.18	0.43
6.0	14200	14500	0.06	0.41	18500	13100	0.19	0.29
6.5	13800	13800	0.06	0.41	18600	7800	0.20	0.31
7.0	16500	14000	0.11	0.45	21200	4500	0.23	0.32
7.5	14800	8700	0.13	0.49	25600	2600	0.24	0.38
8.0	18300	6300	0.13	0.41	24900	1000	0.23	
8.5	22900	4000	0.16	0.48	25700	500	0.25	
9.0	21700	2540	0.18	0.44	22900	800	0.26	
pK_a	7.8	7.8	N.D.	N.D.	6.7	6.7	N.D.	N.D.

	pHRed		mKeima	
pH	$(\varepsilon \cdot QY)_{440}$	$(\varepsilon \cdot QY)_{585}$	$(\varepsilon \cdot QY)_{440}$	$(\varepsilon \cdot QY)_{585}$
5.5	800	6400	3300	5900
6.0	800	6000	3400	3800
6.5	800	5700	3800	2400
7.0	1700	6400	4900	1500
7.5	2000	4300	6100	1000
8.0	2300	2500	5700	
8.5	3600	1900	6400	
9.0	3800	1100	6000	
pK_a	7.8	7.8	6.9	N.D.

Supplemental References.

(1) Kogure, T.; Karasawa, S.; Araki, T.; Saito, K.; Kinjo, M.; Miyawaki, A. *Nat. Biotechnol.* **2006**, *24*, 577-81.
(2) Henderson, J. N.; Osborn, M. F.; Koon, N.; Gepshtein, R.; Huppert, D.; Remington, S. J. *J. Am. Chem. Soc.* **2009**, *131*, 13212-3.
(3) Violot, S.; Carpentier, P.; Blanchoin, L.; Bourgeois, D. *J. Am. Chem. Soc.* **2009**, *131*, 10356-7.
(4) Miesenbock, G.; De Angelis, D. A.; Rothman, J. E. *Nature* **1998**, *394*, 192-5.
(5) Bizzarri, R.; Serresi, M.; Luin, S.; Beltram, F. *Anal. Bioanal. Chem.* **2009**, *393*, 1107-22.
(6) Berg, J.; Hung, Y. P.; Yellen, G. *Nat. Methods* **2009**, *6*, 161-6.
(7) Gross, L. A.; Baird, G. S.; Hoffman, R. C.; Baldridge, K. K.; Tsien, R. Y. *Proc. Natl. Acad. Sci. U.S.A.* **2000**, *97*, 11990-5.
(8) Bulina, M. E.; Chudakov, D. M.; Mudrik, N. N.; Lukyanov, K. A. *BMC Biochem.* **2002**, *3*, 7.
(9) Piatkevich, K. D.; Hulit, J.; Subach, O. M.; Wu, B.; Abdulla, A.; Segall, J. E.; Verkhusha, V. V. *Proc. Natl. Acad. Sci. U.S.A.* **2010**, *107*, 5369-74.
(10) Lin, M. Z.; McKeown, M. R.; Ng, H. L.; Aguilera, T. A.; Shaner, N. C.; Campbell, R. E.; Adams, S. R.; Gross, L. A.; Ma, W.; Alber, T.; Tsien, R. Y. *Chem Biol* **2009**, *16*, 1169-79.
(11) Velapoldi, R. A.; Tonnesen, H. H. *J. Fluoresc.* **2004**, *14*, 465-72.